



REPORT DOCUMENTATION PAGE

1a. REPORT SECURITY CLASSIFICATION Unclassified		1d. RESTRICTIVE MARKINGS None	
2a. SECURITY CLASSIFICATION AUTHORITY None		3. DISTRIBUTION/AVAILABILITY OF REPORT Unlimited	
2b. DECLASSIFICATION/DOWNGRADING SCHEDULE None			
4. PERFORMING ORGANIZATION REPORT NUMBER(S) 88-127-029		5. MONITORING ORGANIZATION REPORT NUMBER(S) <del>XXXXXXXXXX</del> AFOSR-TR. 89-1691	
6a. NAME OF PERFORMING ORGANIZATION University of Wisconsin-Madison	6b. OFFICE SYMBOL (If applicable)	7a. NAME OF MONITORING ORGANIZATION AFOSR/NA	
6c. ADDRESS (City, State and ZIP Code) 750 University Avenue Madison, WI 53706		7b. ADDRESS (City, State and ZIP Code) Building 410 Bolling AFB DC 20332-6448	
8a. NAME OF FUNDING/SPONSORING ORGANIZATION AFOSR	8b. OFFICE SYMBOL (If applicable) NA	9. PROCUREMENT INSTRUMENT IDENTIFICATION NUMBER <del>XXXXXXXXXX</del> AFOSR-87-0233	
8c. ADDRESS (City, State and ZIP Code) AFOSR/NA Bolling AFB DC 20332-6448		10. SOURCE OF FUNDING NOS.	
		PROGRAM ELEMENT NO. 61107	PROJECT NO. 2302
11. TITLE (Include Security Classification) Analysis of Biaxial Stress Fields..(U)			
12. PERSONAL AUTHOR(S) Balish, Stanley S., Enke, Neal F., Lesniak, Jon R., Sandor, Bela I.			
13a. TYPE OF REPORT Final	13b. TIME COVERED FROM 87/7/1 TO 89/8/31	14. DATE OF REPORT (Yr., Mo., Day) 1989-10-19	15. PAGE COUNT 146
16. SUPPLEMENTARY NOTATION			
17. COSATI CODES		18. SUBJECT TERMS (Continue on reverse if necessary and identify by block number) Thermographic stress analysis; SPATE; High-temperature stress analysis; Thermoelasticity	
FIELD	GROUP SUB. GR.		
19. ABSTRACT (Continue on reverse if necessary and identify by block number) Enhanced theories for thermographic stress analysis of isotropic and anisotropic materials are developed. These stress analysis techniques involve the measurement of the dynamic changes in temperature of a component undergoing dynamic loading. The enhanced theories presented allow for quantitative analyses of nonlinear thermoelastic and thermoplastic effects. A theory quantifying damage in anisotropic materials is also presented. From these analytical developments, several new applications for thermographic stress analysis are developed including residual stress analysis, cyclic plasticity analysis, and high-temperature stress analysis. A numerical method for separating the principal stresses is also developed. Examples of each of these applications are presented, and limitations for each are given. In particular, the principal problems encountered with regards to (cont'd. on reverse)			
20. DISTRIBUTION/AVAILABILITY OF ABSTRACT UNCLASSIFIED/UNLIMITED <input checked="" type="checkbox"/> SAME AS RPT. <input type="checkbox"/> DTIC USERS <input checked="" type="checkbox"/>		21. ABSTRACT SECURITY CLASSIFICATION Unclassified/unlimited	
22a. NAME OF RESPONSIBLE INDIVIDUAL LT, COL George K LARSEN	22b. TELEPHONE NUMBER (Include Area Code) (304) 762-0463	22c. OFFICE SYMBOL NA	

89 12 20 020

19. high-temperature stress analysis are discussed at length.

Residual stress analyses were performed on a C-shaped specimen of Ti-6Al-4V alloy, and the minimum resolvable residual stress was found to be 25 PMA. Cyclic plasticity analyses of 1020 steel and 6061-T6 aluminum were performed. The data obtained were found to be in qualitative agreement with the enhanced theory. Quantitative verification was not possible because of limitations in the commercial thermographic equipment used. Based on the enhanced theory, it is predicted that the minimum resolvable stress amplitude using thermographic stress analysis will be approximately independent of temperature, provided relevant thermal and mechanical material properties do not change dramatically. This prediction is verified for 304 stainless steel for temperatures from twenty-five to eight hundred fifty degrees Celsius.

# Analysis of Biaxial Stress Fields in Plates Cracking at Elevated Temperature

Final Technical Report

AFOSR-87-0253

Project Period: July 1, 1987 - August 31, 1989

October 19, 1989

by

Stanley S. Balish

Neal F. Enke

Jon R. Lesniak

Bela I. Sandor

Accession For	
NTIS GRA&I	<input checked="" type="checkbox"/>
DTIC TAB	<input type="checkbox"/>
Unannounced	<input type="checkbox"/>
Justification	
By _____	
Distribution/	
Availability Codes	
_____ / or	
Dist	Special
A-1	

University of Wisconsin-Madison

## ABSTRACT

Enhanced theories for thermographic stress analysis of isotropic and anisotropic materials are developed. These stress analysis techniques involve the measurement of the dynamic changes in temperature of a component undergoing dynamic loading. The enhanced theories presented allow for quantitative analyses of nonlinear thermoelastic and thermoplastic effects. A theory quantifying damage in anisotropic materials is also presented. From these analytical developments, several new applications for thermographic stress analysis are developed including residual stress analysis, cyclic plasticity analysis, and high-temperature stress analysis. A numerical method for separating the principal stresses is also developed. Examples of each of these applications are presented, and limitations for each are given. In particular, the principal problems encountered with regards to high-temperature stress analysis are discussed at length.

Residual stress analyses were performed on a C-shaped specimen of Ti-6Al-4V alloy, and the minimum resolvable residual stress was found to be 25 MPa. Cyclic plasticity analyses of 1020 steel and 6061-T6 aluminum were performed. The data obtained were found to be in qualitative agreement with the enhanced theory. Quantitative verification was not possible because of limitations in the commercial thermographic equipment used. Based on the enhanced theory, it is predicted that the minimum resolvable stress amplitude using thermographic stress analysis will be approximately independent of temperature, provided relevant thermal and mechanical material properties do not change dramatically. This prediction is verified for 304 stainless steel for temperatures from twenty-five to eight hundred fifty degrees Celsius.

## TABLE OF CONTENTS

		<b>Page</b>
	ABSTRACT	i
	LIST OF TABLES	iv
	LIST OF FIGURES	v
	NOMENCLATURE	viii
 <b>Chapter</b>		
1	INTRODUCTION	1
2	FUNDAMENTALS OF THERMOGRAPHIC STRESS ANALYSIS	4
	2.1 Historical Overview	4
	2.2 Nonlinear Thermoelastic Effects	4
	2.3 Thermoplastic Effects	5
	2.4 The Classical TSA Equation	6
3	THE THERMO-ELASTIC-PLASTIC EQUATION	8
	3.1 Assumptions and Initial Developments	8
	3.2 Thermoplastic Effects	9
	3.3 Nonlinear Thermoelastic Effects	10
	3.4 The Isotropic Thermo-elastic-plastic Equation	11
4	MEAN STRESS EFFECTS	12
	4.1 Stress-based Nonlinear Thermoelastic Equation	12
	4.2 In-phase, Proportional, Biaxial Loading	15
	4.3 In-phase, Proportional, Uniaxial Loading	23
	4.4 Residual Stress Analysis	25
5	THE ENHANCED TSA EQUATION	31
6	CYCLIC PLASTICITY ANALYSIS	38
	6.1 Analytical Development	38
	6.2 Experimental Setup	42
	6.3 Experimental Results	43
	6.4 Chapter Summary	48

## TABLE OF CONTENTS (Continued)

	Page	
7	HIGH-TEMPERATURE STRESS ANALYSIS	50
	7.1 Chromatic Aberration	50
	7.2 Photodetector Saturation	52
	7.3 Temperature Gradient Effects	52
	7.5 Emissivity Effects	53
	7.6 Edge Effects	54
	7.7 Experimental Results	55
	7.8 New Specimen Geometry	57
8	A Thermoelasticity Theory For Damage in Anisotropic Materials ( Dr. Daqing Zhang )	59
9	Separation of Thermoelastically Induced Isopachics Into Individual Stresses ( Professor R.E. Rowlands and Dr. Y.M. Huang )	62
10	SUMMARY AND CONCLUSIONS	64
	APPENDIX A	66
	A.1 Infrared Radiation	66
	APPENDIX B	69
	B.1 Infrared Photon Detectors	69
	TABLES	75
	FIGURES	77
	REFERENCES	133

## LIST OF TABLES

Table		Page
1	Mechanical and Thermal Properties of Selected Materials at Room Temperature	75
2	Effect of Prior Plastic Strain on the Thermoelastic Constant of Ti-6Al-4V	76

## LIST OF FIGURES

Figure		Page
1	Spectral radiant photon emittance of a blackbody versus temperature and wavelength	77
2	Infrared transmission of the atmosphere. Adapted from Ref. 26.	78
3	Responsivity of an ideal photodetector	79
4	Location of TSA line scans for the 7075-T651 aluminum plate with a centrally located hole. All dimensions in mm.	80
5	Raw TSA data for two different mean loads for the 7075-T651 aluminum specimen	81
6	Amplitude of the first stress invariant determined from the TSA line scans of the 7075-T651 aluminum specimen	82
7	$\psi$ versus distance from left edge of specimen for the 7075-T651 aluminum specimen	83
8	Mean stress effect in 7075-T651 aluminum	84
9	Mean stress effect in 4150 heat-treated steel	85
10	Mean stress effect in Ti-6Al-4V	86
11	Nonlinear thermoelastic effect at twice the specimen cycling frequency for 6061-T6 aluminum	87
12	Geometry of the Ti-6Al-4V C-specimen	88
13	TSA line scans for the Ti-6Al-4V C-specimen after various overloads	89
14	Estimated residual stress versus prior plastic strain for the Ti-6Al-4V C-specimen	90
15	Estimated residual stress versus number of overloads for the Ti-6Al-4V C-specimen	91
16	$S^2(\omega)$ versus stress amplitude for 1020 steel at room temperature	92
17	TSA calibration factor versus frequency for 304 stainless steel at room temperature	94
18	Absolute calibration of the SPATE system from -11 °C to 55 °C	95

## LIST OF FIGURES (Continued)

Figure		Page
19	Shape of a "generic" hysteresis loop	97
20	Effect of a single cycle of sinusoidal stress on the TSA output for elastic-plastic loading conditions	98
21	FFT of load and TSA outputs for a 1020 steel specimen undergoing cyclic plasticity	99
22	Plastic-work energy per cycle versus plastic strain amplitude for 1020 steel	100
23	Plastic-work energy per cycle versus plastic strain amplitude for 6061-T6 aluminum at 25 °C	102
24	Cyclic stress-strain curves for 1020 steel	103
25	Cyclic stress-strain curve for 6061-T6 aluminum	105
26	Plastic-work energy per cycle versus $S^a(2\omega)$ for 1020 steel	106
27	$S^a(2\omega)$ versus $S^a(4\omega)$ for 1020 steel	107
28	$S^a(2\omega)$ versus stress amplitude and plastic-work energy per cycle for 6061-T6 aluminum	108
29	$S^a(\omega)$ versus stress amplitude for 1020 steel at 8 °C	110
30	Effect of a rapid change in incident photon flux on the TSA output of the SPATE system	111
31	$S^a(\omega)$ versus stress amplitude for 1020 steel at 25 °C	112
32	$S^a(\omega)$ versus stress amplitude for 6061-T6 aluminum at 25 °C	113
33	Specimen design used to determine proper focus settings for the SPATE infrared camera	114
34	Examples of in-focus and out-of-focus scans	115
35	Focus curves of the SPATE infrared camera for 8 to 12 $\mu\text{m}$ and 2 to 3 $\mu\text{m}$	116
36	Example of the effects of atmospheric turbulence on the TSA output	117

## LIST OF FIGURES (Continued)

Figure		Page
37	Geometry of the Hastelloy-X specimen. All dimensions in mm.	118
38	Effects of excessive incident photon flux on the TSA output	119
39	Effects of nonuniform spatial emissivity on the TSA output	120
40	Minimum resolvable stress versus temperature	121
41	FFT of TSA output for Hastelloy-X specimen at 1040 °C	122
42	TSA line scans of Hastelloy-X specimen at four different load amplitudes	123
43	Comparison of TSA line scans of Hastelloy-X specimen at 25 °C and 1040 °C	124
44	TSA frame scans of 304 stainless steel with 1/4" diameter hole in center at temperatures of 23°C, 100°C, 300°C and 800°C	125
45	Comparison of effective modulus $E^e$ of [0/0/90 <sub>5</sub> ] <sub>s</sub> laminate measured by two methods Damaging stresses: $\Delta\sigma = 58$ MPa, $R = 0.1$ Nondestructive stresses for TSA: $\Delta\sigma = 8$ MPa, $R = 0.1$	126
46	Normalized effective mass density $\rho^e/\rho$ during damage evolution of [0/90/0/90/0] <sub>s</sub> laminate measured by the TSA method Damaging stresses: $\Delta\sigma = 317$ MPa, $R = 0.1$ Nondestructive stresses for TSA: $\Delta\sigma = 31$ MPa, $R = 0.1$	127
47	Damage accumulation of [0/0/90 <sub>5</sub> ] <sub>s</sub> laminate measured by the TSA method Damaging stresses: $\Delta\sigma = 58$ MPa, $R = 0.1$ Nondestructive stresses for TSA: $\Delta\sigma = 8$ MPa, $R = 0.1$	128
48	Tensile Aluminum Plate Whose Individual Stresses Were Determined Thermoelastically	129
49	Thermoelastic Information in Region R Adjacent to the Top of the Hole of Fig. 48	130
50	Thermoelastically Determined Tensile Stress $\sigma_x / \sigma_0$ in Region R Adjacent to the Top of the Hole of Fig. 48	131
51	Theoretically Predicted $\sigma_x / \sigma_0$ in the Region R Adjacent to the Top of Hole of Fig. 48	132

## NOMENCLATURE

- $C_e$  = specific heat at constant strain
- $C_p$  = specific heat at constant pressure
- $c$  = speed of light
- $D^*$  = photodetector detectivity
- $E$  = Young's modulus
- $e$  = surface emissivity
- $G$  = shearing modulus (modulus of rigidity)
- $h$  = Planck's constant
- $I_1, J_1$  = first invariant of stress and strain, respectively
- $I_2, J_2$  = second invariant of stress and strain, respectively
- $k$  = Boltzmann's constant
- $K'$  = thermal conductivity
- $Q$  = heat
- $R$  = photodetector responsivity
- $S$  = photodetector output voltage (TSA output)
- $t$  = time
- $T$  = instantaneous temperature
- $T_0$  = initial (nominal) specimen temperature
- $W_\lambda$  = spectral radiant emittance
- $W_p$  = plastic-work energy per cycle
- $\alpha$  = coefficient of thermal expansion

## NOMENCLATURE (Continued)

- $\varepsilon$  = total strain  
 $\varepsilon_p$  = plastic strain  
 $\phi_\lambda$  = spectral radiant photon emittance  
 $\lambda$  = wavelength of light  
 $\lambda'$  = Lamé constant  
 $\nu$  = Poisson's ratio  
 $\rho$  = density  
 $\sigma$  = stress  
 $c_\varepsilon$  = specific heat capacity for  $\varepsilon_i = 0$   
 $\rho^e$  = effective material density

## 1. INTRODUCTION

In this report, a broad analytical and experimental investigation into the field of thermographic stress analysis (TSA) is presented. To date, this new experimental technique (also known as the SPATE method or thermoelastic stress analysis) has been used almost exclusively for room-temperature linear-elastic stress analysis under constant-frequency sinusoidal loading. The purpose of this report is to provide a more complete theoretical and experimental basis for thermographic stress analysis with emphasis on the measurements of those phenomena related to high temperature crack studies. In particular, the following new applications for TSA are developed:

1. Simultaneous measurement of elastic-work energy and plastic-work energy under sinusoidal loading conditions.
2. High-temperature stress analysis
3. Residual and mean stresses

A basic description of infrared thermography, along with a brief review of literature relevant to this report, is presented in Chapter 2. In Chapter 3, a thermo-elastic-plastic equation is developed from first principles. This equation forms the basis for understanding mean stress, plasticity, and heat conduction effects. Mean stress effects (i.e., the effects of mean stresses on the thermoelastic output) are discussed in Chapter 4. Techniques for determining principal stresses and residual stresses via mean stress effects are also discussed. An enhanced TSA equation is presented in Chapter 5. This enhanced equation accounts for nonlinear thermoelastic,

thermoplastic, and specimen motion effects. The effects of cyclic plasticity on the TSA output are described in Chapter 6. The final major topic of this report is the application of thermographic stress analysis at high temperatures. Several important yet subtle phenomena had to be isolated and understood in order to obtain meaningful high-temperature TSA data. The details are given in Chapter 7.

The nonlinear thermoelastic and thermoplastic theories developed in this report are restricted to homogeneous, isotropic materials. As such, several important material phenomena such as viscoelastic, viscoplastic, and anisotropic material response are not addressed. The discussions on specimen motion effects and high-temperature phenomena apply, in general, to all solid materials.

### GENERAL EXPERIMENTAL PROCEDURE

All experiments were performed using closed-loop, servo-hydraulic testing equipment. Load was monitored using conventional load cells. Strain was measured in the cyclic plasticity tests using clip-gage extensometers having gage lengths of either 10 mm or 12.5 mm. These extensometers have a strain resolution under best conditions of approximately 20 microstrain. All TSA data were acquired using a SPATE 8000 system. This equipment employs a mercury-doped cadmium-telluride (Hg:CdTe) photodiode which is quoted by the manufacturer as having a dynamic temperature resolution of 0.001 K under best conditions. The equipment uses a lock-in amplifier to analyze the photodiode output voltage (also referred to in this report as the TSA output). This lock-in amplifier was used to obtain the full-field TSA data presented herein. For much of the work in this report, however, the lock-in amplifier was bypassed, and the TSA output was fed into a Nicolet 660A FFT spectrum

analyzer. This allowed for measurement of the TSA output at multiple frequencies, rather than the single-frequency measurement obtained with the lock-in amplifier. This was necessary in order to analyze cyclic plasticity effects. It was also quite useful for analyzing background noise levels coming from the infrared camera. A drawback of the FFT analyzer was that data were only obtained at a single point on the specimen. Also, the analyzer required significant time to "settle in" once specimen cycling had begun. This was a problem when analyzing elastic-plastic response since the specimen would heat up significantly before data capture had begun. This is further discussed in Chapter 6. Other details on the testing procedures and equipment are presented as needed.

## 2. FUNDAMENTALS OF THERMOGRAPHIC STRESS ANALYSIS

### 2.1 Historical Overview

The thermoelastic effect was discovered by Weber in 1830 [1], and a theoretical explanation was subsequently developed by Lord Kelvin in 1853 [2]. Between that time and the late 1960's experimental investigations into the thermoelastic effect were most often conducted using thermocouples, as no better instrumentation was available (see, for example, Refs. 3-6). This limited the temperature resolution to about 0.1 K, and data could only be obtained at a single point per thermocouple. In 1967, Belgen [7] demonstrated the feasibility of using photoconductive photodetectors to measure cyclic variations in stress. The use of photodetectors has the advantages of remote, scannable sensing and excellent dynamic temperature resolution. Belgen's work laid the foundation for development of commercial equipment in the late 1970's [8].

With regards to the primary topics of this report (nonlinear thermoelastic, thermoplastic, and high-temperature thermographic stress analysis), several prior publications are of significant interest. These are summarized below.

### 2.2 Nonlinear thermoelastic effects

Rocca and Bever [4] performed analytical work on nonlinear thermoelastic effects as early as 1950. They assumed that the thermal expansion coefficient and specific heat vary with stress. Their theory was limited to uniaxial loading, and no experimental verification was possible owing to the limited temperature resolution of the equipment available at the time. Dillon [9] took a very general approach in which the free energy

was expanded in terms of a power series of the strain invariants and temperature. His resulting nonlinear thermoelastic equation is similar, but not identical, to that developed herein. Wong et al. [10] also followed a free energy approach in which they assumed that elastic and thermal properties were temperature dependent. Their resulting equation can be shown to be identical to that developed herein. Machin, Sparrow, Wong, Stimson, Dunn and Lombardo [11-14] also performed substantial verification of this theory for uniaxial loading, and they demonstrated the feasibility of measuring residual stresses via thermoelastic techniques [15].

### 2.3 Thermoplastic effects

Dillon [16] developed a theory for thermoplasticity and used thermocouples to monitor the effects of plasticity on specimen temperature. Using thermocouples, Jordan and Sandor [17-19] obtained quantitative measurements of the effects of elastic and plastic strains on the thermal output. Stanley and Chan [20] qualitatively analyzed the effects of cyclic plasticity on the TSA output. They noticed a rapid increase in the TSA amplitude for stress amplitudes beyond the elastic limit. They speculated that this nonlinearity was due to increases in specimen temperature, but no quantitative verification was performed. Beghi et al. [21] used thermistors to monitor temperature changes in a compact tension specimen undergoing sinusoidal loading. The thermistor outputs were then fed into an FFT analyzer. They noted the presence of higher harmonic terms in the thermistor outputs near the crack tip and speculated that this was due either to localized plasticity or crack closure phenomena. Beghi et al. [22] also developed a theory for irreversible thermodynamics of metals under stress. Their final equation is similar to those of Jordan [18] and Dillon [16].

To the best of our knowledge, no other significant papers in the areas of nonlinear

thermoelastic, thermoplastic, or high-temperature thermographic stress analysis have been published, except for two introductory papers by Enke et al. [23-24]. The developments in this report supersede most of the results of those two papers, given in Chapter 7.

#### 2.4 The Classical TSA Equation

The classical thermoelastic equation relates temperature change to the sum of the principal stresses

$$\frac{dT}{dt} = \frac{-\alpha T}{\rho C_p} \frac{dI_1}{dt} \quad (2.1)$$

The SPATE camera, however, is sensitive to the incident photon flux. If it is assumed that only temperature and not emissivity varies with time, the photon flux is related to the absolute temperature by

$$\phi = eBT^3 \quad (2.2)$$

Eq. 2.2 can be differentiated to give

$$\frac{d\phi}{dt} = 3eBT^2 \frac{dT}{dt} \quad (2.3)$$

Substituting the classical thermoelastic equation (Eq. 2.1) into Eq. 2.3 results in

$$\frac{d\phi}{dt} = \frac{-3eB\alpha T^3}{\rho C_p} \frac{dI_1}{dt} \quad (2.4)$$

Under normal operating conditions, the photodetector output voltage is linearly related to the total incident photon rate,  $\phi_i$ :

$$S = R \phi_i = e R B T^3 + R \phi_b \quad (2.5)$$

where  $\phi_b$  is the incident photon rate for background radiation. Background radiation is any radiation that reaches the detector but originates from somewhere other than the target. For photodiodes the detector responsivity,  $R$ , is independent of the intensity of the incident radiation, except at very high incident power levels.

By differentiating Eq. 2.5 and substituting into Eq. 2.4, the classical TSA equation is obtained:

$$\frac{dS}{dt} = \frac{-3eRB\alpha T^3}{\rho C_p} \frac{dI_1}{dt} \quad (2.6)$$

where variations in background flux have been ignored. This equation applies to both photovoltaic and photoconductive detectors. Provided the temperature, emissivity, specimen material properties, and detector responsivity remain constant, the change in photodetector output voltage is proportional to the change in the first stress invariant. In the remainder of this report, enhancements to the classical TSA equation (Eq. 2.6) will be made.

### 3. THE THERMO-ELASTIC-PLASTIC EQUATION

#### 3.1 Assumptions and Initial Developments

In developing the thermo-elastic-plastic equation, a number of assumptions are made:

- A1: No significant heat transfer takes place across the boundary of the thermodynamic system (i.e., the system is adiabatically isolated).
- A2: The material composing the thermodynamic system is solid, homogeneous and isotropic.
- A3: Heat generation can be divided into reversible and irreversible components. The reversible component is assumed to be due entirely to thermoelastic effects and the irreversible component to thermoplastic effects. Thus, this report does not address such topics as viscoelasticity and viscoplasticity.
- A4: Moderate amounts of plasticity do not alter significantly the material parameters  $\alpha$ ,  $\rho$ ,  $C_e$ ,  $E$ , and  $\nu$ .
- A5: The conversion of plastic-work energy into heat occurs instantaneously.
- A6: Before application of mechanical loading, the system is at a uniform temperature.

Most of the assumptions necessary for the theory of static thermoelasticity also apply (e.g., displacements and their derivatives are small, negligible body forces, etc.).

Other assumptions and restrictions are introduced as needed.

The thermodynamic system is taken to be the material body (or some portion thereof) that is being mechanically loaded. Since the body is assumed to be solid, the only mode of heat transfer within the system is conduction. Employing assumptions

A1 through A3 along with the isotropic form of Fourier's law of heat conduction results in

$$\frac{dT}{dt} = \frac{1}{\rho C_e} \left( K' \nabla^2 T + \frac{dQ_{rev}}{dt} + \frac{dQ_{irrev}}{dt} \right) \quad (3.1)$$

### 3.2 Thermoplastic Effects

No constitutive equation for elastic-plastic response is assumed; instead, the hypothesis is made that the rate of irreversible heat generation is directly proportional to the rate of generation of plastic-work energy,

$$\frac{dQ_{irrev}}{dt} = \rho C_e \frac{dT_{irrev}}{dt} = \beta \frac{dW_p}{dt} \quad (3.2)$$

where

$$W_p = \int \sigma_{ij} d(\epsilon_p)_{ij}$$

and  $\beta$  is the fraction of plastic-work energy that is converted into heat. Note that  $\beta = 1$  implies that there is no stored-energy of cold work, whereas  $\beta = 0$  implies that all the plastic-work energy is converted into stored-energy of cold work. For most metals, almost all the plastic-work energy is converted to heat [30]. This will be especially true under cyclically stabilized loading conditions. Thus, assuming  $\beta = 1$  will not usually result in significant error for cyclic elastic-plastic TSA analysis.

### 3.3 Nonlinear Thermoelastic Effects

Using Biot's procedure [31], the following equation can be derived:

$$dQ_{\text{rev}} = T \frac{\partial \sigma_{ij}}{\partial T} d\varepsilon_{ij} \quad (3.3)$$

This equation is valid for anisotropic, reversible, adiabatic response. The analysis herein will be restricted to isotropic material behavior. In developing the nonlinear isotropic thermoelastic equation, the Duhamel-Neumann equation of thermoelasticity is employed:

$$\sigma_{ij} = \lambda' J_1 \delta_{ij} + 2G \varepsilon_{ij} - \frac{\alpha E}{1-2\nu} (T - T_0) \delta_{ij} \quad (3.4)$$

where  $\varepsilon_{ij}$  is understood to be a purely elastic strain. Differentiating Eq. 3.4 with respect to temperature gives

$$\frac{\partial \sigma_{ij}}{\partial T} = \frac{\partial \lambda'}{\partial T} J_1 \delta_{ij} + 2 \frac{\partial G}{\partial T} \varepsilon_{ij} - \frac{\alpha E}{1-2\nu} \delta_{ij} - \frac{T - T_0}{1-2\nu} \vartheta \delta_{ij} \quad (3.5)$$

where

$$\vartheta = E \frac{\partial \alpha}{\partial T} + \alpha \frac{\partial E}{\partial T} + \frac{2\alpha E}{1-2\nu} \frac{\partial \nu}{\partial T}$$

The last term on the right side of Eq. 3.5 is generally much smaller than the others and can be neglected. Substituting Eq. 3.5 into Eq. 3.3 results in

$$\frac{dQ_{\text{rev}}}{dt} = T \left[ \left( \frac{-\alpha E}{1-2\nu} \right) \frac{dJ_1}{dt} + \frac{\partial \lambda'}{\partial T} J_1 \frac{dJ_1}{dt} + 2 \frac{\partial G}{\partial T} \varepsilon_{ij} \frac{d\varepsilon_{ij}}{dt} \right] \quad (3.6)$$

This can be shown to be identical to the result obtained by Wong et al. [10]. The right side of Eq. 3.6 is a tensor expression quadratic in strain. Since  $dQ_{\text{rev}}/dt$  is a scalar quantity, this tensor expression must be expressible in terms of the first and second strain invariants,  $J_1$  and  $J_2$ . It is easily verified that Eq. 3.6 is equivalent to

$$\frac{dQ_{\text{rev}}}{dt} = T \left[ \left( \frac{-\alpha E}{1-2\nu} \right) \frac{dJ_1}{dt} + \left( \frac{\partial \lambda'}{\partial T} + 2 \frac{\partial G}{\partial T} \right) J_1 \frac{dJ_1}{dt} - 2 \frac{\partial G}{\partial T} \frac{dJ_2}{dt} \right] \quad (3.7)$$

#### 3.4 The Isotropic Thermo-elastic-plastic Equation

Combining Eqs. 3.7, 3.2 and 3.1 gives the general thermo-elastic-plastic equation for homogeneous, isotropic materials:

$$\begin{aligned} \rho C_e \frac{dT}{dt} = T \left[ \left( \frac{-\alpha E}{1-2\nu} \right) \frac{dJ_1}{dt} + \left( \frac{\partial \lambda'}{\partial T} + 2 \frac{\partial G}{\partial T} \right) J_1 \frac{dJ_1}{dt} - 2 \frac{\partial G}{\partial T} \frac{dJ_2}{dt} \right] \\ + K' \nabla^2 T + \beta \frac{dW_p}{dt} \end{aligned} \quad (3.8)$$

In the chapters that follow, simplified forms of this equation will be developed and experimentally verified. Note that by neglecting plasticity, heat conduction, and changes in  $\lambda'$  and  $G$  with temperature, the classical thermoelastic equation is obtained.

## 4. MEAN STRESS EFFECTS

### 4.1 Stress-based Nonlinear Thermoelastic Equation

In order to investigate the effects of mean stresses on the thermoelastic output, it is desirable to convert Eq. 3.8 to an alternative form. For simplicity, heat conduction and plasticity effects will be ignored. This results in the following:

$$dT = \frac{T}{\rho C_e} \left[ \left( \frac{-\alpha E}{1-2\nu} \right) dJ_1 + \left( \frac{\partial \lambda'}{\partial T} + 2 \frac{\partial G}{\partial T} \right) J_1 dJ_1 - 2 \frac{\partial G}{\partial T} dJ_2 \right] \quad (4.1)$$

Next, Eq. 4.1 must be converted from a strain-based to a stress-based formulation.

The Duhamel-Neumann equation can be written as

$$\epsilon_{ij} = \frac{1+\nu}{E} \sigma_{ij} - \frac{\nu}{E} I_1 \delta_{ij} + \alpha (T - T_0) \delta_{ij} \quad (4.2)$$

where  $\epsilon_{ij}$  is a purely elastic strain. The first strain invariant and its derivative can be written as

$$J_1 = \epsilon_{kk} = \frac{1-2\nu}{E} I_1 + 3\alpha (T - T_0) \quad (4.3a)$$

and

$$dJ_1 = \frac{1-2\nu}{E} dI_1 + 3\alpha dT \quad (4.3b)$$

Similarly,

$$d\epsilon_{ij} = \frac{1+\nu}{E} d\sigma_{ij} - \frac{\nu}{E} dI_1 + \alpha dT \quad (\text{for } i=j) \quad (4.4a)$$

$$d\epsilon_{ij} = \frac{1+\nu}{E} d\sigma_{ij} \quad (\text{for } i \neq j) \quad (4.4b)$$

The derivative of the second strain invariant can be written as

$$\begin{aligned} dJ_2 = & \epsilon_{11}(d\epsilon_{22} + d\epsilon_{33}) + \epsilon_{22}(d\epsilon_{11} + d\epsilon_{33}) + \epsilon_{33}(d\epsilon_{11} + d\epsilon_{22}) \\ & - 2\epsilon_{12}d\epsilon_{12} - 2\epsilon_{13}d\epsilon_{13} - 2\epsilon_{23}d\epsilon_{23} \end{aligned} \quad (4.5)$$

Substituting Eq. 4.4 into 4.5 and simplifying gives

$$\begin{aligned} dJ_2 = & \frac{2\nu(\nu-2)}{E^2} I_1 dI_1 + \left(\frac{1+\nu}{E}\right)^2 dI_2 + \frac{2(1-2\nu)}{E} \alpha (T-T_0) dI_1 \\ & + \frac{2(1-2\nu)}{E} \alpha I_1 dT + 6\alpha^2 (T-T_0) dT \end{aligned} \quad (4.6)$$

Substituting Eqs. 4.6 and 4.3 into 4.1 and simplifying results in

$$\left( \frac{\rho C_e}{T} + \frac{3E\alpha^2}{1-2\nu} - \Sigma_4 I_1 \right) dT = \left[ \left( -\alpha - \Sigma_1 + \Sigma_5 \right) dI_1 + \Sigma_2 I_1 dI_1 - \Sigma_3 dI_2 \right] \quad (4.7)$$

where

$$\Sigma_1 = 4 \frac{\partial G}{\partial T} \frac{1-2\nu}{E} \alpha (T-T_0)$$

$$\Sigma_2 = \frac{1}{E^2} \frac{\partial E}{\partial T}$$

$$\Sigma_3 = \frac{1}{2G^2} \frac{\partial G}{\partial T}$$

$$\Sigma_4 = \left( \frac{\partial \lambda'}{\partial T} + 2 \frac{\partial G}{\partial T} \right) \left( \frac{1-2\nu}{E} \right) (3\alpha) - 4\alpha \frac{\partial G}{\partial T} \frac{1-2\nu}{E}$$

$$\Sigma_5 = \Sigma_4 (T-T_0)$$

For most solid isotropic materials,

$$|-\Sigma_1 + \Sigma_5| \ll |\alpha| \quad \text{and} \quad |\Sigma_4 I_1| \ll \frac{\rho C_e}{T}$$

for realistic values of  $I_1$  and  $T$ . These terms are therefore neglected. The relationship between specific heat at constant volume,  $C_e$ , and specific heat at constant pressure is given by [32]:

$$\rho C_e + \frac{3E\alpha^2 T}{1-2\nu} = \rho C_p$$

Combining these results, Eq. 4.7 reduces to

$$dT = \frac{T}{\rho C_p} \left[ -\alpha dI_1 + \frac{1}{E^2} \frac{\partial E}{\partial T} I_1 dI_1 - \frac{1}{2G^2} \frac{\partial G}{\partial T} dI_2 \right] \quad (4.8)$$

Provided the temperature change,  $\Delta T = T - T_0$ , is small compared to  $T_0$ , this can be integrated to give

$$T(t) = \frac{T_0}{\rho C_p} \left[ -\alpha I_1 + \frac{1}{2E^2} \frac{\partial E}{\partial T} I_1^2 - \frac{1}{2G^2} \frac{\partial G}{\partial T} I_2 \right] + T_0 \quad (4.9)$$

This is the stress-based formulation of the nonlinear thermoelastic equation. Note that the right-hand side of Eq. 4.9 is invariant with respect to coordinate rotation, as it must be since the left-hand side is a scalar quantity.

## 4.2 In-phase, Proportional, Biaxial Loading

### Analytical Development

In order to investigate mean stress effects, the analysis will be confined to situations in which the applied loading is in-phase and proportional. For simplicity, the loading will be further assumed to be sinusoidal with a constant mean load. Such loading is not unrealistic; in fact, it is the most common loading mode used in thermographic stress analysis at this time. Under such conditions, the stresses can be written as

$$\sigma_{ij}(t) = \sigma_{ij}^m + \sigma_{ij}^a \sin(\omega t) \quad (4.10)$$

where the superscripts "m" and "a" refer to mean stress and stress amplitude,

respectively. It follows that

$$I_1(t) = I_1^m + I_1^a \sin(\omega t) \quad (4.11a)$$

and

$$[I_1(t)]^2 = 2I_1^m I_1^a \sin(\omega t) - \frac{1}{2} (I_1^a)^2 \cos(2\omega t) + C_1 \quad (4.11b)$$

where  $C_1$  is a constant with respect to time. Since thermographic stress analysis is based on the measurement of dynamic effects, this constant can be ignored.

A few comments on the notation of Eq. 4.10 are in order. First of all, for normal stresses, the mean stress can be positive or negative, depending on whether the mean stress is tensile or compressive, respectively. For shear stresses, the sign of the mean stress depends on the choice of coordinate axes. The stress amplitudes can also be positive or negative. One stress amplitude is arbitrarily given a sign, and the signs of the other stress amplitude terms follow. For example, let the stress amplitude in the 1-direction be positive. If  $\sigma_{11}$  increases as load is applied to the component, but  $\sigma_{22}$  decreases, it follows that the stress amplitude in the 2-direction is negative. In other words, the stress amplitude in the 2-direction is 180 degrees out-of-phase with the stress amplitude in the 1-direction.

Although a general triaxial formulation of the nonlinear thermoelastic equation can be developed, it is not very useful, since thermographic stress analysis is used typically for analyzing biaxial surface stress distributions. The remaining analysis is therefore limited to biaxial stress conditions ( $\sigma_{13} = \sigma_{23} = \sigma_{33} = 0$ ). The second stress invariant is given by

$$I_2 = \sigma_{11} \sigma_{22} - \sigma_{12}^2 \quad (4.12a)$$

Using Eq. 4.10, this can be rewritten as

$$I_2 = \left( \sigma_{11}^m \sigma_{22}^a + \sigma_{22}^m \sigma_{11}^a - 2 \sigma_{12}^m \sigma_{12}^a \right) \sin(\omega t) - \frac{1}{2} I_2^a \cos(2\omega t) \quad (4.12b)$$

where

$$I_2^a = \sigma_{11}^a \sigma_{22}^a - (\sigma_{12}^a)^2$$

Substituting Eqs. 4.11 and 4.12 into 4.9 gives

$$T(t) = T^a(\omega) \sin(\omega t) + T^a(2\omega) \cos(2\omega t) + T_0 \quad (4.13a)$$

where

$$T^a(\omega) = \frac{T_0}{\rho C_p} \left[ -\alpha I_1^a + \frac{1}{E^2} \frac{\partial E}{\partial T} I_1^m I_1^a \right] - \frac{T_0}{\rho C_p} \left[ \frac{1}{2G^2} \frac{\partial G}{\partial T} \left( \sigma_{11}^m \sigma_{22}^a + \sigma_{22}^m \sigma_{11}^a - 2 \sigma_{12}^m \sigma_{12}^a \right) \right] \quad (4.13b)$$

and

$$T^a(2\omega) = \frac{-T_0}{4\rho C_p} \left[ \frac{1}{E^2} \frac{\partial E}{\partial T} (I_1^a)^2 - \frac{1}{G^2} \frac{\partial G}{\partial T} I_2^a \right] \quad (4.13c)$$

The temperature response is seen to consist of two oscillating components. One component occurs at the cycling frequency,  $\omega$ , and consists of mean stress and stress amplitude terms. The other component occurs at the second harmonic,  $2\omega$ , and consists entirely of stress amplitude terms. This was first shown by Wong et al. [10] for the case of uniaxial loading. This second harmonic term is important when considering temperature changes due to cyclic plasticity effects, which show up strongly at the second harmonic (see Chapter 6). This second harmonic term is irrelevant from the standpoint of mean stress effects.

For most materials, mean stress effects are small compared to stress amplitude effects, and experimental verification of Eq. 4.13b by absolute measurement of temperature amplitudes is extremely difficult. In order to circumvent this problem, a comparison technique is used. This is done as follows. A component of complex geometry is subjected to a static tensile mean load and a sinusoidal cyclic load of known amplitude, and a TSA scan is performed. The component is then subjected to a compressive mean load having the same magnitude as the tensile mean load. A sinusoidal cyclic load having the same amplitude as in the tensile mean load test is applied, and another TSA scan is performed. To analyze the data from these two TSA scans, it is assumed that the structure behaves in a linear elastic fashion and that the specimen geometry does not change significantly with application of the loads. Thus, if  $P^m = Z P^a$  (where  $P^m$  is the tensile mean load,  $P^a$  is the load amplitude, and  $Z$  is a constant), then at every point within the structure the following relationship must hold:

$$\sigma_{ij}^m = Z \sigma_{ij}^a \quad (4.14)$$

For the tensile mean load test, Eq. 4.13b reduces to

$$\begin{aligned}
 T_1^a(\omega) &= \text{temperature amplitude at } \omega \text{ for } P^m > 0 \\
 &= \frac{T_0}{\rho C_p} \left[ -\alpha I_1^a + \frac{Z}{E^2} \frac{\partial E}{\partial T} (I_1^a)^2 - \frac{Z}{G^2} \frac{\partial G}{\partial T} I_2^a \right] \quad (4.15a)
 \end{aligned}$$

For the compressive mean load test,  $P^m = -Z P^a$ , and thus

$$\begin{aligned}
 T_2^a(\omega) &= \text{temperature amplitude at } \omega \text{ for } P^m < 0 \\
 &= \frac{T_0}{\rho C_p} \left[ -\alpha I_1^a - \frac{Z}{E^2} \frac{\partial E}{\partial T} (I_1^a)^2 + \frac{Z}{G^2} \frac{\partial G}{\partial T} I_2^a \right] \quad (4.15b)
 \end{aligned}$$

This leads to:

$$T_1^a(\omega) + T_2^a(\omega) = \frac{-2\alpha T_0}{\rho C_p} I_1^a \quad (4.15c)$$

Also, provided the point under consideration is not in a state of pure shear, the following expression can be derived:

$$\psi = \frac{T_2^a(\omega) - T_1^a(\omega)}{\left( T_2^a(\omega) + T_1^a(\omega) \right)^2} = \frac{-Z \rho C_p}{2\alpha^2 T_0} \left[ \frac{1}{E^2} \frac{\partial E}{\partial T} - \frac{I_2^a}{G^2 (I_1^a)^2} \frac{\partial G}{\partial T} \right] \quad (4.15d)$$

For uniaxial stress conditions, the second stress invariant is identically zero. For this

case,  $\psi$  should be a positive constant, regardless of the magnitudes of the mean stress and stress amplitude. For biaxial loading, there is a slight variation in this expression, depending on the magnitude of the amplitude of the second stress invariant relative to the square of the amplitude of the first stress invariant. For pure-shear loading, Eq. 4.15d is no longer valid, and the following equation should be used:

$$T_2^a(\omega) - T_1^a(\omega) = \frac{2T_0 Z}{\rho C_p G^2} \frac{\partial G}{\partial T} I_2^a \quad (4.15e)$$

From Eq. 4.15c, the amplitude of the first stress invariant at every point in the specimen can be determined. By then applying Eq. 4.15d (or Eq. 4.15e for pure-shear loading), the amplitude of the second stress invariant can be calculated. With this information it is possible to determine the principal stresses,  $\sigma_A$  and  $\sigma_B$ :

$$I_1^a = \sigma_A^a + \sigma_B^a \quad (4.16a)$$

$$I_2^a = \sigma_A^a \sigma_B^a \quad (4.16b)$$

Hence,

$$\sigma_A^a, \sigma_B^a = \frac{I_1^a}{2} \pm \frac{1}{2} \left[ (I_1^a)^2 - 4I_2^a \right]^{1/2} \quad (4.16c)$$

From these data, the maximum shear stress,  $\tau_{\max} = (\sigma_A - \sigma_B)/2$ , can also be calculated. This is fine in theory, but in practice the magnitude of the mean stress effect is so small as to make accurate determination of  $\sigma_A$  and  $\sigma_B$  very difficult using current

equipment, except perhaps for a few special alloys.

### Experimental Results

A simple experiment was conducted in order to demonstrate the feasibility of detecting the mean stress effect under complex stress fields. A flat plate of 7075-T651 aluminum with a centrally located hole was used. TSA scans were conducted in the manner described in the previous paragraph. The scans were obtained along the horizontal line of symmetry of the specimen, as shown in Fig. 4. Along this line, the shear stress is zero, and so  $\sigma_A = \sigma_{11}$  and  $\sigma_B = \sigma_{22}$ . Three TSA scans were performed at each mean load, and the data were averaged. The load amplitude for all the tests was 4450 N, and mean loads of  $\pm 8900$  N were employed. By monitoring the load cell output with a digital oscilloscope, it was possible to keep the mean load and load amplitude constant to within 0.5% for all tests. The specimen cycling frequency was 25 Hz. This frequency has been found by experience to be sufficient to minimize heat conduction effects in aluminum structures such as a flat plate with a hole. In the presence of very high stress gradients (such as the region surrounding a crack tip), higher frequencies may be required to maintain adiabatic conditions. The specimen temperature was maintained at 298 K throughout the testing. The TSA line scans consisted of over 200 data points each. The spot size for these tests (i.e., the diameter of the circular region in space which is focused onto the photodetector) was approximately 0.8 mm. Data were acquired at the rate of 1 second per point. Thus, each TSA data point in every line scan is actually the average of the TSA output for 25 cycles.

The raw TSA data are shown in Fig. 5. Note that under ideal conditions, the slope of the TSA data at the edge of the hole would be infinite (i.e., a vertical line). This is

clearly not the case here. The explanation for this "edge effect" is that the photodetector is focused on a finite size region of the specimen. As the TSA scan reaches the edge of the specimen, the photodetector is focused partly on the specimen and partly on the background (which is not being stressed and hence produces zero TSA signal). As a result, the TSA data for the specimen near the edge of the hole are too low, and instead of an infinitely sharp drop-off, the TSA signal does not return to zero until the region the photodetector is focused on is completely off the specimen. Since the spot size for these tests was almost one-tenth of the total scan width, the effect is rather dramatic. It should be possible to develop an image processing algorithm that corrects for this effect, but no one has done this to date.

The TSA data were analyzed via Eqs. 4.15c and 4.15d. The data were converted from millivolts to degrees using the absolute calibration procedure discussed in Chapter 5. The resulting plot of the amplitude of the first stress invariant is given in Fig. 6, and the plot of  $\psi$  is given in Fig. 7. Considerable scatter exists in the raw TSA data on the left side of the specimen (see Fig. 5). This scatter is reflected in the data of Fig. 7. The scatter is lower on the right side of Fig. 5, but this is to be expected since the stresses (and hence the temperature and TSA amplitudes) are larger there, and so the signal-to-noise ratio is improved. The parameter  $\psi$  should be constant in regions far from the hole since the stress field is essentially uniaxial in such regions. The value of  $\psi$  for uniaxial stress is readily predicted from Eq. 4.15d:

$$\psi = \frac{-2(2800 \text{ kg/m}^3)(870 \text{ J/kg K})(-40 \times 10^6 \text{ Pa/K})}{2(23.4 \times 10^{-6} \text{ m/m/K})^2(298 \text{ K})(69 \times 10^9 \text{ Pa})^2} = 0.122 \text{ K}^{-1}$$

This predicted value for  $\psi$  under uniaxial stresses is in good agreement with the

experimental data, especially considering that the predicted value for  $\psi$  would be 0 if the classical thermoelastic equation were employed.

It is seen in Fig. 7 that there is a significant drop in  $\psi$  near the edge of the hole, followed by a return to the uniaxial stress value of  $0.122 \text{ K}^{-1}$  at the hole's edge. Although this may be nothing more than experimental scatter, it is precisely the effect one would expect if a significant tensile transverse stress reaches its peak near the edge of the hole. Such a transverse stress distribution is, of course, predicted by the theory of elasticity. Attempts were made to use the data of Figs. 6 and 7 to separate the principal stresses, but because of the large scatter in the data, no useful results were obtained. Again, the ability to determine the magnitudes of the principal stresses via mean stress effects exists in principle, but the current state of the art in TSA equipment and specimen preparation techniques does not provide data of sufficient accuracy to make this technique feasible with most engineering alloys and component geometries.

### 4.3 In-phase, Proportional, Uniaxial Loading

For uniaxial loading, Eq. 4.13 simplifies considerably. Take the stress distribution as

$$\sigma(t) = \sigma^m + \sigma^a \sin(\omega t) \quad (4.17a)$$

Equations 4.13b and 4.13c reduce to

$$T^a(\omega) = \frac{T_o}{\rho C_p} \left[ -\alpha + \frac{1}{E^2} \frac{\partial E}{\partial T} \sigma^m \right] \sigma^a \quad (4.17b)$$

$$T^a(2\omega) = \frac{-T_0}{4\rho C_p E^2} \frac{\partial E}{\partial T} (\sigma^a)^2 \quad (4.17c)$$

From Eq. 4.17b it is seen that, for a constant stress amplitude, the temperature amplitude should vary linearly with the applied mean stress. This is precisely what was originally observed by Machin et al. [11]. Considerable experimental verification of Eq. 4.17b has been performed at the National Aeronautical Laboratory in Australia [11-14]. Additional data were acquired for this report, Figs. 8-10. These data were obtained by signal averaging the TSA and load outputs with an FFT analyzer. Typically, each data point in Figs. 8-10 is the result of signal averaging for several hundred cycles. The specimens used for these tests had uniform gage lengths of circular or rectangular cross section. The computed values for  $\partial E/\partial T$ , based on the data in Figs. 8-10 (and using Eq. 4.17b), are in good agreement with values from other references (see Table 1).

Accurate measurement of the second harmonic term (Eq. 4.17c) resulting from the nonlinear thermoelastic effect was complicated by the inability to produce a pure sine wave using the closed-loop servo-hydraulic testing equipment. Some load amplitude was always present at the second harmonic, resulting in a linear thermoelastic effect at this frequency. The magnitude of the temperature amplitude due to load being present at the second harmonic was usually comparable to the magnitude of the temperature amplitude due to the nonlinear thermoelastic effect. For one set of tests, however, the load amplitude at the second harmonic was fairly small, and estimates of the nonlinear thermoelastic effect at the second harmonic were possible, Fig. 11. The resulting estimate for  $\partial E/\partial T$  is -31 MPa/K, which is somewhat lower than most handbook data on  $\partial E/\partial T$  for aluminum (see Table 1).

#### 4.4 Residual Stress Analysis

The most promising practical application for the mean stress effect is for residual stress analysis. Determination of residual stresses by absolute measurement of the temperature amplitude is exceedingly difficult because of the small magnitude of the mean stress effect relative to the stress amplitude effect. Useful results can be obtained by using a comparison technique. Although this technique has limited applications, it has already been put to practical use. The technique is described below, followed by an illustrative example.

##### Analytical Development

The technique described herein is useful for measuring residual stresses due to successive overloads of a component. Discussion will be further limited to cases in which the stress distribution is uniaxial. By using Eqs. 4.15, this technique can be easily modified to account for biaxial stress distributions. The procedure is outlined below:

1. The component to be tested must initially be in a virgin state, with no residual stresses present. A TSA scan of the component is obtained using a known mean load and load amplitude:  $P^m = Z P^a$ , where  $P^m$  is the mean load,  $P^a$  is the load amplitude, and  $Z$  is a constant. Provided the structure behaves in a linear-elastic fashion, it follows that  $\sigma^m = Z \sigma^a$  at every point within the structure. The temperature amplitude for this "original" scan is thus

$$T^{a(\omega)}|_{\text{original}} = \frac{T_o}{\rho C_p} \left[ -\alpha + \frac{Z}{E^2} \frac{\partial E}{\partial t} \sigma^a \right] \sigma^a \quad (4.18)$$

Since  $\sigma^a$  is the only unknown in this equation, it can be readily calculated.

2. An overload is applied to the component in order to induce residual stresses. After the overload, another TSA scan is performed in the region of interest. The temperature amplitude for this scan is given by

$$T^a(\omega)|_{\text{overload}} = \frac{T_o}{\rho C_p} \left[ -\alpha + \frac{\partial E}{\partial T} \frac{Z\sigma^a + \sigma^{\text{res}}}{E^2} \right] \sigma^a \quad (4.19)$$

where  $\sigma^{\text{res}}$  is the residual stress due to the overload. The assumption is implicitly made here that the overload did not change the geometry of the component, so that applying the same mean load and load amplitude as for the component in its virgin state will result in the same stress distribution. Also, it is assumed that any plastic flow occurring in the region of interest did not alter relevant material properties.

3. Subtracting Eq. 4.18 from Eq. 4.19 and dividing the result by Eq. 4.18 gives

$$\frac{T^a(\omega)|_{\text{overload}} - T^a(\omega)|_{\text{original}}}{T^a(\omega)|_{\text{original}}} = \frac{\frac{\partial E}{\partial T} \sigma^{\text{res}}}{-\alpha E^2 + \frac{\partial E}{\partial T} Z\sigma^a} \quad (4.20)$$

The residual stress is readily determined from Eq. 4.20, as it is the only unknown.

Notice that the stress amplitude plays a minor role in Eq. 4.20. In fact, for

fully-reversed loading (i.e.,  $Z = 0$ ), absolute calibration of the TSA scans is not needed in order to determine the residual stress. This is a highly advantageous situation.

### Experimental Results

In order to test the feasibility of thermographic residual stress analysis via Eq. 4.20, a C-specimen of Ti-6Al-4V alloy was used. The specimen and loading geometry are given in Fig. 12. This specimen was not arbitrarily chosen; in fact, the specimen was designed to simulate the stress distribution occurring in a high-speed centrifuge. The industrial sponsors of this research project were interested in knowing the residual stress developed at the midsection of the C-specimen (line A-B of Fig. 12) as a result of applying a given force overload. Special strain gages having high-strain capability were mounted in this region, and TSA scans were performed along line A-B between the strain gages. The specimen cycling frequency for these scans was 25 Hz, the load amplitude was 6.67 kN, and the mean load was 17.8 kN. Samples of some of the raw TSA data are shown in Fig. 13. It is seen that the applied overloads did alter significantly the TSA amplitude along line A-B. Multiple overloads were applied at each overload level, and TSA scans were taken after specific numbers of overloads.

Assuming that plastic flow does not have a significant effect on the thermoelastic parameter ( $\alpha/\rho C_p$ ), and having the raw data of Fig. 13, the residual stresses in the C-specimen can be determined via Eq. 4.20. The results are shown in Fig. 14, where the residual stress has been plotted versus total accumulated plastic strain (measured with the strain gages). The residual stresses are plotted against the number of applied overloads in Fig. 15. The residual stress tends to increase at first with increasing numbers of overload cycles, but after a few cycles (roughly from 5 to 20) the residual stress stabilizes. Based on the maximum scatter in the average values of the data from

the TSA line scans, these residual stress estimates should have a maximum error of approximately  $\pm 25$  MPa, provided that prior plastic strain does not affect the material properties. This is comparable to the accuracy obtainable with most other techniques [33]. It should be pointed out that the mean stress effect is much larger in Ti-6Al-4V than in most other metals [10]. Thus, the accuracy with most alloys will likely be worse than  $\pm 25$  MPa.

In order to verify that the changes in TSA amplitude were not due to the effects of plastic flow on the material properties, tests were performed on a uniform cylindrical specimen of the same alloy. The specimen was scanned in its virgin state and after overloading to known amounts of plastic strain (the axial strain being monitored and controlled with a clip-gage extensometer). Since the specimen was of uniform cross section within the gage region, no residual stresses should be generated by plastic flow in this region. Some reduction in cross-sectional area did occur, however, and it is assumed that the specimen volume remained constant during this plastic flow. Thus,  $A_i = A_o L_o / L_i$ , where  $A_o$  and  $L_o$  are the original cross-sectional area and extensometer gage length, respectively, and  $A_i$  and  $L_i$  are these same quantities after performing an overload. Knowing  $A_o$ ,  $L_o$ , and the final gage length after overloading,  $L_i$ , the reduced cross-sectional area,  $A_i$ , can be estimated. This reduced cross-sectional area was used to determine the stress amplitudes for the TSA scans performed after the overloads. The reduced data are shown in Table 2. It is seen that small amounts of plastic flow do not cause significant changes in the thermoelastic parameter,  $\alpha/\rho C_p$ , for this material. In fact, the observed variations might well be attributable to experimental scatter, since the largest observed change in the thermoelastic parameter was only 0.75 percent.

### Analysis of the Effects of Plastic Strain on Residual Stress Accuracy

Wong et al. have also performed residual stress analysis via the mean stress effect [15]. They noted a significant deviation from theoretical predictions in regions where significant compressive plastic flow had occurred. No error was noticed in areas of tensile plastic flow. The material tested was 2024-T351 aluminum. Because of this finding, and the scatter in data of Table 2, an error analysis on the potential effects of prior plastic strain is warranted. The analysis here will be limited to assuming that plastic strains can affect either the thermal expansion coefficient (see, for example, Ref. 34) or the specific heat. Similar analyses could be performed for the effects of prior plastic strain on the  $E$ ,  $\partial E/\partial T$ , or any combination of these material parameters.

Case 1 – Change in thermal expansion due to prior plastic strain. It is assumed that the thermal expansion has changed after applying the overload force, this change being due to plastic strains. Let the new value for thermal expansion after the overload be  $(1+x)\alpha$ , where  $\alpha$  is the original value. Substituting this expression in place of  $\alpha$  in Eq. 4.19 and then substituting the result into Eq. 4.20 leads to

$$\sigma^{\text{res}}(\text{change in } \alpha) = \sigma^{\text{res}}(\text{normal}) - \frac{x \alpha E^2}{\partial E / \partial T} \quad (4.21)$$

where  $\sigma^{\text{res}}(\text{normal})$  is the "normal" estimate for residual stress, as given by Eq. 4.20.

Case 2 – Change in specific heat due to prior plastic strain. The analysis is the same as before. We assume that the specific heat after overloading has changed to  $(1+x)C_p$ , where  $C_p$  is the specific heat of the virgin material. Performing the same error analysis as for Case 1 leads to the following:

$$\sigma^{\text{res}}(\text{change in } C_p) = (1+x)\sigma^{\text{res}}(\text{normal}) - \frac{x \alpha E^2}{\partial E / \partial T} + (1+x)xZ\sigma^a \quad (4.22)$$

For the Ti-6Al-4V specimen with the previously stated loading conditions and with  $x$  equal to 0.008, a maximum error of approximately 21 MPa in the residual stress estimate is predicted for Case 1, and a maximum error of 25 MPa is predicted for Case 2. These values are within the range of scatter noted in the raw TSA data.

For alloys that do show significant changes in elastic and thermal properties with accumulated plastic strain, thermographic residual stress analysis would be difficult. It is worth noting that other residual stress analysis techniques have similar problems. For example, the Barkhausen noise technique is unable to separate the effects of prior plastic deformation from residual stresses. It is also limited to ferromagnetic materials. X-ray diffraction and ultra-sonic techniques are strongly affected by grain boundaries and crystallographic orientation [15].

In summary, TSA shows promise as a new technique for residual stress analysis. Although the technique described in this report is restricted to laboratory conditions and components that are initially free of residual stress, the technique should nonetheless prove useful as a means for rapidly determining the effects of force overloads on the residual stress patterns in regions of high stress.

## 5. THE ENHANCED TSA EQUATION

Many important physical phenomena were neglected in the development of the classical TSA equation (Eq. 2.6). To obtain the enhanced TSA equation, it is assumed that emissivity, temperature and background flux vary with time. From Eq. 2.5 it follows that

$$\frac{dS}{dt} = R \frac{d\phi_i}{dt} = 3eRBT^2 \frac{dT}{dt} + RBT^3 \frac{de}{dt} + R \frac{d\phi_b}{dt} \quad (5.1)$$

Changes in emissivity can occur because of nonuniform spatial emissivity combined with specimen motion. Such effects will show up most strongly at the specimen cycling frequency,  $\omega$ , which is the frequency at which thermoelastic effects are largest. These emissivity effects can be quite dramatic if inadequate surface coatings are employed. Temperature changes,  $dT/dt$ , are not limited to thermoelastic, thermoplastic and heat conduction effects, but can also be caused by temperature gradients across the specimen combined with specimen motion. Changes in background flux with time will normally be due to stochastic processes (i.e., white noise effects).

For simplicity of demonstration, the classical thermoelastic equation will be used instead of the nonlinear thermoelastic equation. Substituting Eq. 3.8 into 5.1 and including other relevant terms results in

$$\begin{aligned} \frac{dS}{dt} = & RB T_0^3 \left( \frac{-3e\alpha}{\rho C_p} \frac{dI_1}{dt} + \frac{de}{dy} \frac{dy}{dt} \right) \\ & + 3eRB T_0^2 \left( \frac{1}{\rho C_e} \frac{dW_p}{dt} + \frac{dT}{dy} \frac{dy}{dt} + K' \nabla^2 T \right) + R \frac{d\phi_b}{dt} \end{aligned} \quad (5.2)$$

where  $y$  is the direction perpendicular to the angle of view of the photodetector. Thus,  $de/dy$  is the emissivity gradient in the  $y$ -direction, and  $dT/dy$  is the temperature gradient in the  $y$ -direction. The term  $dy/dt$  represents the rate of displacement of a material point located on the specimen with respect to the spatial region the photodetector is focused on.

Consider a specimen of uniform cross section undergoing loading in a direction perpendicular to the angle of view of the photodetector. This arrangement would exist, for example, if the specimen was being loaded in the vertical direction and the angle of view of the photodetector was parallel to the horizontal. In fact, this is the testing arrangement that existed for all data reported in this report. Assuming the load frame and gripping are far more rigid than the specimen, the specimen's rate of vertical deflection,  $dy/dt$ , at a distance  $L$  from the upper rigid grip is given by

$$\frac{dy}{dt} = \frac{L}{AE} \frac{dP}{dt}$$

where  $A$  is the specimen cross-sectional area,  $P$  is the applied load, and  $E$  is the elastic modulus of the material. Equation 5.2 is implicitly based on the assumption that the photodetector spot size is infinitesimal. This is not the case in practice, and an accurate analytical description of emissivity and temperature gradient effects would involve

integrating the terms  $(de/dy)(dy/dt)$  and  $(dT/dy)(dy/dt)$  over the finite spatial region the photodetector is focused on.

Typically, emissivity and temperature gradient effects become larger as the spot size becomes smaller. This has important implications for microscopic stress analysis. In particular, a very uniform spatial emissivity would be necessary. In general, any specimen coating employed must have an average particulate size that is much smaller than the minimum desirable photodetector spot size. Also, for curved surfaces, it is important that the emissivity be independent of the viewing angle. Many coatings show significant variations in emissivity with respect to angle of incidence. Other coating effects that have not even been touched upon in this report are infrared transmissivity and reflectivity. If these properties vary spatially or with angle of incidence, this will result in "false" TSA signals similar to those experienced when emissivity gradients are present.

Based on Eq. 5.2, thermoelastic and emissivity effects are proportional to the cube of the nominal temperature whereas thermoplastic, temperature gradient and heat conduction effects are proportional to the temperature squared. The heat conduction effect is a bit misleading. If the heat conduction is a stabilized dynamic effect due to the thermoelastic effect, the magnitude of the heat conduction will be proportional to the thermoelastic temperature change, which in turn is proportional to the nominal temperature. Such heat conduction effects will effectively be proportional to the temperature cubed, just as the thermoelastic effect is. Also note from Eq. 5.2 that emissivity effects are proportional to the temperature cubed. Thus, it is essential to maintain a uniform spatial emissivity, regardless of the specimen temperature. Temperature gradient effects, on the other hand, are proportional to the temperature squared. Thus, assuming for the moment that one is interested in thermoelastic effects

only, Eq. 5.2 implies that larger temperature gradients can be tolerated at higher temperatures, all other quantities remaining equal. This is a bit of an oversimplification since all other quantities will not remain equal as the nominal specimen temperature is changed. For example, the elastic modulus usually decreases with increasing temperature, and hence the specimen displacement for a given stress increment increases at higher temperatures.

Changes in background radiation with time will normally be due to stochastic processes, thus leading to a "white noise" effect. The exact magnitude of  $d\phi_B/dt$  depends on so many parameters (e.g., photodetector angle of view, infrared lens characteristics, temperature and emissivity of camera housing, etc.) that accurate analytical quantification is virtually impossible. This effect will show up in the TSA output in combination with other noise effects such as electrical noise and thermal noise from the specimen itself.

The static thermal flux from the specimen, which for TSA purposes is a thermal noise, is given by Eq. 2.2. Dividing Eq. 5.2 by Eq. 2.5 (modified), and neglecting background radiation effects, provides an indication of the idealized thermal signal-to-noise ratio:

$$\frac{\frac{dS}{dt}}{S_{\text{static}}} = \frac{-3\alpha}{\rho C_p} \frac{dI_1}{dt} + \frac{\frac{de}{dy} \frac{dy}{dt}}{e_{\text{ave}}} + \frac{1}{T_0} \left( \frac{1}{\rho C_e} \frac{dW_p}{dt} + \frac{dT}{dy} \frac{dy}{dt} + K' \nabla^2 T \right) \quad (5.3)$$

where  $e_{\text{ave}}$  is the average emissivity within the region of interest during the sampling time. It is seen that the thermoelastic signal-to-noise ratio is independent of temperature, provided  $\alpha$ ,  $\rho$ ,  $C_p$  and  $e$  do not change significantly with temperature (a condition that is not always met in practice). Thus, under ideal testing conditions, the

same stress resolution should be obtainable over a wide range of temperatures. The thermoplastic signal-to-noise ratio is inversely proportional to temperature; consequently, the minimum resolvable plastic-work energy is expected to decrease with increasing temperature. These conclusions are valid provided the incident flux rate is kept low enough to keep the photodetector within its linear operating range, and provided the thermal noise from the specimen is the factor limiting the resolvable TSA signal. In practice, this is often not the case. In particular, for low temperature testing, the magnitude of the specimen photon flux (be it the dynamic flux due to thermoelastic effects or the static flux from the specimen) decreases rapidly, and electrical noise and/or background photon flux are the factors limiting resolvable stress rather than the thermal noise from the specimen.

Some practical implications of Eqs. 5.2 and 5.3 are now discussed. First of all, it can be seen that the TSA output should be linearly related to the specimen stress amplitude, all other factors remaining constant, and no mean or residual stresses being present:

$$S^a(\omega) = \left[ \frac{-3 e R B \alpha T_0^3}{\rho C_p} \right] \sigma^a(\omega) \quad (5.4)$$

This has been found to be the case to a very high degree of accuracy. This is demonstrated in Fig. 16 for a cylindrical specimen composed of 1020 steel coated with a thin layer of ultra-flat black paint. Similar results were obtained with other metals.

Provided inter-specimen heat conduction and heat transfer to the surroundings are minimized, the TSA amplitude for a constant stress amplitude should be independent of frequency. This statement can be seriously in error at very high testing frequencies or

with thick coatings [35]. Figure 17 shows the results for a 304 stainless steel specimen coated with a thin layer of high-temperature ultra-flat black paint. Data were obtained at a single point on the specimen, and the TSA output was monitored using an FFT spectrum analyzer. Each data point in Fig. 17 is actually the result of performing several tests at different stress amplitudes and taking a linear curve fit of the plot of TSA output versus stress amplitude for that particular frequency. Thus, the fact that the data do not form a smooth curve is unlikely to be due to random noise. The "scatter" may be due to heat transfer effects in the coating. Such heat transfer effects are known to be capable of producing significant changes in the TSA calibration factor,  $S^a/\sigma^a$ , for small changes in frequency, especially if the coating is of varying thickness or of nonhomogeneous composition [35]. Below approximately 3 Hz, the TSA signal decreases rapidly. This is due to the filtering characteristics of the preamplification electronics in the SPATE system. Very similar results (i.e., always a sharp decrease in TSA signal below 3 Hz) were obtained with a variety of other specimen shapes, sizes and alloys. These filtering effects have serious implications for elastic-plastic analysis, as discussed in the next chapter.

Another important implication of Eq. 5.2 is the possibility to perform absolute calibration of thermoelastic and thermoplastic effects at any temperature provided that all relevant parameters are known. Ideally, one would like to be able to take  $R$  and  $D^*$  as constants. This is reasonable provided that the incident photon flux rate is kept within the linear range of the photodetector. TSA calibration plots of  $S^a(\omega)$  versus  $\sigma^a$  are given in Fig. 18a for 1020 steel at several temperatures. The estimates for  $3eRB$  (using the data of Fig. 18a, the material property data of Table 1, and Eq. 5.4) are given in Fig. 18b, where additional data from other tests are also shown. From  $-11^\circ\text{C}$  to  $55^\circ\text{C}$ , and using ultra-flat black paint, the apparent value for  $3eRB$  is seen to

increase slightly with increasing temperature. This could be due to changes of  $\epsilon$ ,  $R$ ,  $\alpha$ ,  $C_p$ , or  $\rho$  with respect to the specimen temperature. The exact cause of the increase is not known, but the effect is small (about 0.1% increase in  $3\epsilon RB$  per degree C) when compared to the fact that the TSA output is dependent on the cube of temperature (which results in approximately a 1% increase in the TSA output per degree C for the temperature range in Fig. 18b).

Further ramifications of Eqs. 5.2 and 5.3 are given in Chapters 6 and 7. A complete verification of these equations, including quantitative analyses of emissivity and temperature gradient effects, is beyond the intended scope of this report.

## 6. CYCLIC PLASTICITY ANALYSIS

### 6.1 Analytical Development

Cyclic plasticity affects the TSA output in two major ways. First of all, the generation of irreversible plastic-work energy (which is hereafter assumed to be entirely converted into irreversible heat) will create a unique thermal profile. Secondly, the plastic-work energy results in self-heating of the specimen. This in turn affects the magnitude of the TSA outputs due to thermoelastic effects, which are proportional to the cube of temperature. Equation 5.2 is used as the starting point for cyclic plasticity analysis. When emissivity, temperature gradient, heat conduction, and background flux effects are ignored, Eq. 5.2 reduces to

$$\frac{dS}{dt} = -\frac{3eRB\alpha}{\rho C_p} T_o^3 \frac{dI_1}{dt} + \frac{3eRB}{\rho C_e} T_o^2 \frac{dW_p}{dt} \quad (6.1)$$

For materials exhibiting significant nonlinear thermoelastic effects, Eq. 6.1 should be appropriately modified using the nonlinear thermoelastic equations developed in this report. More will be said on this later in the chapter.

Although Eq. 6.1 is general enough to be applied to any stress distribution, the analysis here will be limited to uniaxial stress conditions. This is done for ease of demonstration and also because all cyclic plasticity testing we have performed to date has been limited to uniaxial conditions. Furthermore, the analysis will be confined to sinusoidal, fully-reversed, load-controlled cycling. The stress as a function of time is given by

$$I_1(t) = \sigma(t) = \sigma^a \sin(\omega t) \quad (6.2)$$

The TSA amplitude due to reversible thermoelastic effects is therefore given by

$$S_{\text{rev}}^a(\omega) = -\frac{3eRB\alpha}{\rho C_p} T_0^3 \sigma^a \quad (6.3)$$

Provided the specimen temperature and material properties remain constant, the TSA amplitude at the specimen cycling frequency due to thermoelastic effects will be proportional to the stress amplitude. However, cyclic loading at stresses above the proportional limit will result in increases in  $T_0$  due to self-heating of the specimen. This in turn results in an increase in the value of  $S^a(\omega)$  and for a given  $\sigma^a$ .

In order to understand the effects of cyclic plasticity on the TSA output, it is instructive to look at the geometry of a hysteresis loop. Consider the shape of a hysteresis loop for a "generic" isotropic material, Fig. 19. Note that  $W_p$  is the area within the hysteresis loop:  $W_p = \int \sigma d\varepsilon_p$ , where  $\varepsilon_p = \varepsilon - \sigma/E$ . From A to B in Fig. 19, the material experiences a combination of elastic and plastic strains. Elastic unloading occurs from B to C, and no additional plastic-work energy is accumulated during this time. From C to D the material again experiences elastic and plastic strains, and from D to E the material once again unloads elastically. For sinusoidal load-controlled cycling (Fig. 20a), it follows that the TSA signal due to thermoelastic effects is also sinusoidal, but 180° out-of-phase with the stress waveform, Fig. 20b. This is assuming  $\alpha$  is greater than zero. If  $\alpha$  is less than zero, the TSA signal due to thermoelastic effects will be in-phase with the stress. The plastic-work energy, which is proportional to the irreversible temperature change, is shown in Fig. 20c. From this

waveform it is anticipated that irreversible plasticity effects will show up in the TSA output at multiple frequencies. The exact nature of the TSA output in the frequency domain will depend on the sampling time involved. This is because the waveform in Fig. 20c is not periodic; consequently, when this waveform is converted from the time domain to the frequency domain via a Fast Fourier Transform, the amplitudes of the frequency components depend on both the sampling time and the shape of the waveform [36]. If data are acquired for a total period,  $\Delta t$ , of one single cycle ( $\Delta t = 2\pi/\omega$ ), the smallest frequency discernible with an FFT algorithm is precisely  $\omega$ , and the TSA output due to thermoplastic effects will show up potentially at every frequency in the FFT analysis:  $\omega, 2\omega, 3\omega, \dots, N\omega/2$ , where  $N$  is the number of data points gathered during the sample time [36].

The preamplification stage present in the SPATE system used in this research effectively acts as a high-pass filter. Consider a mathematically ideal high-pass filter. Such a filter passes all frequencies above 0 Hz and completely attenuates the 0 Hz static component. With such an ideal filter, the static temperature dwells in the thermoplastic temperature response (i.e., B to C and D to E in Fig. 20c) would be completely eliminated from the TSA output, Fig. 20d. Note that for each cycle of TSA output caused by thermoelastic effects (A to E in Fig. 20b), there would be two cycles of TSA output due to thermoplastic effects (A to B and C to D in Fig. 20d). In other words, the TSA output due to irreversible thermoplastic effects ( $S_{\text{irrev}}$ ) would have a fundamental frequency equal to twice the fundamental frequency of the TSA output due to thermoelastic effects. In equation form,

$$S_{\text{irrev}} = S^2(2\omega) \sin(2\omega t + \phi_2) + S^2(4\omega) \sin(4\omega t + \phi_2) + \dots \quad (6.4)$$

The exact magnitudes of the TSA amplitudes and the associated phase angles would depend on the hysteresis loop size and shape and the nominal specimen temperature. Unfortunately, any real filter has a finite decay time. As a result, the simplistic response of Fig. 20d is not observed when using the SPATE system, and the actual TSA output due to combined thermoelastic and thermoplastic effects becomes a complex function of the material, the filtering characteristics of the SPATE preamplification stage, and the sampling time. For this reason, quantitative verification of the thermo-elastic-plastic equation from first principles was not possible in this research. Even so, useful empirical relationships between the plastic-work energy and the TSA output were developed, as shown later in this chapter. These results provide good qualitative verification of the ideas proposed herein.

## 6.2 Experimental Setup

Cyclic plasticity analyses were performed on 1020 steel and 6061-T6 aluminum. Thermal and mechanical constants for these materials are given in Table 1. All tests were conducted on cylindrical specimens. Strains were monitored using 10 mm or 12.5 mm gage-length extensometers. These extensometers have strain resolutions of about 20 microstrain. The SPATE output was monitored using a Nicolet 660A FFT spectrum analyzer. A hysteresis loop was recorded for each test at the midpoint of the FFT sampling. The hysteresis loop was recorded using either an HP 7090A digital plotter or a Macintosh II computer equipped with appropriate A/D hardware and software. Specimen temperature was monitored using a J-type thermocouple.

Tests on 1020 steel were performed at nominal specimen temperatures of 0, 8, 25, and 55 °C. Tests on 6061-T6 aluminum were performed at a nominal specimen temperature of 25 °C. For the tests on 1020 steel, the specimens were mounted in a

small environmental chamber that was connected to a source of constant velocity air flow at the desired test temperature. In order to avoid moisture condensation on the specimen during the low-temperature tests, the air flow was passed through a desiccant before arriving at the specimen. For both the low-temperature tests (0 °C and 8 °C) and high-temperature tests (55 °C), advantage was taken of the large thermal mass of the steel hydraulic grips used to hold the specimens. This was done by heating/cooling the grips to the desired test temperature. The grips thus acted as a constant-temperature heat source, and it was possible to keep the specimen temperature constant to within about  $\pm 0.5$  °C (except, of course, during elastic-plastic conditions, when the specimen heated up because of irreversible thermoplastic effects).

One annoyance in using the Nicolet 660A FFT spectrum analyzer is that it has a "settling time" that depends on the frequency range chosen. The tests reported herein were performed at a specimen cycling frequency of 3 Hz, and the FFT device was set on its 50 Hz range. On this setting, the maximum measurable frequency component is 50 Hz, the minimum is 0.125 Hz, and the "settling time" is 8 seconds, which corresponds to the sampling time for a single "sweep" of the FFT analyzer on this frequency setting (the sweep time is the inverse of the minimum measurable frequency - see Ref. 36). Thus, at least 24 cycles of loading had to be continuously applied to the specimen before TSA sampling could even begin. In one way this was advantageous since this allowed enough cycles for the material to approach a cyclically stabilized state with respect to its mechanical properties. After the "settling time", sampling was performed for a minimum of 50 additional cycles at high plastic strain amplitudes, and for as many as 100 additional cycles at low plastic strain amplitudes. During the sampling time, the specimen temperature was always observed to increase, implying that a stabilized cyclic thermal response had not been achieved in these tests.

The relatively low cycling frequency of 3 Hz was chosen for two reasons. First of all, this helps to minimize the magnitude of the specimen self-heating for a given sampling time. Secondly, the particular closed-loop servo-hydraulic testing equipment used in this research had much better response (in terms of the harmonic purity of the sine wave produced) at lower frequencies when cycling a specimen within the elastic-plastic regime.

### 6.3 Experimental Results

Figure 21 shows an FFT analysis of both the load and TSA signals for one of the elastic-plastic tests performed on 1020 steel under sinusoidal load control. Although no significant load amplitudes existed at the second, fourth, or sixth harmonics, sizeable TSA amplitudes occurred at these frequencies. This is in good qualitative agreement with the analytical developments of Section 6.1. Note the presence of significant load amplitude at the third harmonic. Load amplitudes at the third harmonic were always present in the load-controlled tests. This occurred because the closed-loop servo-hydraulic system used in this research was not capable of producing a perfect sine wave. Fortunately, very little load amplitude was ever present at the second or fourth harmonics in these tests, so accurate measurement of the TSA output due to cyclic plasticity effects was still possible. Only 30 percent of the TSA output at  $5\omega$  in Fig. 21 can be accounted for by the magnitude of load amplitude at that frequency. The cause for this discrepancy could be due to any number of things (asymmetry between the tensile and compressive halves of the hysteresis loop, cyclic creep phenomena, filtering effects of the SPATE preamplification electronics, etc.). No definite explanation is available at this time.

By recording hysteresis loops at different load/strain amplitudes, it was possible to

determine the stabilized cyclic stress-strain characteristics of the materials tested. The plastic strain amplitude (equal to one-half the width of the hysteresis loop at zero load) was determined for all the tests along with the plastic-work energy (the area within the hysteresis loop). These two quantities are plotted against one another in Figs. 22-23. Data for the 0 °C tests on steel are not shown. The data for both materials can be fit to a power-law relationship, at least within the range of plastic strain amplitudes tested. Cyclic stress-strain curves (stress amplitude versus total strain amplitude) for both materials were also determined, Figs. 24-25. The method used for constructing these curves is given in Ref. 37. Results for both load-controlled and strain-controlled tests on 1020 steel at room temperature are given in Figs. 22b and 24b. The data for both control modes are in excellent agreement with one another, implying that the control mode does not affect the underlying mechanical strength properties of 1020 steel, at least for 25 °C and 3 Hz.

It is also clear from Figs. 22a and 24a that the cyclic stress-strain response for the 1020 steel is temperature dependent. In particular, the material shows decreasing resistance to plastic deformation (for a given stress amplitude) with increasing temperature. Most other metals show a similar response. Such strength-temperature relationships are extremely important if one is attempting to obtain quantitative information on the plastic strain amplitudes via TSA techniques. If calibration data such as given in Figs. 22 through 25 are known for the materials of interest and over the temperature ranges of interest, then accurate estimation of plastic strain amplitudes under uniaxial loading should be possible. For biaxial conditions, it would be necessary to construct biaxial stress-strain curves as well as biaxial counterparts to Figs. 22 and 23 by using some sort of effective strain parameter. Such concepts have been under development for many years in the field of multiaxial fatigue, and useful

ideas could probably be gained from the available literature in this area (see, for example, Refs. 38-40).

If the basic shape of the hysteresis loop remains constant for increasing hysteresis loop size, the irreversible temperature amplitude versus time should also keep the same shape. This in turn implies that the FFT of the SPATE's photodetector output should have the same form for any magnitude of plastic-work energy, even in the presence of attenuation effects due to the preamplification circuitry. Put another way, if the geometric shapes of the hysteresis loops are the same for all magnitudes of plastic-work energy, the TSA outputs from the SPATE system at the second and fourth harmonics,  $S^a(2\omega)$  and  $S^a(4\omega)$ , should be linearly proportional to  $W_p$ . A linear relationship between  $S^a(2\omega)$  and  $W_p$  was in fact observed for 1020 steel, at least within the range of experimental scatter, as shown in Fig. 26. Note that these are raw data that have not been corrected for the effects of specimen self-heating during the FFT sampling time.

From the hypothesis of the invariance of hysteresis loop shape with respect to  $W_p$ , it is expected that the ratio  $S^a(2\omega)/S^a(4\omega)$  should be constant for all magnitudes of  $W_p$ , provided nonlinear thermoelastic effects are insignificant. Accurate measurement of  $S^a(4\omega)$  was only possible for the tests on 1020 steel that resulted in large plastic strain amplitudes. For these tests, the ratio  $S^a(2\omega)/S^a(4\omega)$  was found to be constant, at least within the range of experimental scatter, Fig. 27.

Both the load- and strain-controlled tests for 1020 steel at 25 °C show a linear relationship between  $S^a(2\omega)$  and  $W_p$ , but the strain-controlled tests have a different slope from the load-controlled tests (see Fig. 26). This is not surprising since, although the hysteresis loops for load- and strain-controlled tests have the same shape (see the cyclic stress-strain curve of Fig. 24b), the plastic-work energy is generated at different rates for these two control modes. For the load-controlled tests, considerable

plastic-work energy occurs just before the peak load is reached. This is because 1020 steel (like most materials) shows a rapid increase in plastic strain with small increases in stress for stresses above the yield strength. For strain-controlled tests, the development of plastic-work energy is more gradual. It follows that for the same value of  $W_p$ , the rate of generation of irreversible plastic-work energy will be different for the two control modes, and hence so will be the values of the TSA amplitudes and phase angles. Also, the strain-controlled tests will inevitably contain some load amplitude at  $2\omega$  (as well as higher harmonics), and this results in a thermoelastic effect at this frequency. This thermoelastic effect in turn interacts with thermoplastic effects occurring at  $2\omega$ . This thermoelastic-thermoplastic interaction will also affect the slope of the  $S^a(2\omega)$  versus  $W_p$  plot. This difference in the TSA output for load versus strain control could be useful in assessing the true nature of cyclic plasticity in complex members.

The form of the TSA output for 6061-T6 aluminum under elastic-plastic conditions is more complicated than for 1020 steel. This is because this alloy shows a significant nonlinear thermoelastic effect at the second harmonic, as was discussed in Section 4.3 and shown in Fig. 11. Also, it was necessary to perform these tests under strain control because of the nearly flat-top yielding of this material (i.e., a very rapid increase in plastic strain amplitude for small increases in stress amplitude - see Fig. 25). The TSA amplitude at  $2\omega$  is plotted against the stress amplitude in Fig. 28a and against the plastic-work energy in Fig. 28b. Although exact quantitative analyses of these data were not possible (again because of the filtering effects of the preamplification stage in the SPATE's signal-conditioning electronics), intuitive statements can be made based on the theories developed in this report:

- a) At stress amplitudes within the elastic regime, the TSA output at  $2\omega$  is

due to nonlinear thermoelastic effects. This hypothesis can be quantitatively verified, as was done in Fig. 14. b) For small plastic strain amplitudes, nonlinear thermoelastic and thermoplastic effects undergo destructive interference, and the magnitude of  $S^a(2\omega)$  decreases. c) At still higher plastic strain amplitudes, thermoplastic effects dominate over nonlinear thermoelastic effects (and thermoelastic effects due to any load occurring at  $2\omega$ ), and so  $S^a(2\omega)$  increases continuously with further increases in stress amplitude.

Quantitative verification of this hypothesis would require measuring the amplitude and phase of the stress, plastic-work energy and photodetector output voltage (without any filtering) at frequencies of  $\omega$  and  $2\omega$ .

Analysis of  $S^a(\omega)$  for elastic-plastic loading has not been found to be in strict agreement with idealized theory. Within the elastic domain,  $S^a(\omega)$  is linearly related to  $\sigma^a$ , but for stress amplitudes beyond the cyclic yield strength,  $S^a(\omega)$  increases rapidly. Some of this nonlinearity is due to specimen self heating, and this term can be accounted for via Eq. 5.2. As shown in Fig. 29 for the case of 1020 steel at 8 °C, theoretical predictions for  $S^a(\omega)$  are generally below the experimental data. Not surprisingly, the magnitude of the disagreement increases at larger plastic strain amplitudes. The reason for this discrepancy between theory and experiment is believed to be due to a combination of effects - namely heat conduction from the specimen to the environment, and the less-than-ideal filtering characteristics of the SPATE's preamplification electronics. In Fig. 29, the predictions for  $S^a(\omega)$  based on perfectly adiabatic specimen response (i.e., no heat transfer to the surroundings) are shown along with the predictions based on the actual measured specimen temperatures. The difference between these two data sets implies that significant heat transfer is occurring

from the specimen to the surroundings.

As further verification that the SPATE's preamplification electronics is at least partially responsible for the discrepancy between theory and experiment observed in Fig. 29, an impulse test was performed on the SPATE system. That is to say a step change in the photon flux coming from the target was created, and the decay characteristics of the TSA output were recorded, Fig. 30. The impulse was achieved by rapidly going from a low-emissivity target to a high-emissivity target. This was accomplished by having the infrared camera focused on a target composed of ordinary white paper and then quickly switching to an object coated with ultra-flat black paint. As seen in Fig. 30, the SPATE's preamplification electronics has a very long decay time indeed, and it is not surprising that the TSA output disagrees significantly from the anticipated response for a mathematically ideal high-pass filter.

Figures 31 and 32 show further results of the effects of cyclic plasticity on  $S^a(\omega)$  for 1020 steel and 6061-T6 aluminum at 25 °C. From these figures it is seen that considerable cyclic plasticity did not alter significantly the value for the thermoelastic parameter. This is in agreement with assumption A4 of Chapter 3. The thermoelastic parameter (equal to  $\alpha/\rho C_p$  for the case of fully-reversed loading) is proportional to the quantity  $S^a(\omega)/\sigma^a$  for data within the elastic range of the material.

#### 6.4 Chapter Summary

This chapter has provided an intuitive model for the effects of cyclic plasticity on the TSA output. The model predicts that cyclic plasticity effects should show up at the even harmonics ( $2\omega$ ,  $4\omega$ , ...) when an ideal low-frequency, high-pass filter is present in the photodetector signal-conditioning electronics. In the absence of any filtering and in the absence of significant heat transfer from the specimen to the surroundings,

thermoplastic effects should show up at all harmonics, including the specimen cycling frequency. This assumes a FFT sampling time equal to the specimen cycling period. The results using the SPATE system were found to be between these extremes. This was to be expected because of the presence of real (as opposed to mathematically ideal) high-pass filtering in the SPATE signal-conditioning electronics. This filtering has a finite decay time, and this in turn results in data that lie between the two mathematically perfect extremes. The inevitable occurrence of heat transfer between the specimen and the environment also played a role in the measured discrepancy between idealized theory and experiment.

It would be helpful to develop a new TSA system that avoids the imperfect filtering characteristics of the SPATE's preamplification circuitry. The thermoplastic equation could then be verified accurately from first principles, including measurement of both the TSA amplitudes and phase angles at all the relevant frequencies. Digital data acquisition with subsequent post-processing would also be desirable. In this way data could be acquired for a single cycle only, or for any number of cycles desired, and digital analysis of the data (in the form of FFT analysis or other techniques) could be performed. Single-cycle analysis has the advantage that the specimen does not heat up significantly during the test time. Also, this could be a useful way to measure the stored-energy of cold work during the first cycle of overload of a virgin specimen.

Clearly, much more research needs to be performed in the area of thermographic stress analysis of elastic-plastic material response, and a thorough understanding of thermo-elastic-plastic interactions is still many years away. This chapter provides many crucial concepts that can be used as a starting point for further research in this field.

## 7. HIGH-TEMPERATURE STRESS ANALYSIS

This section of the report covers the most recent work done on high-temperature stress analysis using TSA, along with solutions to problems encountered in the previous year. Based on Eq.5.3, the minimum resolvable stress using TSA should be virtually independent of temperature. This statement is valid provided that thermal noise from the specimen is the factor limiting the resolvable stress. Meeting this criterion of "thermal-noise limitation" stress resolution has been difficult because of the occurrence of many new phenomena at high temperatures. In addition, phenomena that are normally only of minor concern at room temperature (emissivity and temperature gradient effects, for example), have been found in the beginning to be almost insurmountable problems at high temperatures. The most important of these phenomena which have been isolated during the past two years are discussed below along with suggested methods for avoiding them.

### 7.1 Chromatic Aberration

This phenomenon will occur when a real lens is used to focus light of significantly different wavelengths. The lens will not simultaneously focus all the wavelengths properly because of variations of the index of refraction of the lens material with wavelength. The end result is a distorted image. The simple solution to this problem is to use a narrow band-pass optical filter. A 1-mm thick glass slide was placed between the specimen and the camera during testing. Since ordinary glass does not transmit significant amounts of radiation beyond 3  $\mu\text{m}$ , and the germanium lens used in the SPATE infrared camera does not transmit radiation of wavelengths shorter than 2  $\mu\text{m}$

[46], this results in a 2- to 3- $\mu\text{m}$  band-pass filter. This filter gives good results for temperatures exceeding approximately 500°C. The reason for this is explained later in this chapter.

A new focus curve must be determined for the infrared camera before it can be properly used with this 2- to 3- $\mu\text{m}$  filter. This can be accomplished by taking a uniform flat-plate specimen and coating a small region of the specimen with a thick, thermally insulating layer (region BCD of Fig. 33). The entire specimen is then coated with a thin layer of high-temperature paint. When the specimen is cyclically loaded, little or no temperature variation is seen in region BCD, whereas large temperature variations are observed in regions AB and DE. If the infrared camera is properly focused, a line scan from A to E in Fig. 33 will have the approximate geometry of a square wave. If the camera is out of focus, the TSA line scan will appear blurred. Examples of in-focus and out-of-focus TSA scans are given in Fig. 34 for a region of a test specimen corresponding to CDE in Fig. 33. Notice that the TSA output from C to D is actually negative rather than zero. This implies that the thermal insulating layer (a thick layer of ceramic cement for the data in Fig. 34) is not completely blocking out the thermoelastic effect. Instead, it decreases the temperature amplitude significantly and causes a phase shift in the sinusoidal temperature variation coming from the specimen. In this particular case, the fact that the TSA data are negative implies a phase lag of between 90° and 270°.

Using the technique described in the previous paragraph, the focus curve provided by the manufacturer of the SPATE system was verified. This focus curve applies to 8- to 12- $\mu\text{m}$  radiation. A new focus curve for the 2- to 3- $\mu\text{m}$  range was also constructed. These two curves are shown in Fig. 35. Note that significant differences exist in the

focus settings for these two different bands of wavelengths. Thus, it is extremely important to use the proper focus curve for the optical filter at hand when performing high-temperature TSA scans with the SPATE system. At room temperature, insignificant amounts of radiation are emitted by a blackbody at the shorter wavelengths where atmospheric windows exist, and chromatic aberration is not a problem (see Chapter 2 and Figs. 1 and 2).

## **7.2 Photodetector Saturation**

If excessive radiation reaches the photodetector, it becomes saturated (i.e., the photodetector does not return to a neutral electrical state upon removal of the incident radiation). Attenuating filters should be placed between the specimen and the infrared camera if this problem is to be avoided. Such filters are commercially available. Some brands of commercial plastics used for transparency overheads have been found to be a cheap alternative to expensive commercial infrared filters. An example of the FFT of the photodetector output for the case in which the photodetector was bordering on complete saturation is given in Fig. 38, where it is seen that substantial noise exists at low frequencies. When a 60% transmittance filter was placed between the infrared camera and the specimen, this low-frequency noise is reduced by a factor of approximately 5, while the thermoelastic signal from the specimen was only reduced by 40 percent (see Fig. 38).

## **7.4 Temperature Gradient Effects**

Large temperature gradients affect the TSA data in two ways. First of all, for full-field scanning, variations in temperature over the scan region affect the magnitude

of the thermoelastic output (since this output is proportional to the cube of the absolute temperature - see Eq. 5.2). Also, these gradients keep the test furnace from stabilizing at a uniform temperature during testing. An example of high-temperature data before and after furnace stabilization is given in Fig. 36. The specimen geometry for these scans is shown in Fig. 37. Secondly, any specimen motion perpendicular to the direction of viewing will result in a false TSA signal if temperature gradients are also present in this direction. Success has been achieved in correcting for the first effect by using absolute temperature imaging.

### 7.5 Emissivity Effects

These effects are caused by specimen motion. If the specimen emissivity varies from point to point on the specimen surface, any specimen motion will result in a net change in the average emissivity within the region the photodetector is focused on. This effect can be quite dramatic. For example, in order to obtain a stress resolution of 1 MPa in 304 stainless steel at room temperature, the average emissivity must not vary by more than 0.0014 percent. This can be seen from Eq. 5.2:

$$\Delta e = \frac{3e\alpha}{\rho C_p} \Delta\sigma = \frac{3(1)(17.3 \times 10^{-6} \text{ m/m/K})}{(7920 \text{ kg/m}^3)(477 \text{ J/kg}\cdot\text{K})} (10^6 \text{ Pa}) = 0.000014$$

where the average emissivity has been assumed to be equal to unity. In particular, nonuniform specimen oxidation at high temperatures can cause serious spatial emissivity variations. Consequently, it is usually necessary to cover the specimen with an oxidation-resistant coating. A ceramic cement composed primarily of silicon carbide

and silica is the best coating that has been found to date. It gives excellent results at room temperature (often better than using ultra-flat black paints), and has been successfully used at temperatures exceeding 1000 °C.

An example of poor high-temperature TSA data due to variations in spatial emissivity is shown in Fig. 39 for the case of a graphite-based high-temperature spray paint. Note the dramatic increase in scatter in the data at 130 °C as compared to 25 °C. This was typical of graphite-based high-temperature spray paints in this temperature range. The 130 °C TSA scan was repeated over time and for a large range of specimen cycling frequencies, and the same pattern was always observed. This effectively rules out the possibility that the scatter is due to turbulence or heat conduction effects. The use of an 8- to 12- $\mu\text{m}$  optical filter rules out the possibility of chromatic aberration, leaving emissivity effects as the only possible cause for scatter. This conclusion is further verified by the fact that much better results were obtained with the same specimen and equipment arrangement, but using the silicon carbide ceramic coating instead of the high-temperature spray paint.

## 7.6 Edge Effects

Emissivity and temperature gradient effects are of particular concern at specimen edges, where the photodetector is focused partly on the specimen and partly on the background. The background (which may be heating coils, insulation, etc.) is normally at a significantly different temperature and emissivity than the specimen. In such cases the thermoelastic component of the TSA signal can be over an order of magnitude smaller than the component of the TSA signal due to emissivity and temperature gradient effects. The best solution is to provide a stress-free backing for

the specimen having the same emissivity and being at the same temperature as the specimen. At room temperature this is easily accomplished by coating a piece of paper with the same coating as is used for the specimen, and then loosely attaching the paper to the back of the specimen. Obtaining a proper background is much more difficult at high temperatures, however, and no simple solutions have yet been found.

When the six major problems just discussed are minimized, it is possible to obtain high-temperature TSA data having stress resolutions comparable to those obtainable at room temperature.

### 7.7 Experimental Results

In order to verify the temperature independence of the minimum resolvable stress, tests were conducted on a uniform 304 stainless steel specimen at a variety of temperatures. The specimen was coated with the silicon carbide ceramic cement mentioned in Section 7.1. Below 400 °C, an 8- to 12- $\mu\text{m}$  filter was placed between the furnace and the infrared camera in order to keep shorter wavelength radiation from reaching the photodetector. Above 400 °C, a 1-mm thick glass plate was used. Above 500°C, attenuating filters were used in addition to the glass filter in order to limit the intensity of radiation reaching the photodetector. The particular filters used transmit about 60% of the radiation in the 2- to 3- $\mu\text{m}$  range. The furnace was allowed to stabilize for several hours at each new temperature before TSA frame scans were obtained. The frame scans (approximately 10-mm wide by 6-mm high) were taken through the center of the furnace window.

Experimental verification of the independence of resolvable stress with temperature is given in Fig. 40. These data were obtained by taking the standard deviation of the

TSA frame scans. The resolvable stress is seen to degrade at first as the temperature increases (roughly a factor of two loss in stress resolution between 25 °C and 400 °C). This is believed to be due to excessive radiant photon flux reaching the photodetector. At higher temperatures, where the 2- to 3- $\mu\text{m}$  glass-germanium filtering is employed, the minimum resolvable stress returns to its room-temperature value. At approximately 400 °C, the minimum resolvable stress using the 2- to 3- $\mu\text{m}$  filter improves rapidly with increasing temperature. The explanation for this phenomenon is as follows. Below 400 °C, little radiation is emitted by the specimen between 2 and 3  $\mu\text{m}$  wavelengths (see Fig. 1), and electrical noise in the photodetector electronics is the primary factor limiting the resolvable stress amplitude. Above 400 °C, the radiant photon emittance between 2 and 3  $\mu\text{m}$  increases rapidly, thermal noise rather than electrical noise becomes the limiting factor, and the minimum resolvable stress amplitude returns to its room-temperature value (in accordance with Eq. 5.3).

As further demonstration of the capabilities of high-temperature TSA, line scans were obtained with a Hastelloy-X specimen at a temperature of 1040 °C. The specimen geometry is given in Fig. 37. The specimen had been coated with silicon carbide ceramic cement prior to testing. A FFT analysis of the TSA output was performed in the flat region of the specimen (region C of Fig. 37). As shown in Fig. 43, the signal-to-noise ratio is quite good. In fact, the minimum resolvable stress amplitude of 0.6 MPa at 1040 °C is the same as the minimum resolvable stress amplitude for this alloy at room-temperature. Line scans were also performed at four uniformly spaced load amplitudes, Fig. 44. The data have the proper qualitative appearance (i.e., uniform spacing in the TSA output for uniform increments in load amplitude). These line scans also have the same basic shape as line scans performed at room temperature,

although there are some significant differences that remain unexplained at this time (see Fig. 43). Still, these results at least demonstrate the feasibility of applying TSA at temperatures exceeding 1000 °C. Better results can be expected in the future as further refinements and improvements in the testing techniques are made.

### 7.8 New Specimen Geometry

Up to this point in our research the majority of the high temperature testing was done with flat-plate specimens. The question then arose whether or not we could be successful scanning specimens with stress concentrations at elevated temperatures. Since the previous method of taking standard deviations to compare stress resolutions would not be valid with a stress concentration present, we would have to rely on the actual frame scans themselves in order to compare room temperature scans to high temperature scans. The material used for these tests was 304 stainless steel with a 1/4" diameter hole in the center of the scan area. These specimens were also covered with a silicon carbide ceramic coating. A backing plate of the same material and surface coating was used to avoid any possible edge effect problems (see Edge Effects, Sec. 7.6). Scans were taken at room temperature, 100°C, 300°C, and 800°C (Figures 44a, 44b, 44c, and 44d) using the same filtering techniques that were used for the flat-plate testing. The scans show a strong similarity to each other over the large temperature range, indicating that the stress resolution remained independent of temperature.

The capabilities of TSA at high-temperature seem to have no upper temperature limit. The furnace used for our research only allowed us to test up to 1100°C, but all of our data shows that going above this temperature will only lead to equal or better stress resolution than at room temperature. High-temperature stress analysis represents one

of the most promising new frontiers for TSA and should be carefully explored in order to discover its full potential.

## 8. A THERMOELASTICITY THEORY FOR DAMAGE IN ANISOTROPIC MATERIALS

(Dr. Daqing Zhang)

Composite materials such as fiber-reinforced materials, carbon-carbon composites, and ceramic and metal-matrix composites are needed for structures intended for high temperature conditions and hostile environments. The characteristics of the microstructure and the associated micromechanisms in these materials are changed due to the micro-damage accumulation under load-environment interaction with time. For instance, microcracks occur in the fiber/matrix interface bonding of composites and these cracks are randomly distributed. Damage mechanics is required to establish criteria for damage evaluation in composites, since theories of continuum mechanics, plasticity and fracture mechanics may not be suitable for the failure description of the materials.

In order to exploit new techniques for evaluation of damage accumulation, a theory of thermoelasticity for damage in anisotropic materials was developed [47] by employing fundamentals of damage mechanics. The generalized temperature change due to small linear elastic deformation in anisotropic damage can be expressed as

$$\Delta T = \frac{T}{\rho^e C_\epsilon} \left( \frac{\partial M_{ij}}{\partial T} C_{jk} \epsilon_k + M_{ij} \frac{\partial C_{jk}}{\partial T} \epsilon_k - M_{ij} C_{jk} \alpha_k \right) \Delta \epsilon_i \quad (8.1)$$

where  $M_{ij}$  is the effective damage tensor,  $C_{jk}$  is the stiffness matrix,  $\alpha_k$  are the

thermal expansion coefficients and  $\rho^e$  is the effective mass density of the material.

Simplify the above equation by neglecting the temperature-dependent terms, and consider a state of plane stress with damage in the material,

$$\Delta T = - \frac{T}{\rho^e C_p} \left( \alpha_1 M_{11} \Delta \sigma_1 + \alpha_2 M_{22} \Delta \sigma_2 \right) \quad (8.2)$$

Effective mass density  $\rho^e$  can be related to a damage parameter  $D$  and undamaged mass density  $\rho$ ,

$$\frac{1}{\rho^e} = \frac{1}{\rho} \left( \frac{1}{1-D} \right) \quad (8.3)$$

The damage parameter  $D$  can also be expressed as the change of Young's modulus

$$D = \frac{E - E^e}{E} \quad (8.4)$$

where  $E^e$  is the Young's modulus of the damaged material.

This theory is particularly useful in investigating the microstructure-mechanics connection of multiphase materials, and in establishing quantitative prediction capabilities of macroscopic behaviors and service lives. The damage parameter  $D$ , the normalized effective mass density  $\rho^e/\rho$ , and the effective modulus  $E^e$  in composites can be quantitatively evaluated by incorporating the method of thermographic stress analysis (TSA method). Specifically, the determination of normalized effective mass density  $\rho^e/\rho$  from this theory is important for applying the TSA method to damaged materials, since there are no other experimental techniques available to evaluate this quantity easily.

The detailed derivation of the theory is given in Ref. 47. The measurements of damage parameters in glass fiber/epoxy composites by the TSA method[47] have shown excellent agreements with the measurements by a conventional extensometer. A few examples are shown in Figs. 45 - 47. Most importantly, this theory can also be used to determine the damage parameters for composites at high temperature condition under dynamic loads by the TSA method.

The advantages of the TSA technique in applying this theory for composites at elevated temperatures are as follows:

1. Microcrack developments (randomly distributed) due to load-environment interaction in the material can be monitored from full-field stress maps which cover global effects that damage mechanics would deal with, but not local effects that the theories of continuum mechanics, plasticity and fracture mechanics address.
2. Non-contacting measurement is particularly important in the damage evaluation of composites at high temperature condition because there is no need to go through the series of operations recommended for the correct and difficult installation and use of measuring sensors.
3. The damage parameter  $D$  and the normalized mass density  $\rho^e/\rho$  can be directly, nondestructively, and quantitatively obtained from the TSA signals.

## 9. SEPARATION OF THERMOELASTICALLY INDUCED ISOPACHICS INTO INDIVIDUAL STRESSES

( Professor R.E. Rowlands & Dr. Y.M. Huang )

Practical design and analysis of a structural or machine component necessitates quantitative information on the individual stresses  $\sigma_x$ ,  $\sigma_y$  and  $\tau_{xy}$ . Determination of boundary stresses requires reliable boundary data. However, conventional thermoelasticity provides information on only the sum of the principal stresses ( isopachics ), measured thermoelastic data can be quite noisy, and recorded edge information is usually unreliable [48]. These features have tended to cause differential thermography ( thermoelasticity ) to be highly qualitative in certain cases. A new concept was recently proposed [49,51] for simultaneously smoothing the isopachic data, enhancing measured boundary information and separating the internal stresses. Unlike other hybrid techniques such as that of Ref. [48], this new method does not require any prior smoothing of measured data. Stress equilibrium and strain compatibility prevail within the region analyzed and the traction-free edge conditions are satisfied. Effective means of separating the stresses are essential for thermoelasticity to become a more generally useful, quantitative method of stress analysis.

These capabilities are described in Refs. 48 - 53. A representative example involving the determination of the individual stresses in a region R adjacent to a hole in an aluminum tensile strip is presented in Figs. 48 - 51. Figure 49 shows the

thermoelastically generated isopachics ( $\sigma_x + \sigma_y$ ) throughout a region R adjacent to the top boundary of the hole in Fig. 48. The hole radius is 0.34" and the region R of Figs. 49 - 51 covers  $0.34" \leq r \leq 0.68$  and  $-30^\circ \leq \phi \leq 60^\circ$ . Contours of the largest stress  $\sigma_x / \sigma_y$  throughout region R as determined from the thermoelastic data of Fig. 49 are shown in Fig. 50. Stresses of Fig. 50 were obtained using less than 5% of the available measured data. The thermoelastically measured stresses of Fig. 50 are compared with theory in Fig. 51. The agreement is excellent. Additional results are contained in Refs. 48 - 50.

This stress - separation research, in addition to receiving some support from this Air Force grant, has been supported extensively by NSF ( grant MSM - 8706662 ) and the UW Alumni Association.

## 10. SUMMARY AND CONCLUSIONS

The theory for thermographic stress analysis has been expanded to include nonlinear thermoelastic, thermoplastic, and specimen motion effects. An enhanced TSA equation was developed, and new significant findings derived from this equation were discussed. In particular, the developments in this report pave the way for several new applications for thermographic stress analysis including residual stress analysis, cyclic plasticity analysis, and high-temperature stress analysis.

Residual stresses were quantitatively measured in a C-specimen composed of Ti-6Al-4V alloy. The minimum resolvable residual stress was approximately 25 MPa. A limitation of the residual stress measurement technique developed in this report is that the specimen must be initially free of residual stresses. The residual stresses are then induced by overloading the specimen until plastic flow occurs in the critical regions.

Uniform cylindrical specimens of 1020 steel and 6061-T6 aluminum were cyclically loaded into the elastic-plastic regime, with TSA, stress, and strain data being recorded. For 1020 steel it was found that the TSA output at twice the cycling frequency was proportional to the plastic-work energy per cycle. For 6061-T6 aluminum, the data were complicated by the presence of sizeable nonlinear thermoelastic effects at twice the specimen cycling frequency. The TSA output at the specimen cycling frequency was found to be a complex function of the stress amplitude, plastic-work energy per cycle, specimen temperature, and filtering characteristics of the particular TSA equipment used.

Problems with applying thermographic stress analysis at elevated temperatures were described, and some possible solutions were presented. The principal problems

encountered at high temperatures are chromatic aberration, turbulence, photodetector saturation, emissivity effects, temperature gradient effects, and edge effects. When these problems were minimized, the minimum resolvable stress amplitude was found to be approximately independent of the specimen temperature for temperatures between 25 and 850 °C. This finding is in agreement with the theory developed in this report.

High-quality TSA line scans were obtained for a cracked plate of 304 stainless steel at 550 °C. TSA line scans of moderate quality were also obtained for a Hastelloy-X specimen at 1040 °C. These data demonstrate the feasibility of using thermographic stress analysis to monitor stresses in complex members at elevated temperatures. Further advances in this area can be expected as hardware, software and research methodologies are further developed.

## APPENDIX A

### A.1 Infrared Radiation

A blackbody is an object that absorbs all the radiation incident upon it. In addition, a blackbody is a perfect emitter. Such an object is said to have a surface emissivity of unity, independent of temperature or the wavelength of light. Planck's law relates the spectral radiant emittance of a blackbody,  $W_\lambda$  (watts/[m<sup>2</sup>•μm•steradian]), to the wavelength and temperature [25]:

$$W_\lambda = \frac{2hc^2}{\lambda^5} \left( \frac{1}{\exp(hc/\lambda kT) - 1} \right) \quad (\text{A.1})$$

The voltage output of an ideal photon detector is proportional to the rate of incident photons rather than the incident power. It is thus more useful to consider the spectral radiant photon emittance,  $\phi_\lambda$  (photons/[m<sup>2</sup>•μm•steradian•s]), obtained by dividing  $W_\lambda$  by the energy per photon ( $hc/\lambda$ ):

$$\phi_\lambda = \frac{2c}{\lambda^4} \left( \frac{1}{\exp\left(\frac{hc}{\lambda kT}\right) - 1} \right) \quad (\text{A.2})$$

This equation is plotted in Fig. 1 for several temperatures. At room temperature, the peak value for  $\phi_\lambda$  occurs at approximately 12 μm. At higher temperatures, the peak shifts to shorter wavelengths. Integrating Eq. A.2 between wavelengths  $\lambda_1$  and  $\lambda_2$  results in

$$\phi = \int_{\lambda_1}^{\lambda_2} \phi_{\lambda} d\lambda = B T^3 \quad (\text{A.3})$$

where  $\phi$  is the total radiant photon emittance between wavelengths  $\lambda_1$  and  $\lambda_2$ , and  $B$  is a constant (for the particular  $\lambda_1$  and  $\lambda_2$  at hand). Few real materials approximate a blackbody; instead, the surface emissivity depends on both temperature and wavelength. For simplicity, it is hereafter assumed that emissivity is independent of wavelength between wavelengths  $\lambda_1$  and  $\lambda_2$ . Equation A.3 can then be written as

$$\phi = e B T^3 \quad (\text{A.4})$$

where  $e$  is understood to depend on  $T$ . If emissivity does vary greatly with wavelength between  $\lambda_1$  and  $\lambda_2$ , it must be included in the integrand of Eq. A.3. In thermographic stress analysis, the component to be analyzed is usually coated with a substance that provides a high, spatially uniform emissivity. As discussed in Chapters 5 and 7, spatial uniformity of emissivity is critical when small temperature changes are to be measured. Commercial flat-black spray paints were used for the room-temperature analyses presented in this report. For elevated temperatures, high temperature flat-black paints and a silicon carbide ceramic coating were employed (see Chapter 7 for details).

In typical applications of thermographic stress analysis, the radiation emanating from the component under investigation must be transmitted through the atmosphere, which tends to absorb, scatter and refract the radiation. The atmospheric transmittance

versus wavelength is shown in Fig. 2. Notice that a good atmospheric window exists between wavelengths of 8 and 14  $\mu\text{m}$ . Coincidentally, these are the wavelengths of peak emittance at room temperature. Provided the photon flux reaching the detector is limited to this 8 to 14  $\mu\text{m}$  window, the effects of the ambient atmosphere on the TSA signal are ordinarily insignificant, at least for laboratory conditions. If the photon flux is not limited to a good atmospheric window, or if the specimen-to-camera path contains a gas environment other than "normal" air, then the effects of the local atmosphere must be accounted for.

## APPENDIX B

### B.1 Infrared Photon Detectors

A variety of photodetectors have been developed for use over a wide range of wavelengths. Details on the various types of photodetectors (photoconductive and photovoltaic photon detectors, thermal detectors, photoemissive detectors, etc.) can be found in Ref. 27. The SPATE 8000 system used in this research employs a mercury-doped cadmium-telluride ( $\text{Hg}_{1-x}\text{Cd}_x\text{Te}$ ) photovoltaic photon detector (also commonly called a photodiode) [28]. By varying  $x$ , different band-gap energies are obtained. If  $x = 0.2$  (which is the approximate composition for the detector in the SPATE system), a band-gap energy of 0.1 eV is obtained [27], which corresponds to a photon wavelength of 12.4  $\mu\text{m}$ . Photons with energies greater than the semiconductor band-gap energy will excite electrons from the nonconducting state into the conducting state. This in turn changes the open circuit voltage of the photodiode. Photodiodes are normally operated under reverse bias, and so the observed signal is actually a photocurrent rather than a photovoltage. The SPATE system employs a servo-loop "feed-back" preamplification stage which converts the photodiode output current into a voltage while maintaining the photodiode at the optimum zero-voltage bias [28]. This preamplification stage has the effect of filtering out the static DC voltage from the photodetector. Thus, only dynamic changes in the incident photon flux rate to the photodetector are represented in the output voltage of the SPATE infrared camera. This fact is crucial for understanding the data obtained under elastic-plastic loading conditions (see Chapter 6 for details).

An ideal photon detector is equally responsive to all photons having energies

greater than the band-gap energy. Thus, a  $\text{Hg}_{0.8}\text{Cd}_{0.2}\text{Te}$  detector is sensitive to radiation at wavelengths shorter than  $12.4 \mu\text{m}$ . Since the atmosphere has several windows of transmission at shorter wavelengths ( $0.5\text{-}1.4$ ,  $1.5\text{-}1.8$ ,  $2.0\text{-}2.5$ ,  $3.4\text{-}4.2$  and  $4.5\text{-}5.0 \mu\text{m}$ ), it is possible to use such a detector within these atmospheric windows, as well as the  $8$  to  $14 \mu\text{m}$  window. At room temperature, very little radiation is emitted by a blackbody material at wavelengths shorter than  $5 \mu\text{m}$ , and the effects of this radiation can be safely ignored. At high temperatures, however, the total photon emission at these shorter wavelengths can be greater than the emission between  $8$  and  $14 \mu\text{m}$ , and the effects of this radiation must be considered.

Under normal operating conditions, the photodetector output voltage is linearly related to the total incident photon rate,  $\phi_i$ :

$$S = R \phi_i = e R B T^3 + R \phi_b \quad (\text{B.1})$$

where  $\phi_b$  is the incident photon rate for background radiation. Background radiation is any radiation that reaches the detector but originates from somewhere other than the target. For photodiodes the detector responsivity,  $R$ , is independent of the intensity of the incident radiation, except at very high incident power levels. It does depend, however, on the magnitude of the reverse bias saturation current [27]:

$$R \text{ (volts/photon/s)} = \frac{\eta \beta k T}{I_s} \quad (\text{B.2})$$

where  $\eta$  is the quantum efficiency of the photodiode semiconductor material (i.e., the

number of electron-hole pairs generated per photon),  $\beta$  is a constant of the order of unity, and  $I_S$  is the reverse bias saturation current. Ordinarily, the responsivity is plotted versus the incident power level, Fig. 3b, rather than being plotted versus the rate of incident photons, Fig. 3a. This leads to the common misconception that a  $\text{Hg}_{0.8}\text{Cd}_{0.2}\text{Te}$  detector is insensitive to short wavelength radiation. In fact, the detector has approximately the same quantum efficiency (i.e., volts out per unit rate of incident photons) for all radiation from the cutoff wavelength of  $12\ \mu\text{m}$  down to wavelengths shorter than visible light. This fact is essential in understanding high-temperature TSA phenomena. More details are given in Chapter 7.

The noise equivalent power (NEP) is the rms incident radiant power,  $P$ , required to produce an output voltage,  $V_S$ , equal to detector noise level,  $V_N$  [25]:

$$\text{NEP} = \frac{P}{V_S/V_N} = \frac{V_N}{R} \quad (\text{B.3})$$

A more common parameter used to describe photodetector noise characteristics is the specific detectivity,  $D^*$  ( $\text{cm}\cdot\text{Hz}^{1/2}\cdot\text{W}^{-1}$ ), which is the signal-to-noise ratio when one watt of power is incident on a detector having an effective area of  $1\ \text{cm}^2$ , and the noise is measured over a 1 Hz bandwidth [25]. Thus,

$$D^* = \frac{(A \Delta f)^{1/2}}{\text{NEP}} \quad (\text{B.4})$$

where  $A$  is the area of the sensitive portion of the detector, and  $\Delta f$  is the frequency bandwidth over which the measurement is made. The minimum resolvable TSA signal

will generally be proportional to  $D^*$ . Typically, the specific detectivity decreases rapidly at low frequencies due to the presence of  $1/f$  power law noise. This noise is due to potential barriers at the contact, interior, or surface of the semiconductor [27]. For Hg:CdTe photoconductive detectors,  $1/f$  power law noise increases approximately as  $f^{-1/2}$  below a certain "corner frequency," typically 1 kHz [27]. Since many applications of TSA require measurements to be made at frequencies below 1 kHz, this  $1/f$  noise in photoconductive Hg:CdTe detectors is a serious limitation. Photovoltaic Hg:CdTe detectors are less prone to  $1/f$  noise, but they are prone to shot noise [27]. The shot noise current,  $I_N$ , is roughly proportional to the square root of the reverse bias saturation current [27]:

$$I_N = (2q I_S \Delta f)^{1/2} \quad (\text{B.5})$$

where  $q$  is the charge of an electron. Unlike  $1/f$  noise, shot noise is independent of frequency.

The reverse bias saturation current is almost independent of the reverse bias voltage over a large voltage range [29]. However, for large reverse bias voltages (which would be brought about due to large levels of incident photon flux),  $I_S$  increases rapidly. This in turn decreases the detector responsivity and increases the magnitude of the shot noise, as given by Eqs. B.2 and B.5. Thus, to avoid altering the responsivity and specific detectivity due to changes in  $I_S$ , care must be taken to attenuate incoming radiation when performing TSA scans at elevated temperatures. In fact, at very high incident power levels, the photodetector can be permanently damaged.

High-quality photon detectors are typically background limited. That is to say

that the minimum resolvable radiation level from the target is limited by extraneous background radiation that reaches the detector. If this background radiation could be completely eliminated and no electrical noise were present in the photodetector, the minimum resolvable signal would be limited by the probability of a photon emitted by the target arriving at the photodetector during the sampling period. This is known as the signal fluctuation limit, and is equal to  $4.4 \times 10^{-19}$  W for a photodetector cutoff wavelength of  $10 \mu\text{m}$  [27].

The background limit for a photon detector depends on a variety of parameters including the detector's operating temperature, the detector's spectral response, the spectral distribution of the background, and the field of view over which the detector receives background radiation. The best way to improve  $D^*$  is to cool the detector. Liquid nitrogen is normally employed for Hg:CdTe detectors. This minimizes background radiation from the detector itself. Also, since the detector is mounted to a substrate which is in turn mounted to a dewar containing the liquid nitrogen, very little background radiation is received by the backside of the detector. The only source of background radiation is then extraneous radiation arriving on the front side of the detector. If the frontside of the detector is unshielded, background radiation can arrive over an angle of view of  $180^\circ$  (i.e.,  $\pi$  steradians).

If the angle of view of the detector is decreased, the background radiation drops proportionally. This can be accomplished by placing a cryogenic "cold stop" aperture directly in front of the photon detector. This does not affect measurement of the target signal, which is normally focused through a lens and hence occupies a very narrow angle of view. The improvement in  $D^*$  that can be obtained by reducing the angle of view can be quite dramatic. In fact, for a photon detector having a cutoff wavelength of

approximately  $10\ \mu\text{m}$ , an order of magnitude improvement in  $D^*$  can be achieved by reducing the field of view from  $180^\circ$  to approximately  $15^\circ$  [27].

Table 1 Mechanical and Thermal Properties of Selected Materials at Room Temperature

Material	$\alpha$ ( $10^{-6}\text{m/m/K}$ )	$\rho$ ( $\text{kg/m}^3$ )	E (GPa)	$C_p$ (J/kg·K)	$\partial E/\partial T$ (MPa/K)
7075-T651 aluminum	23.6	2800	69	870	-----
6061-T6 aluminum	23.6	2700	69	933	-----
2024 aluminum	----	----	----	----	-36 (Ref. 42)
4150H steel	12.3	7840	200	477	-75 (Ref. 44)
Ti-6Al-4V	9.5	460	114	532	-48 (Ref. 45)
304 stainless steel	17.3	7920	190	477	-----
1020 steel	11.7	7860	200	467	-----

Except as noted, all data are from Refs. 45 and 46. For aluminum alloys in general,  $\partial E/\partial T$  is reported to be in the range of -35 to -45 MPa/K (Ref. 43)

Table 2 Effect of Prior Plastic Strain on the Thermoelastic Constant of Ti-6Al-4V

Prior plastic strain ( $\mu\text{m}/\text{m}$ )	Estimate for $\alpha/\rho C_p$ ( $10^{-6} \text{ m}^3\text{J}^{-1}$ )	% change
0	4.00	0.00
350	3.97	-0.75
930	3.98	-0.50
1580	3.98	-0.50
2780	4.02	+0.50
4260	4.02	+0.50
6570	4.01	+0.37

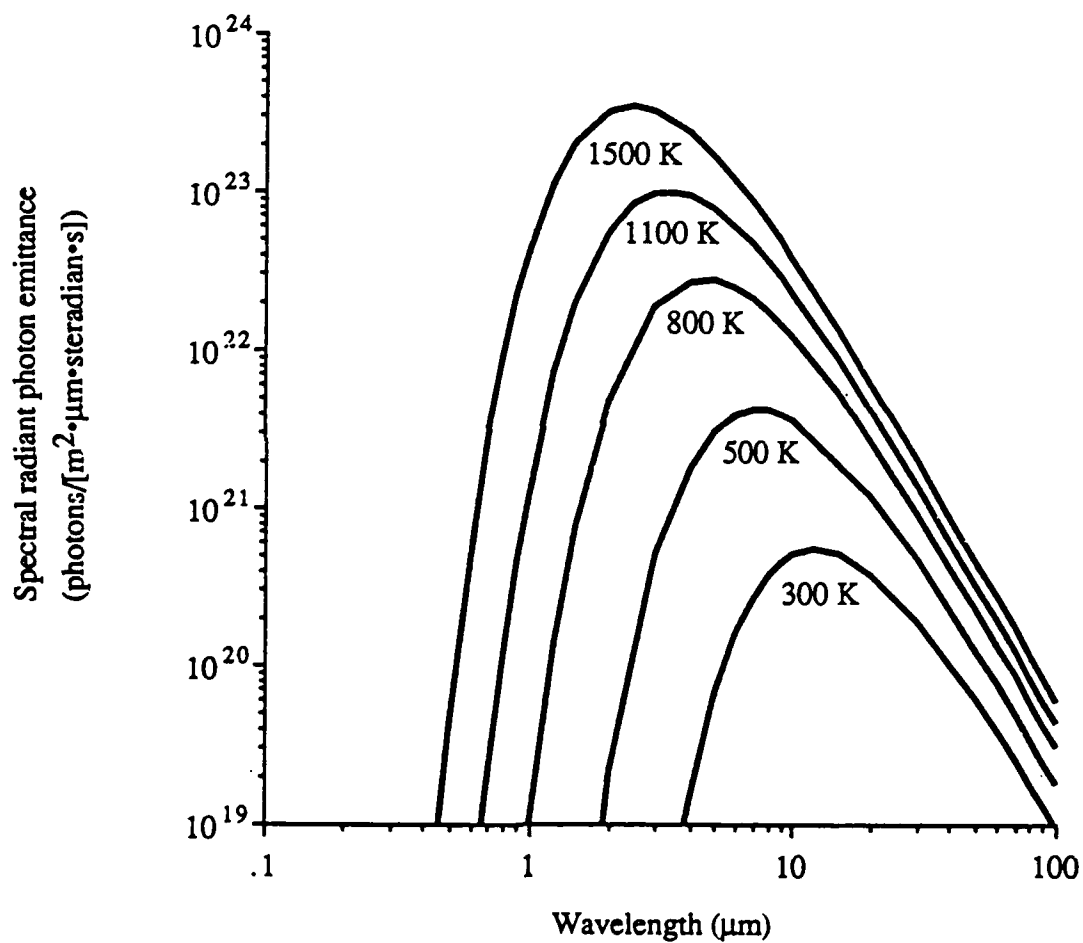


Figure 1 Spectral radiant photon emittance of a blackbody versus temperature and wavelength

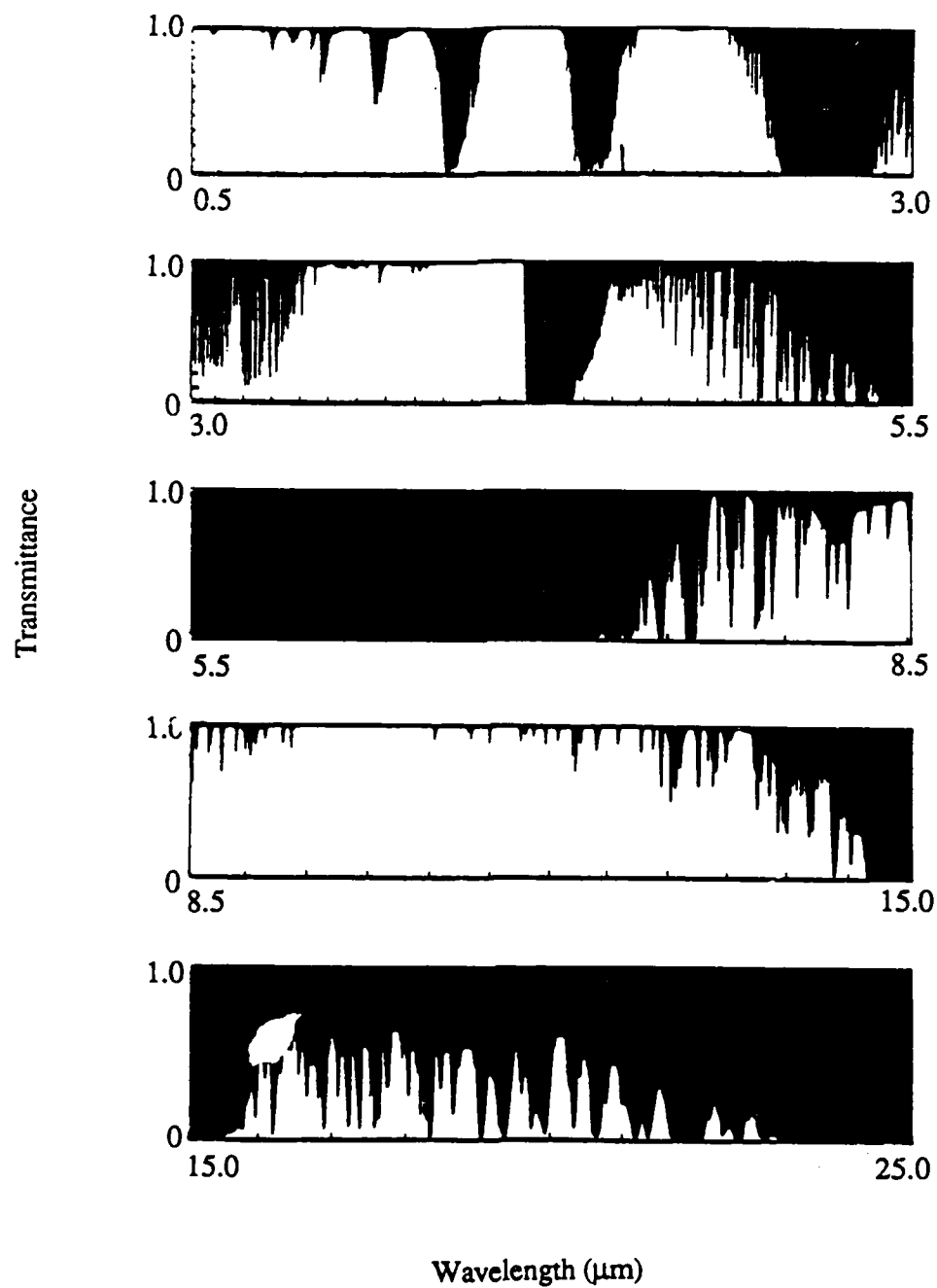
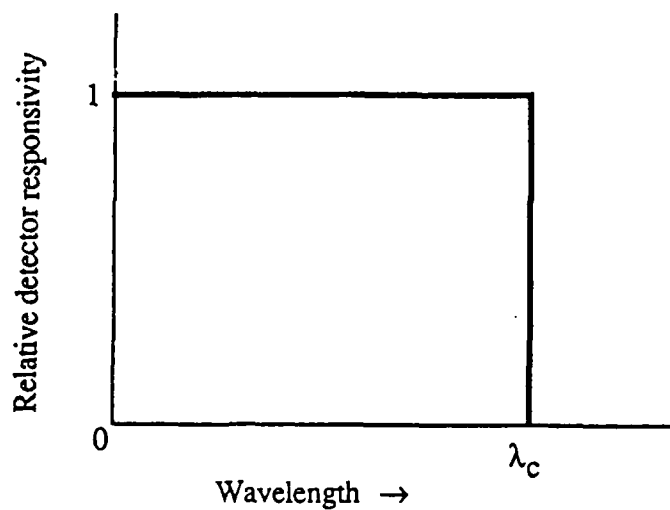
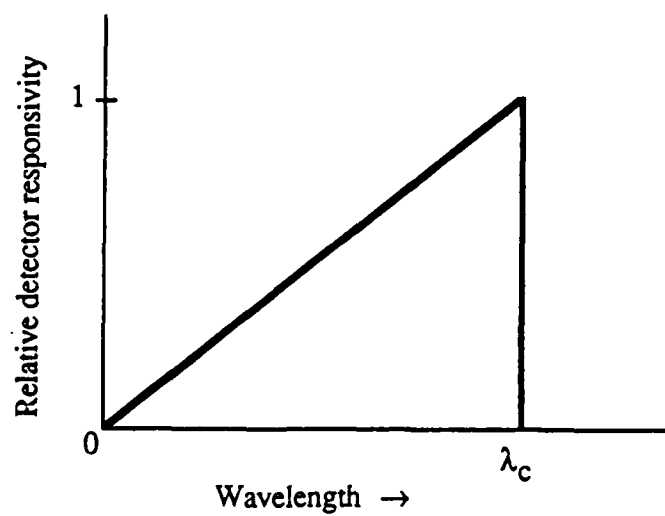


Figure 2 Infrared transmission of the atmosphere. Adapted from Ref. 26.



(a) Detector response for a constant incident photon flux rate at all wavelengths



(b) Detector response for a constant incident power flux at all wavelengths

Figure 3 Responsivity of an ideal photodetector

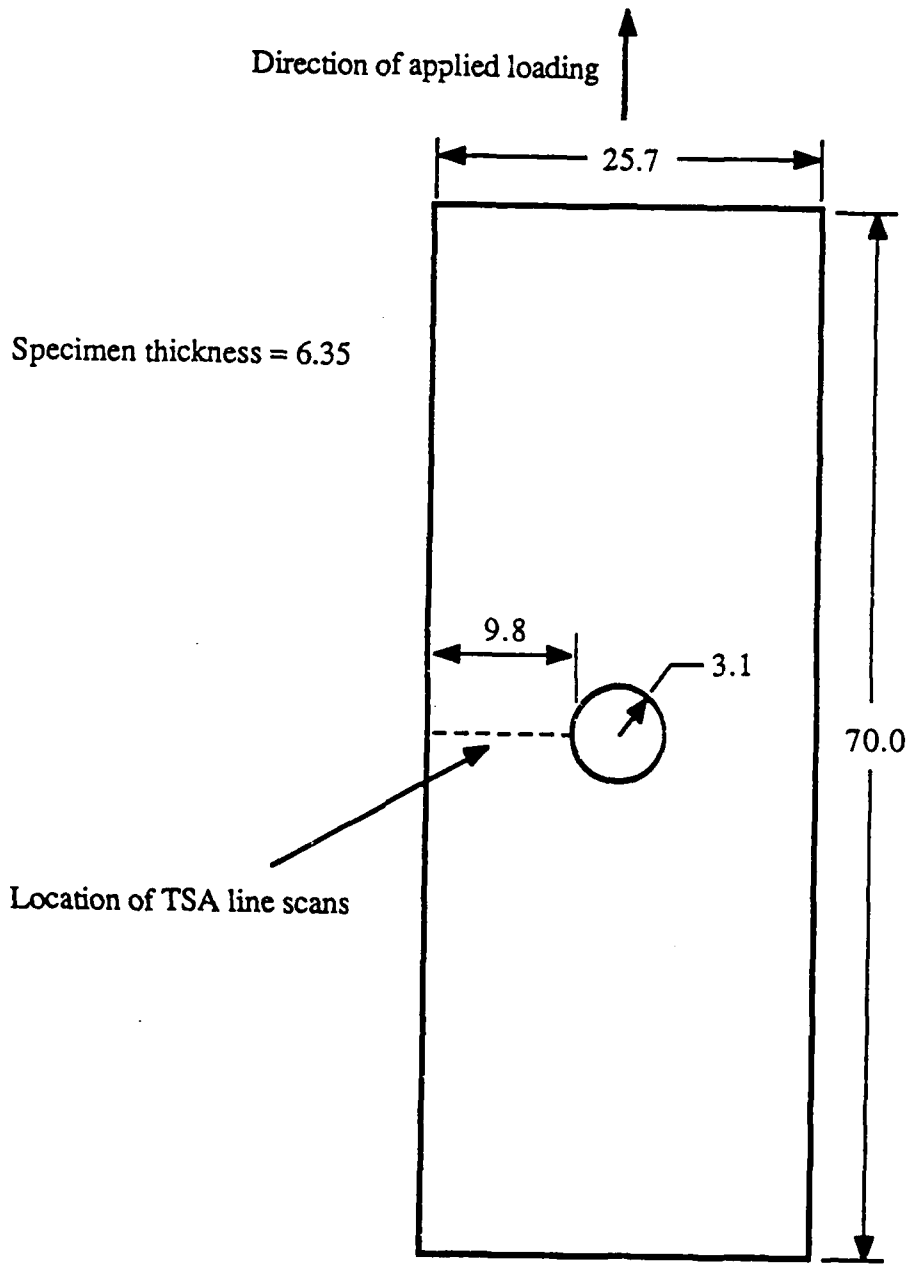


Figure 4 Location of TSA line scans for the 7075-T651 aluminum plate with a centrally located hole. All dimensions in mm.

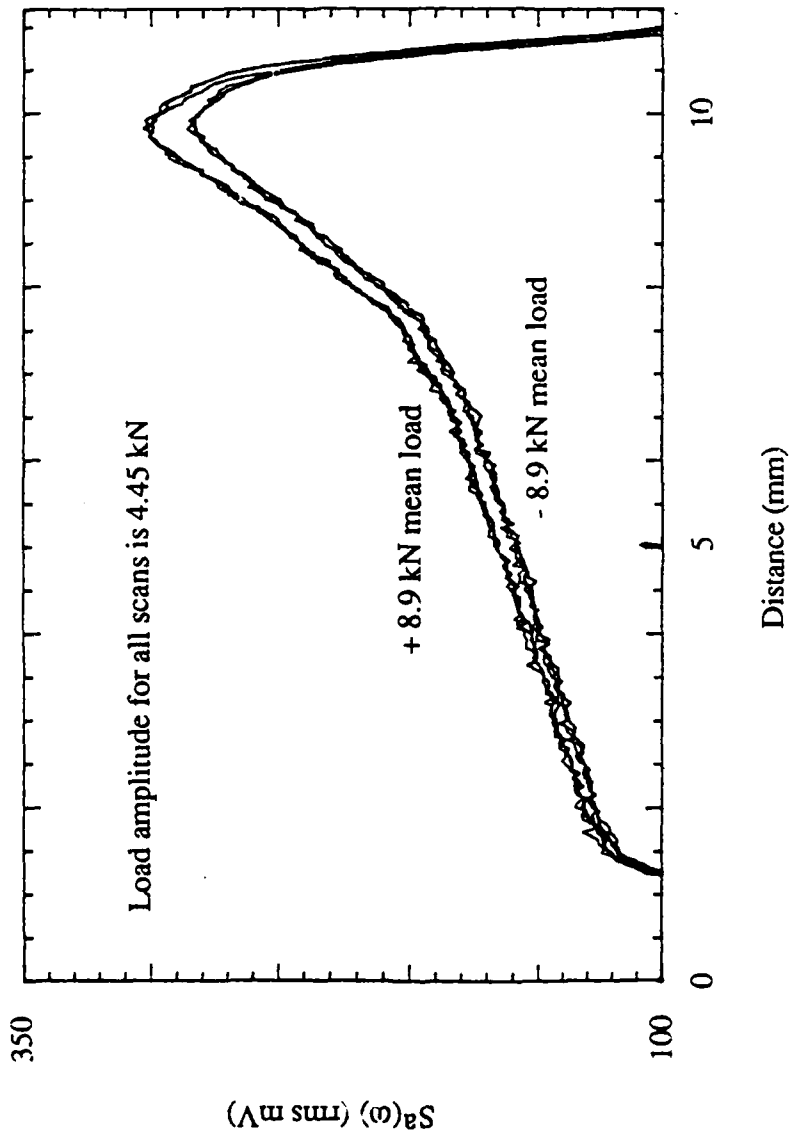


Figure 5 Raw TSA data for two different mean loads for the 7075-T651 aluminum specimen

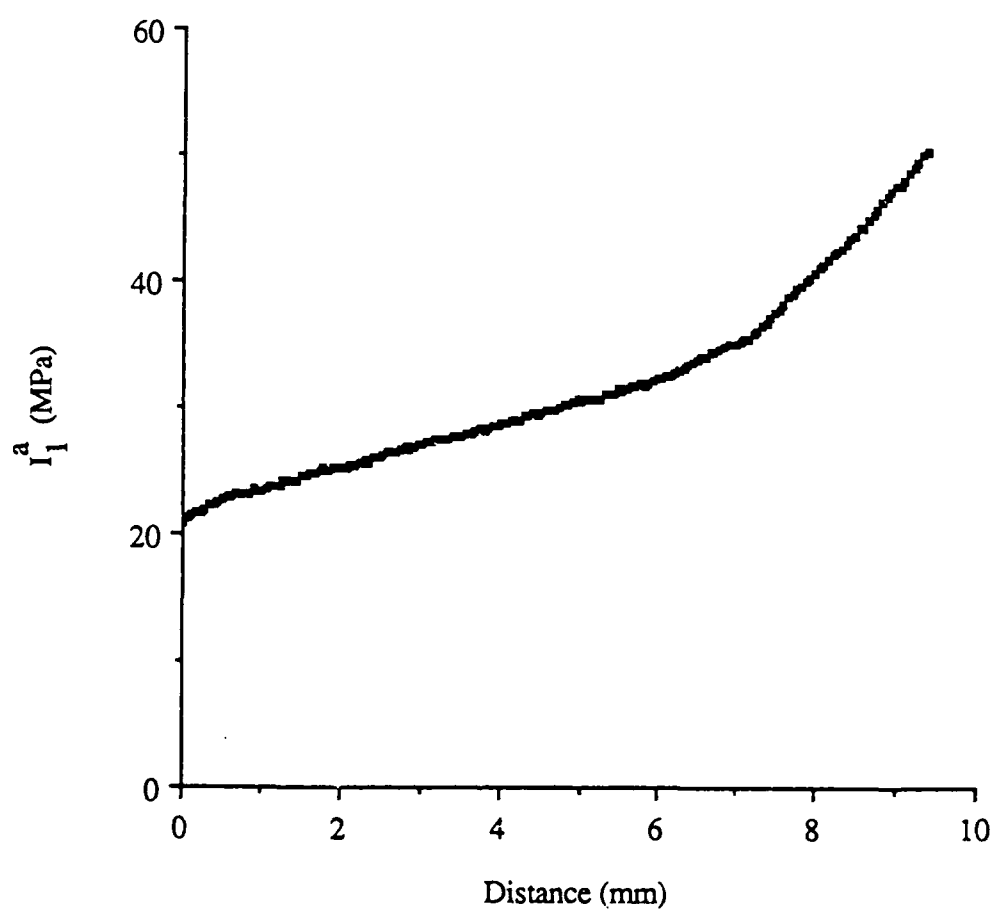


Figure 6 Amplitude of the first stress invariant determined from the TSA line scans of the 7075-T651 aluminum specimen

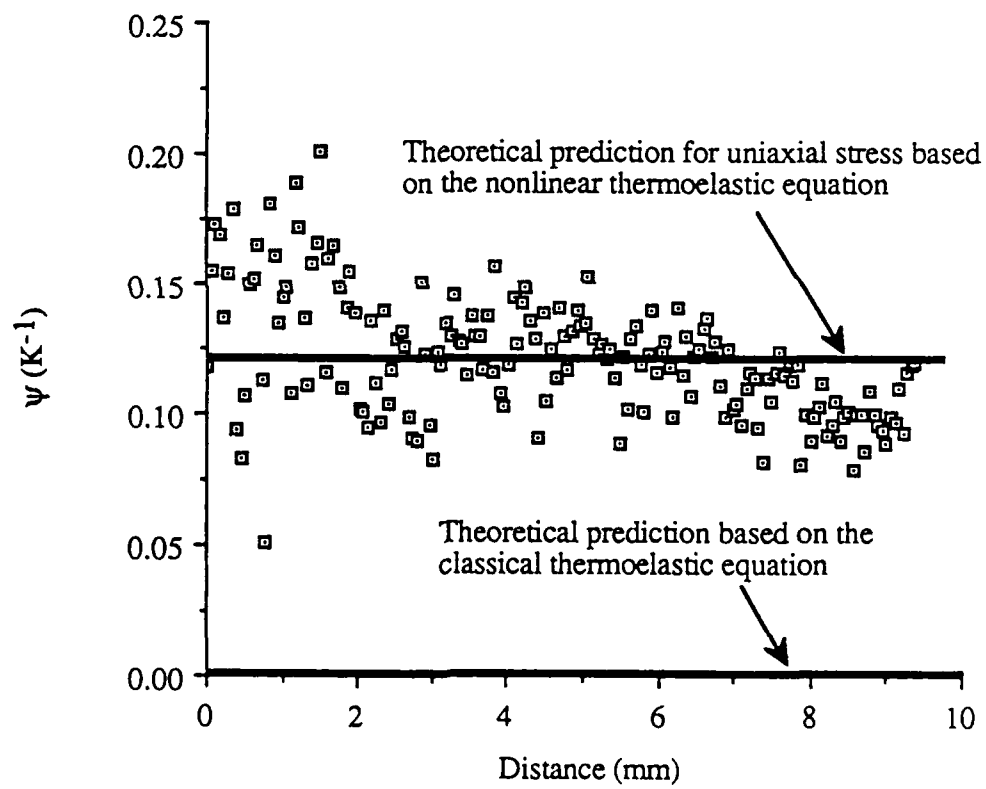


Figure 7  $\psi$  versus distance from left edge of specimen for the 7075-T651 aluminum specimen

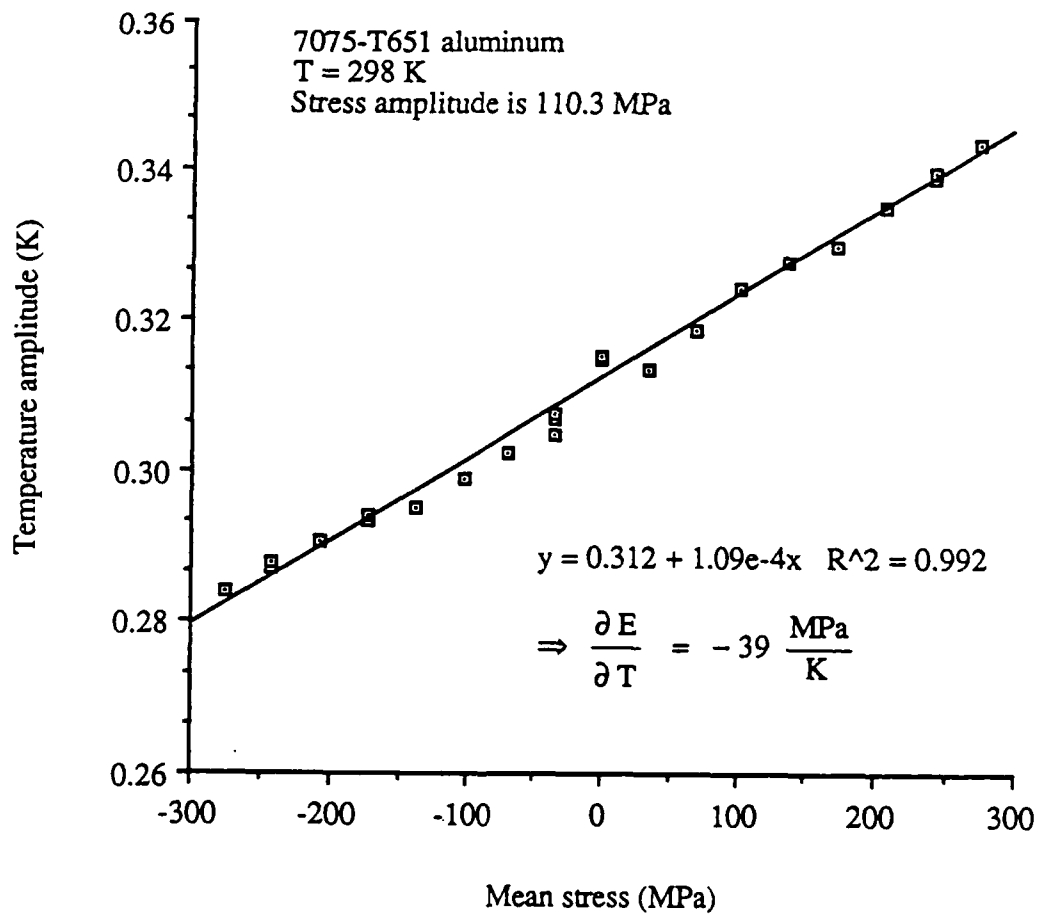


Figure 8 Mean stress effect in 7075-T651 aluminum

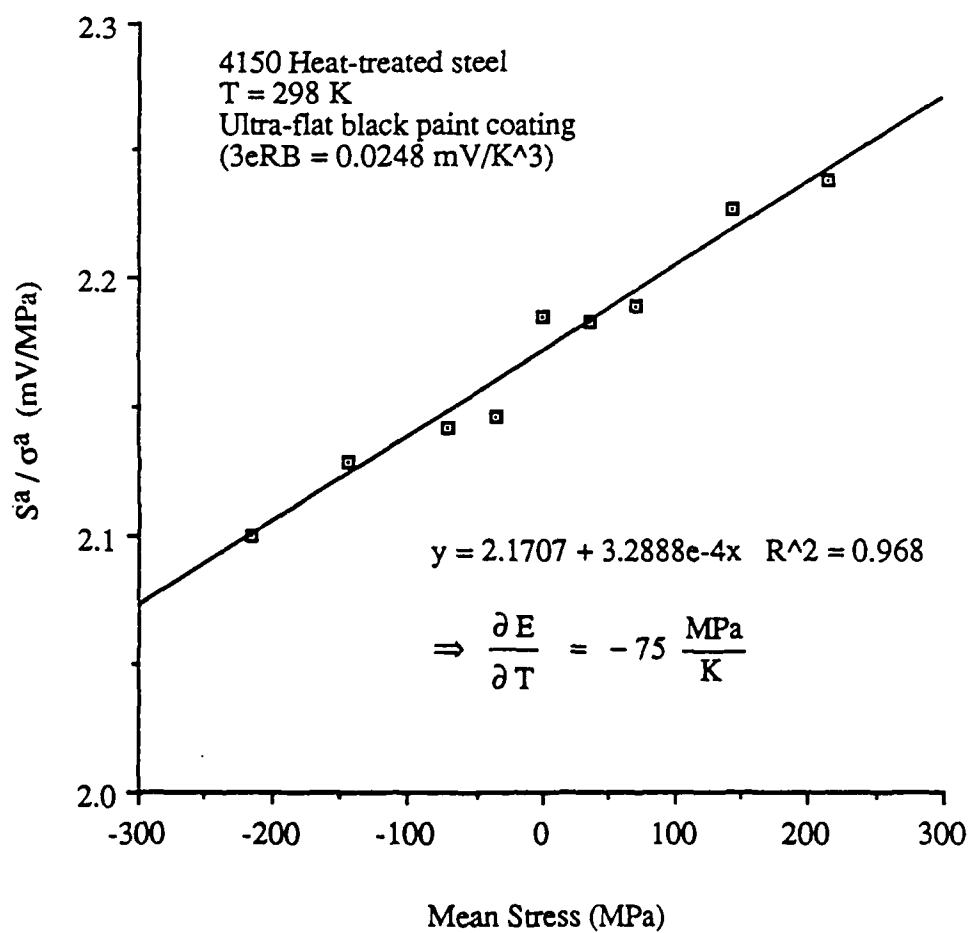


Figure 9 Mean stress effect in 4150 heat-treated steel

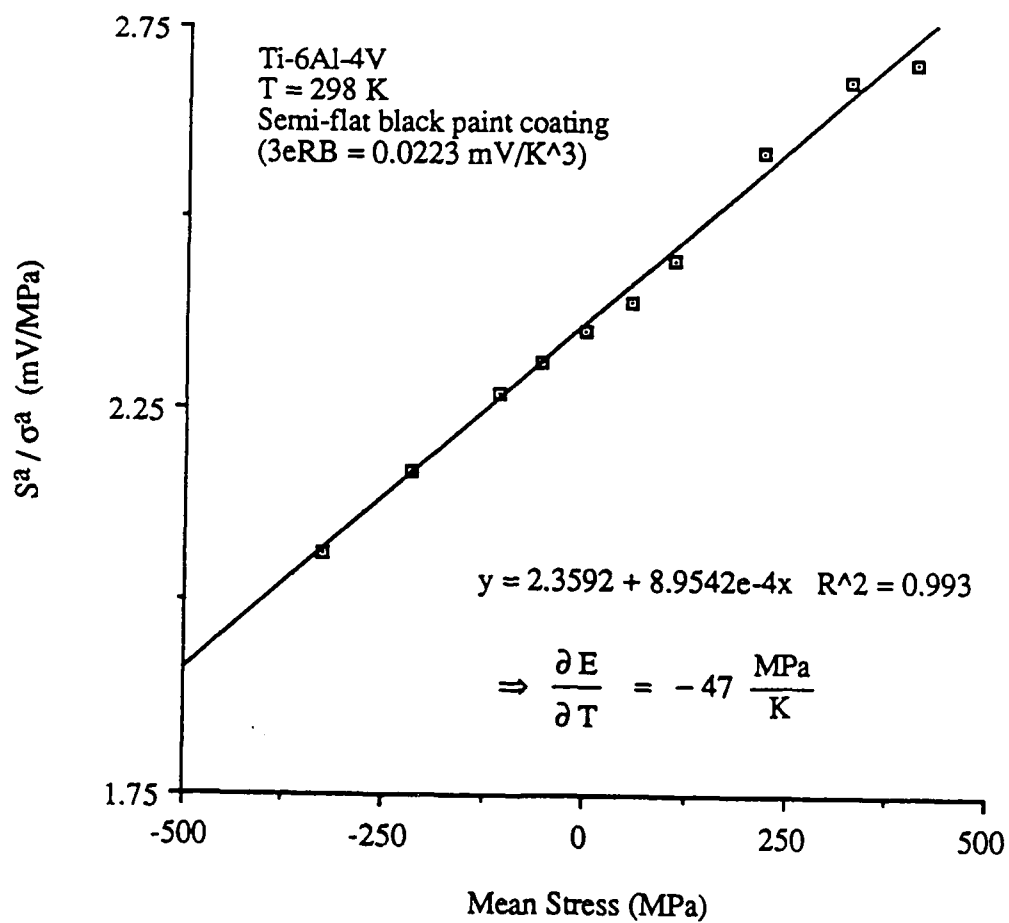


Figure 10 Mean stress effect in Ti-6Al-4V

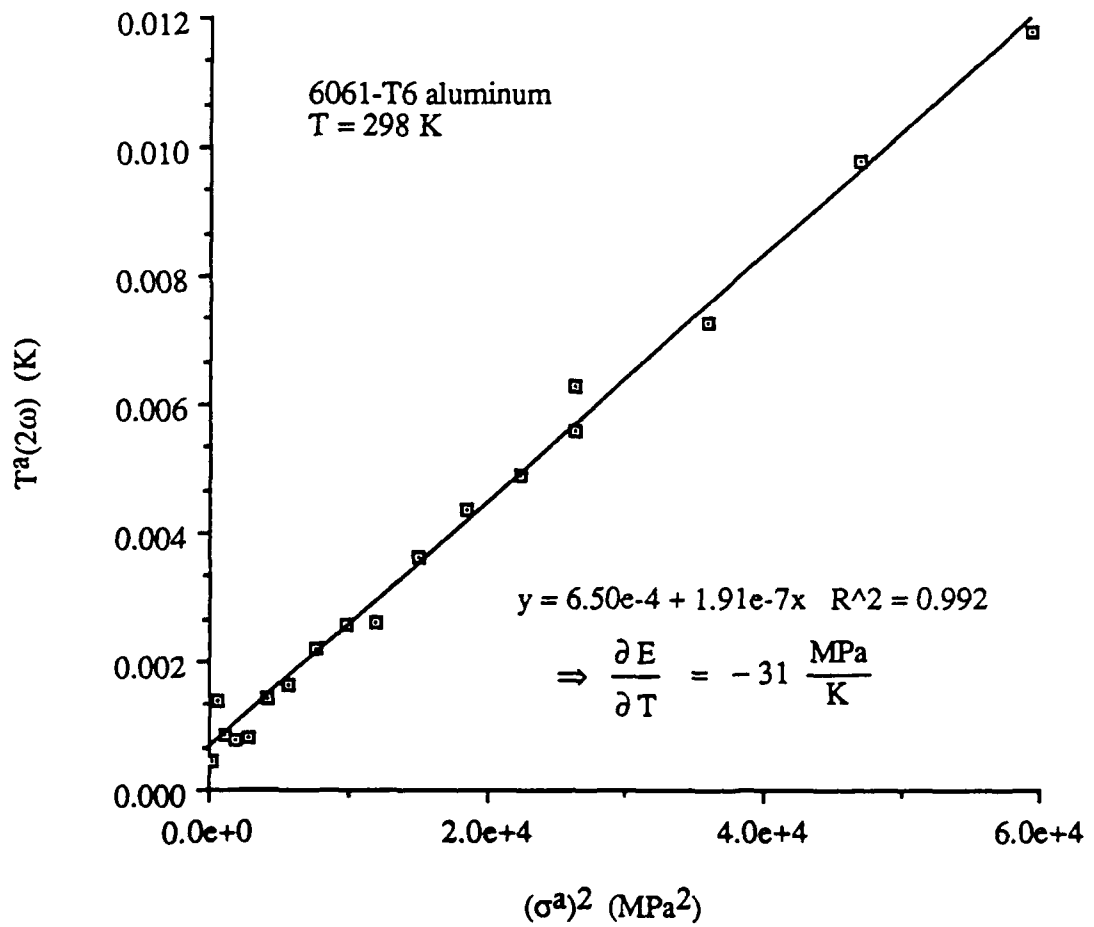
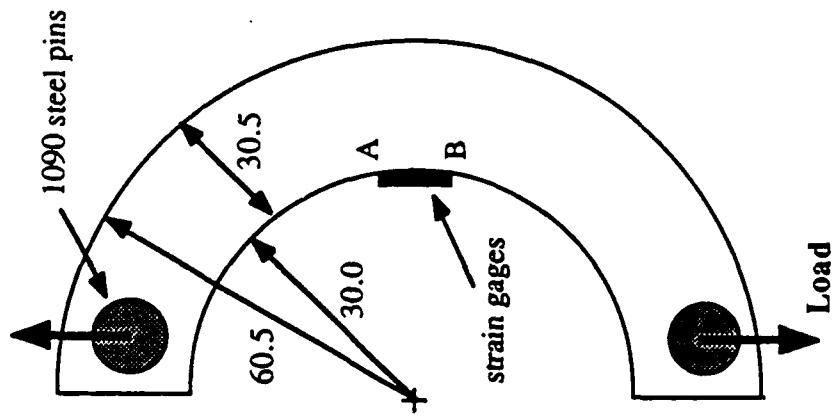
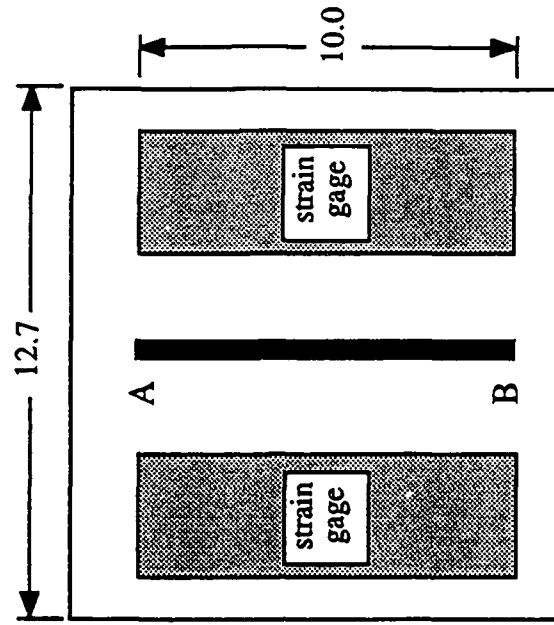


Figure 11 Nonlinear thermoelastic effect at twice the specimen cycling frequency for 6061-T6 aluminum

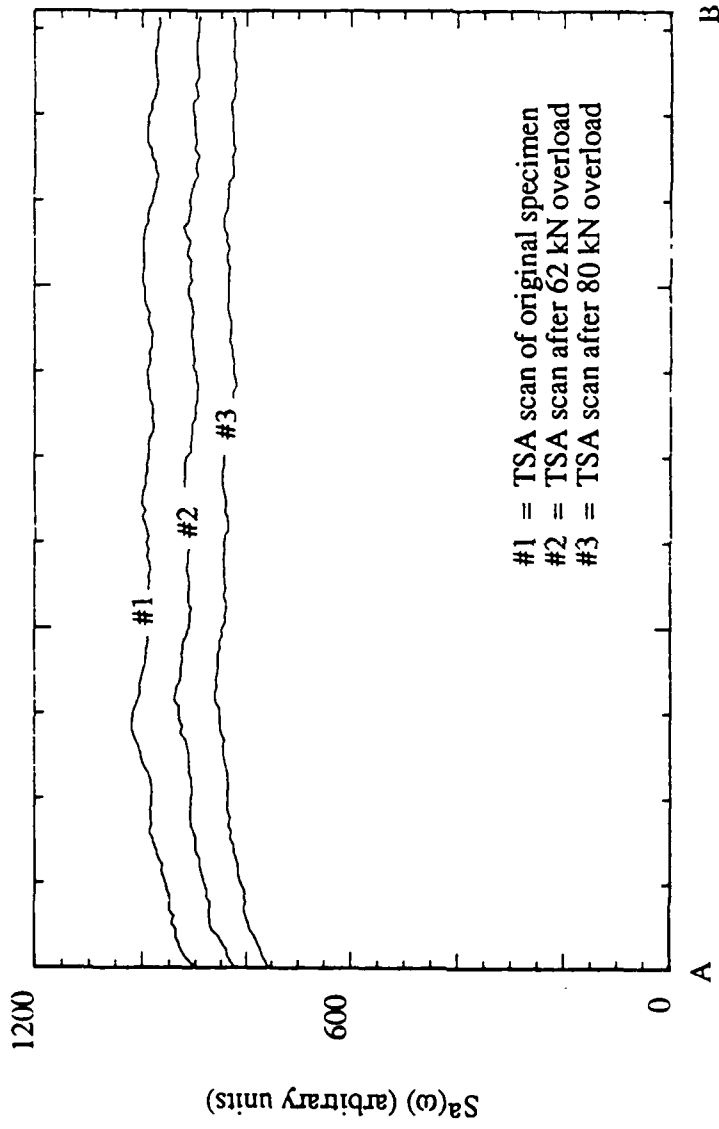


a) Side view



b) Close-up front view

Figure 12 Geometry of the Ti-6Al-4V C-specimen



Distance (arbitrary units - see Fig. 12)

Figure 13 TSA line scans for the Ti-6Al-4V C-specimen after various overloads

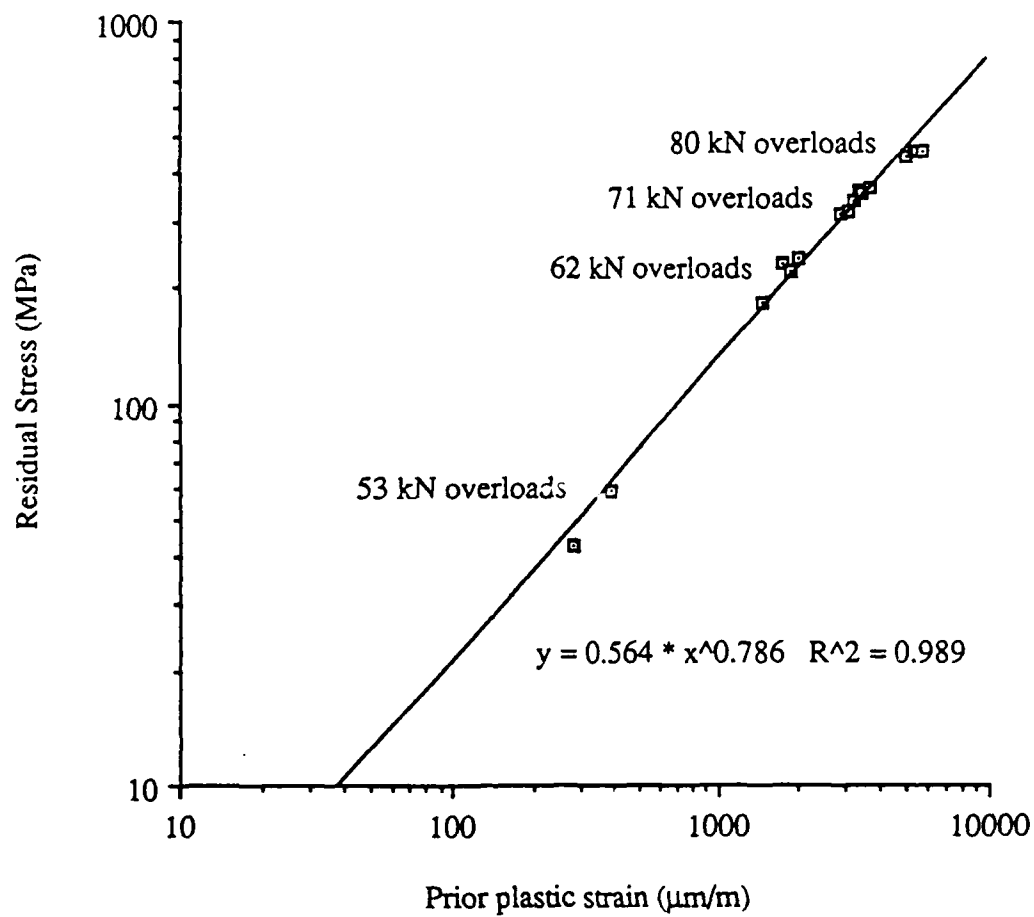


Figure 14 Estimated residual stress versus prior plastic strain for the Ti-6Al-4V C-specimen

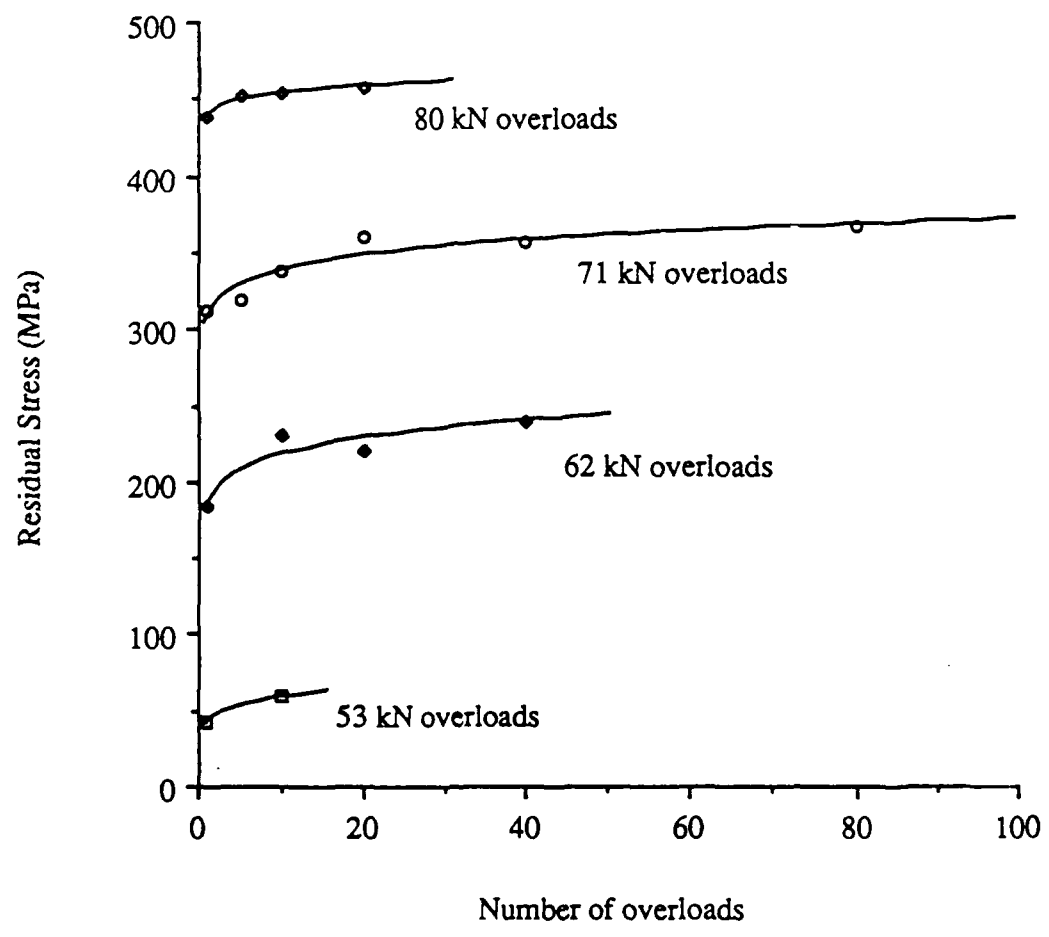
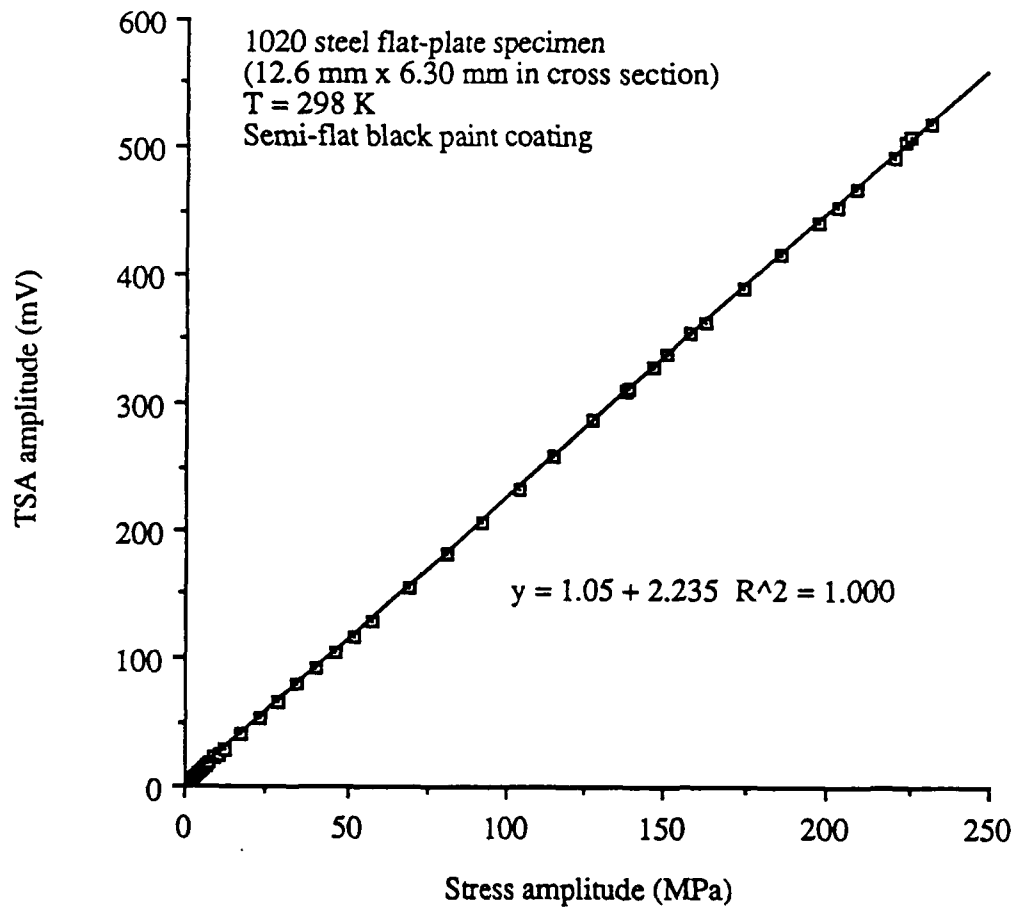
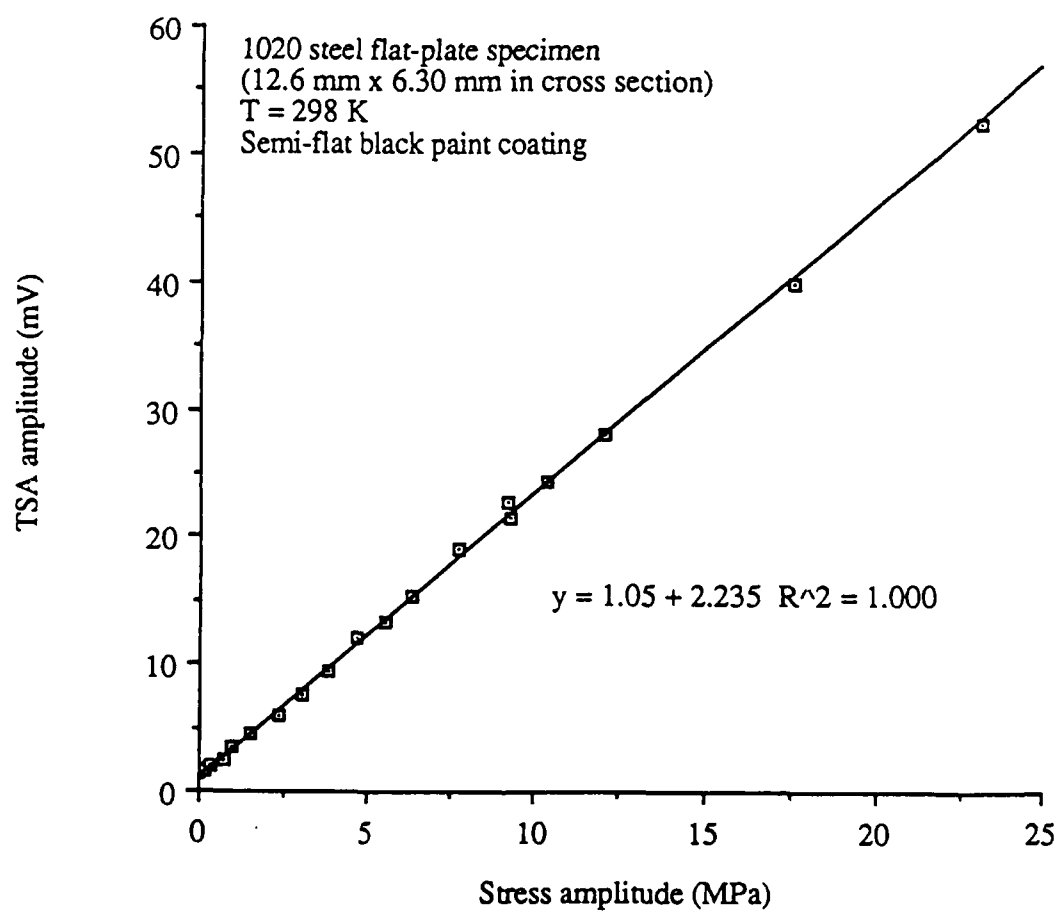


Figure 15 Estimated residual stress versus number of overloads for the Ti-6Al-4V C-specimen



(a) Total curve

Figure 16  $S^2(\omega)$  versus stress amplitude for 1020 steel at room temperature



(b) Close-up of Fig. 16a for low stress amplitudes

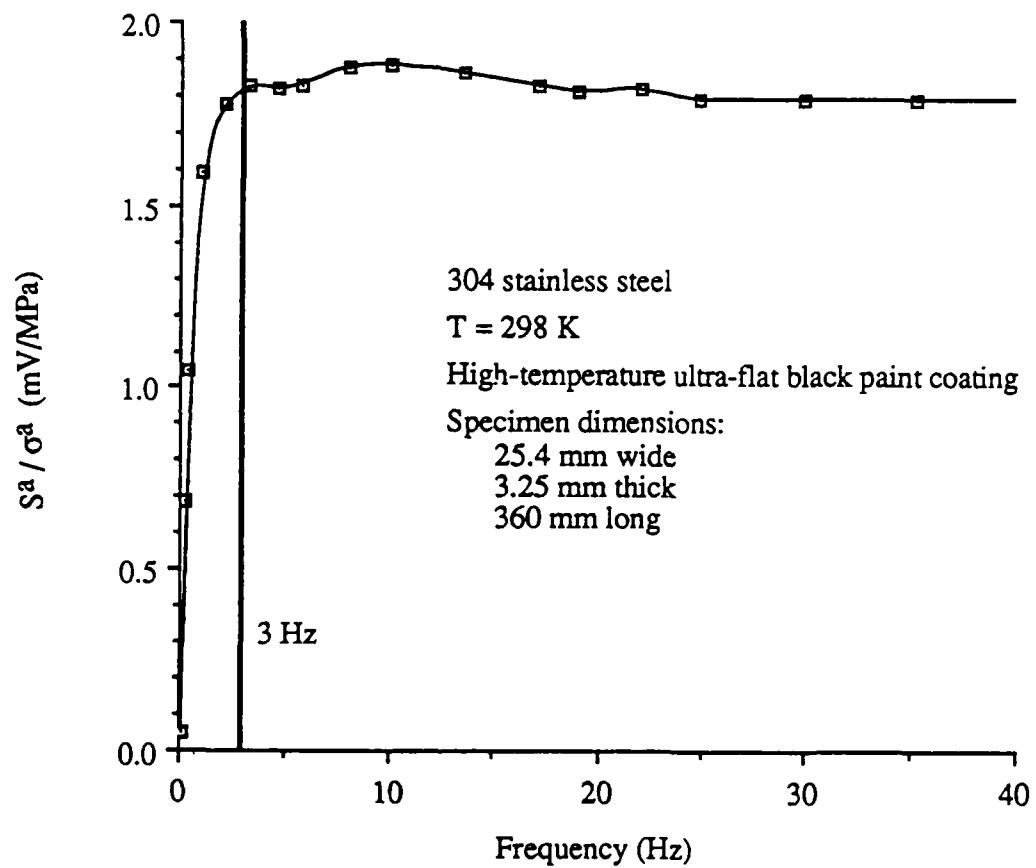
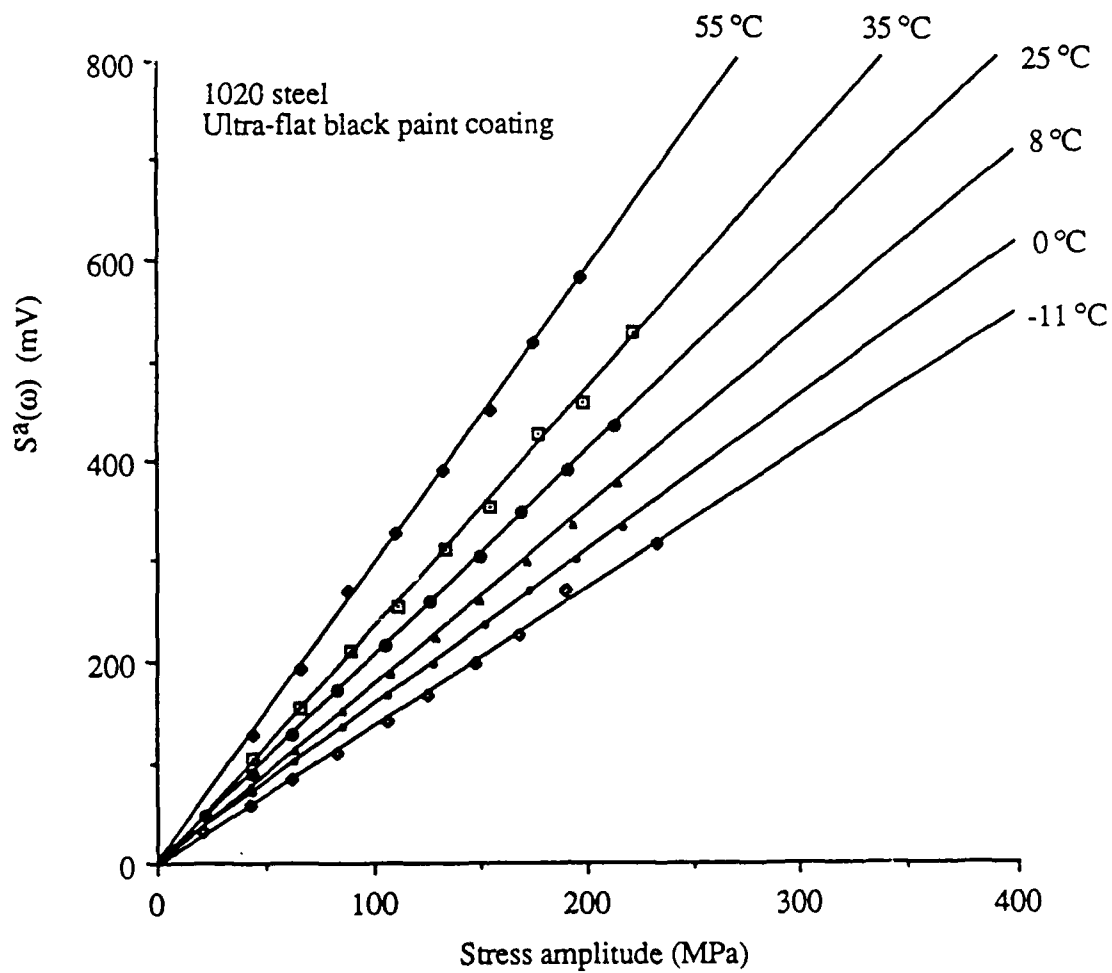
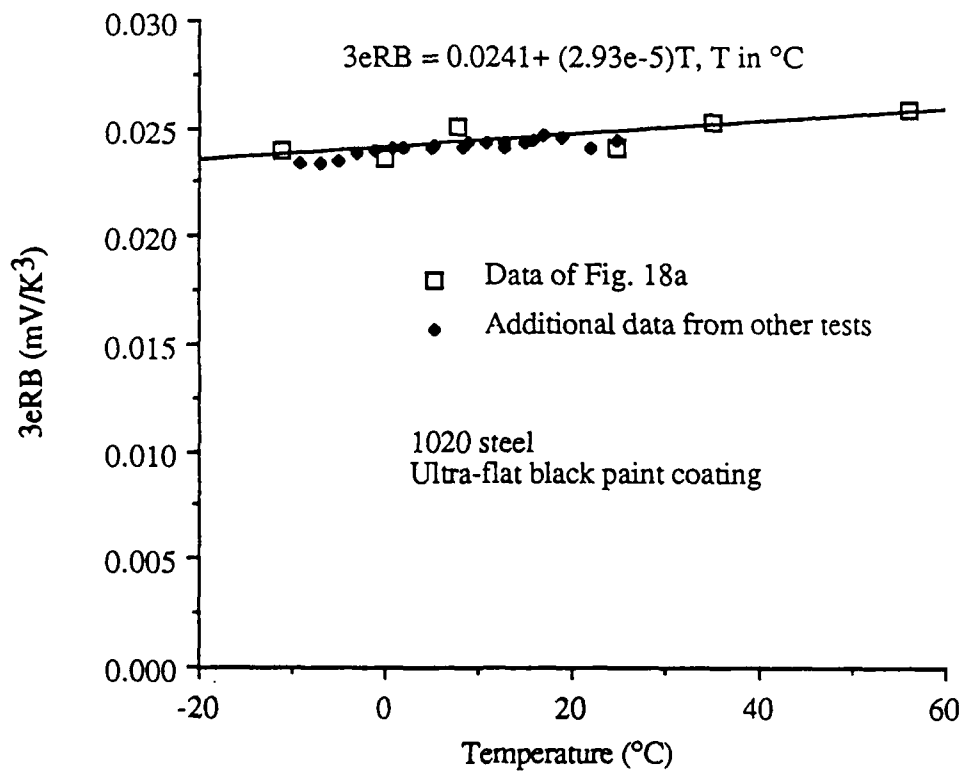


Figure 17 TSA calibration factor versus frequency for 304 stainless steel at room temperature



(a)  $S^a(\omega)$  versus stress amplitude for 1020 steel at various temperatures

Figure 18 Absolute calibration of the SPATE system from -11 °C to 55 °C



(b) 3eRB versus temperature

Figure 18 (continued)

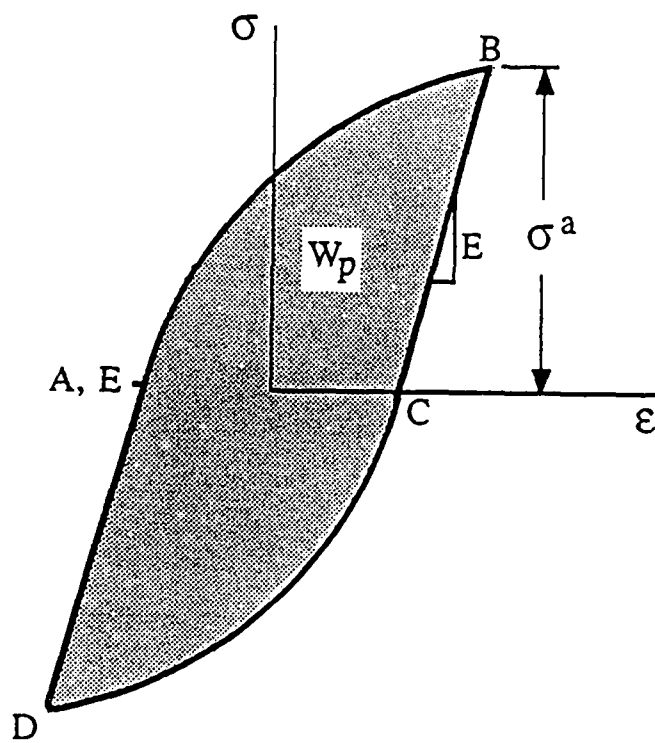


Figure 19 Shape of a "generic" hysteresis loop

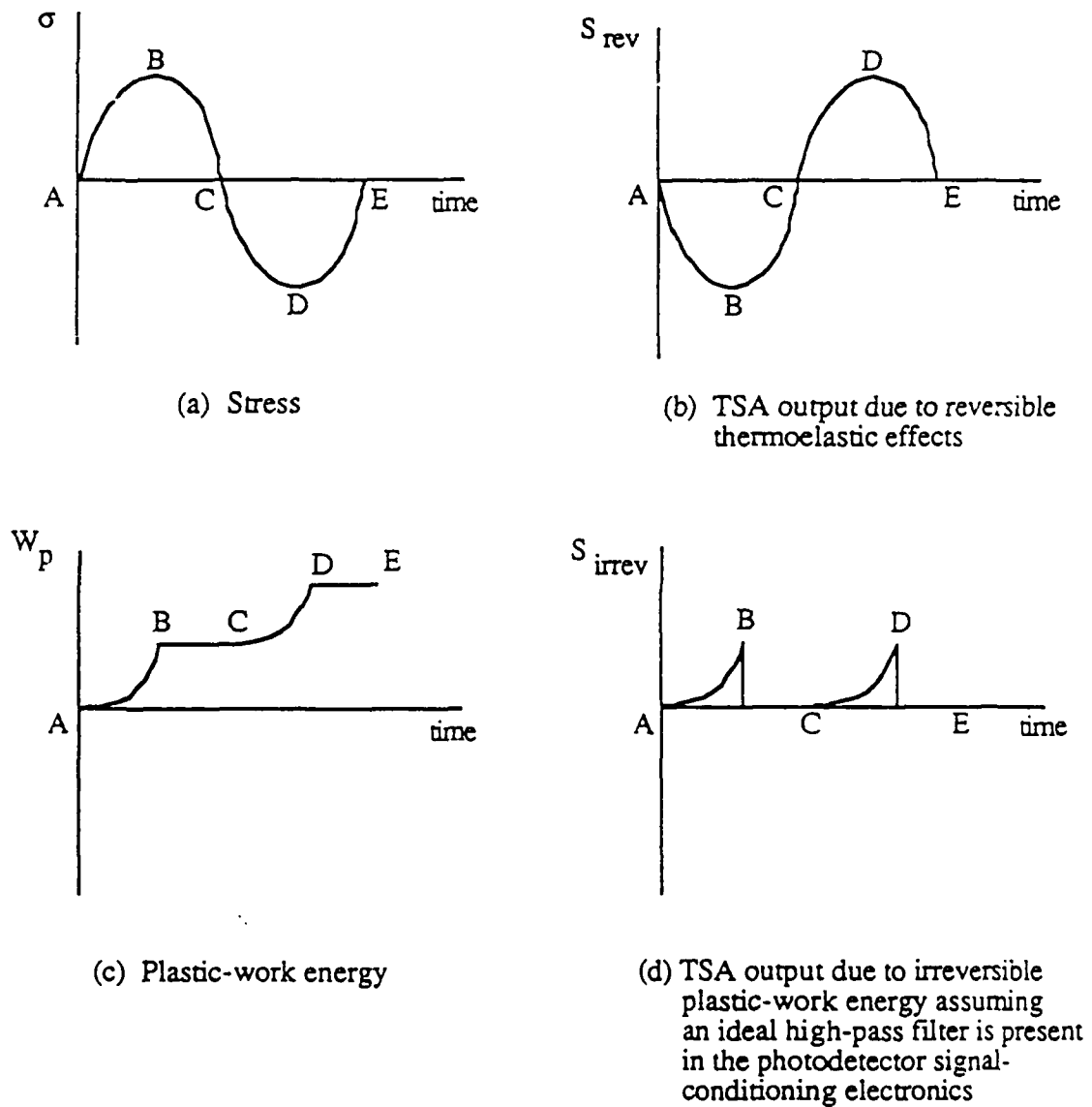


Figure 20 Effect of a single cycle of sinusoidal stress on the TSA output for elastic-plastic loading conditions

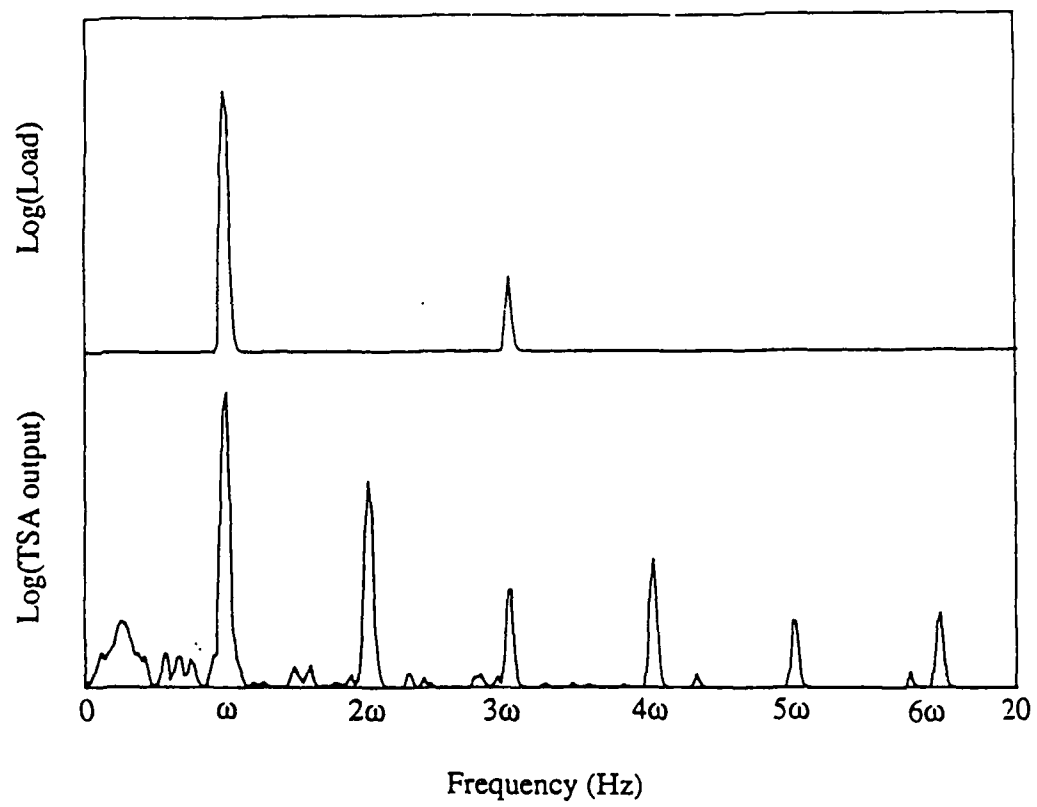
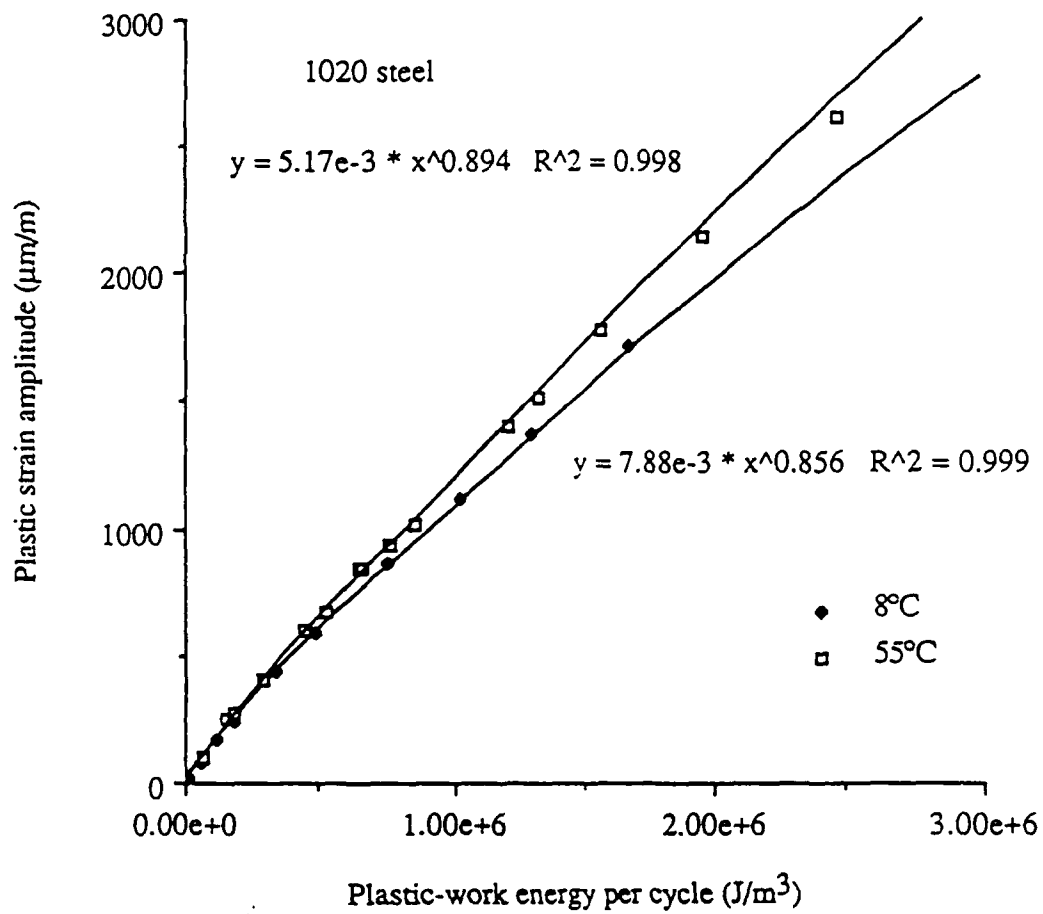
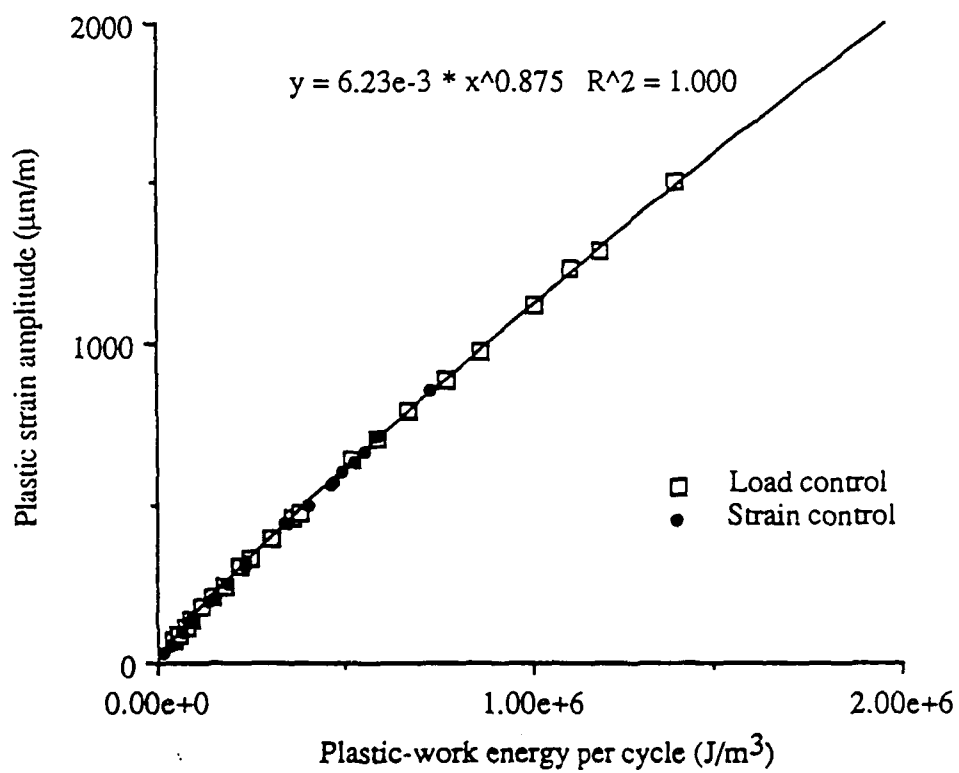


Figure 21 FFT of load and TSA outputs for a 1020 steel specimen undergoing cyclic plasticity



(a) Temperatures of 8 °C and 55 °C

Figure 22 Plastic-work energy per cycle versus plastic strain amplitude for 1020 steel



(b) Temperature = 25 °C

Figure 22 (continued)

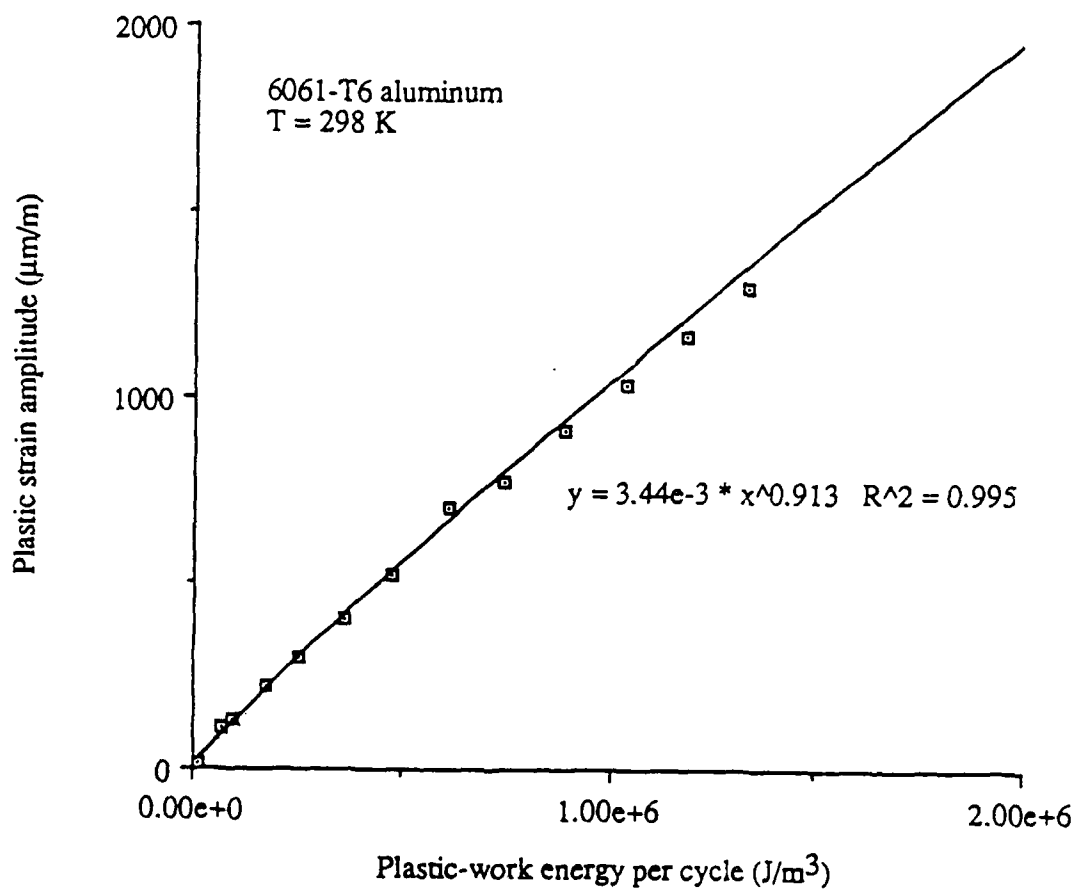
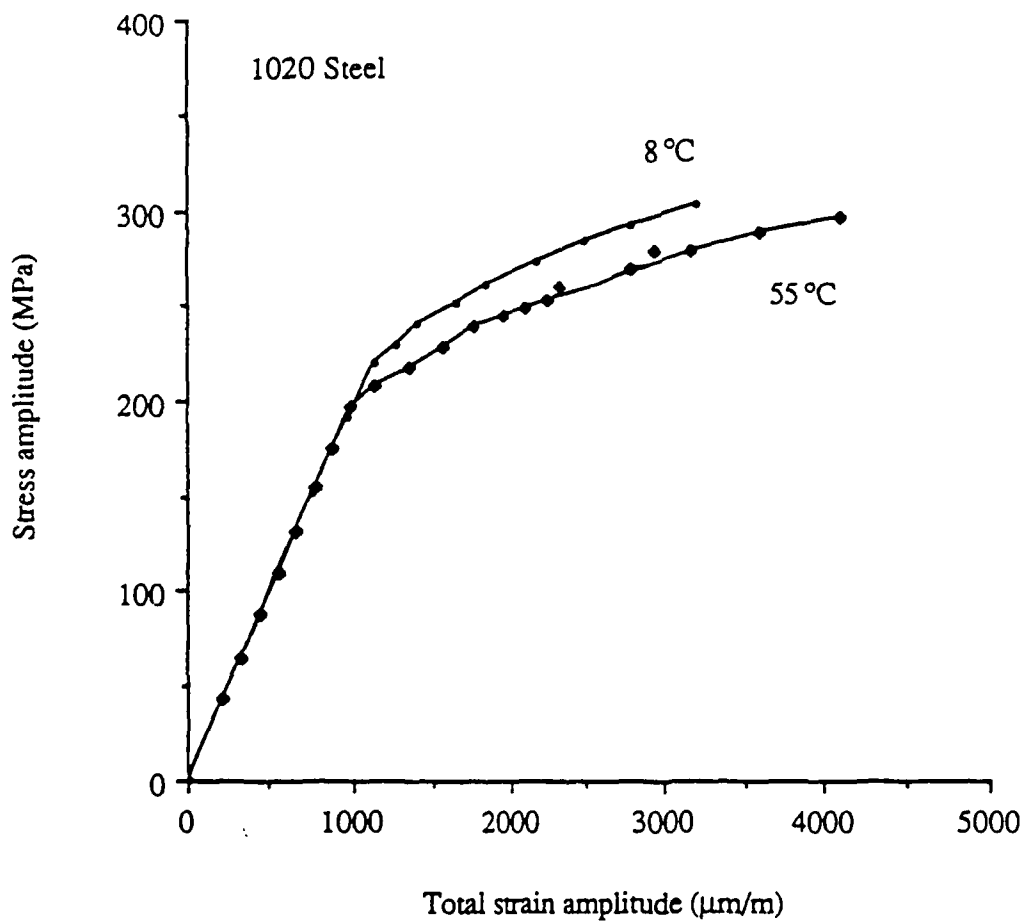
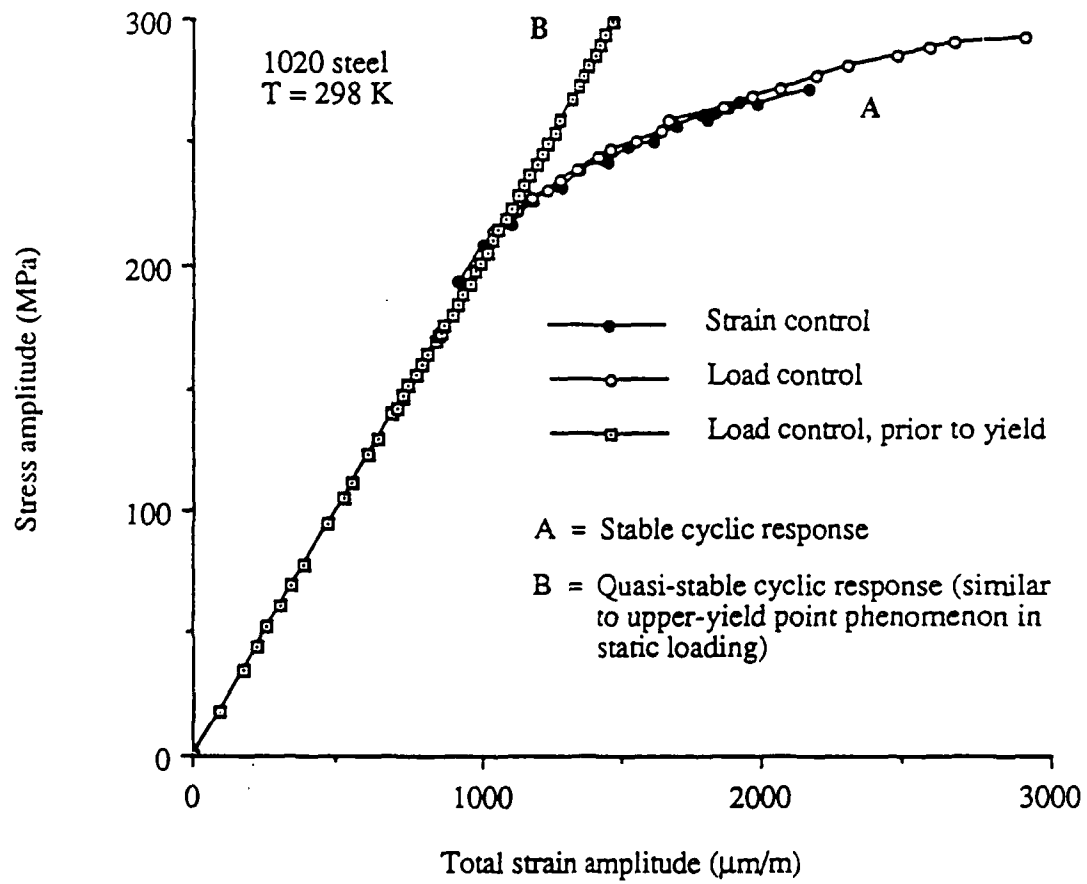


Figure 23 Plastic-work energy per cycle versus plastic strain amplitude for 6061-T6 aluminum at 25 °C



(a) Temperatures of 8 °C and 55 °C

Figure 24 Cyclic stress-strain curves for 1020 steel



(b) Temperature = 25 °C

Figure 24 (continued)

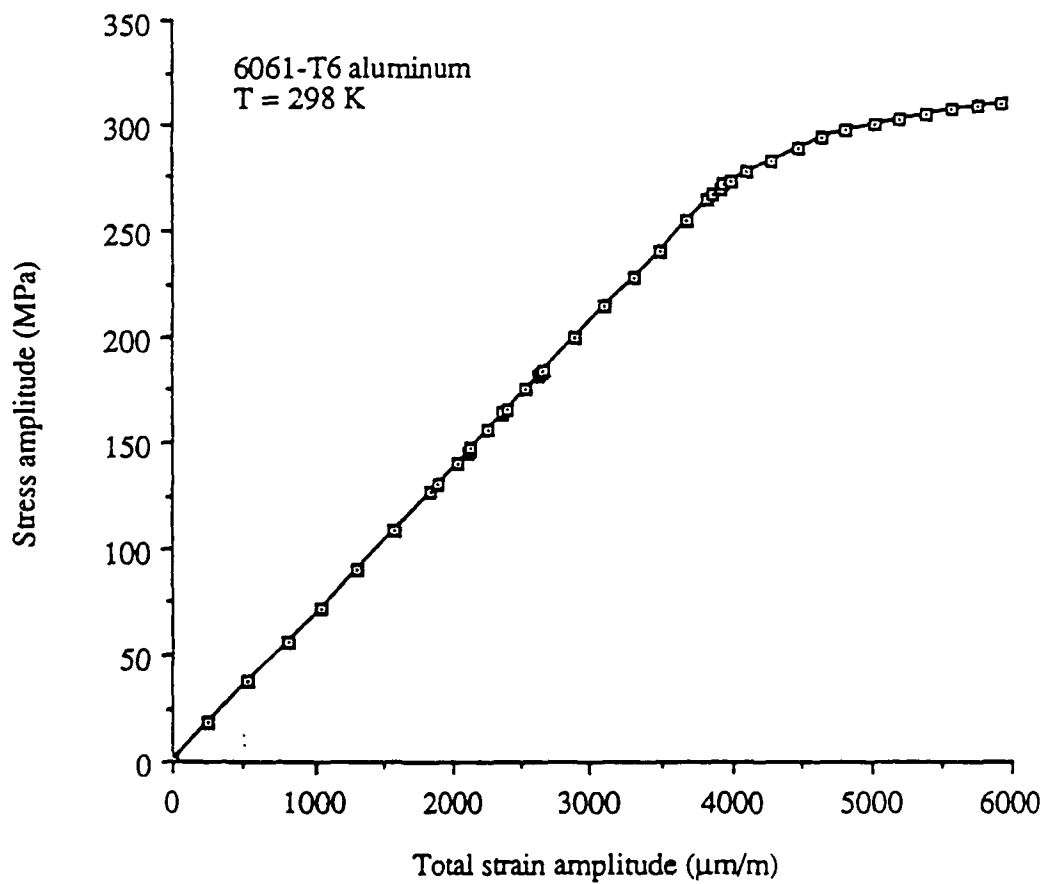
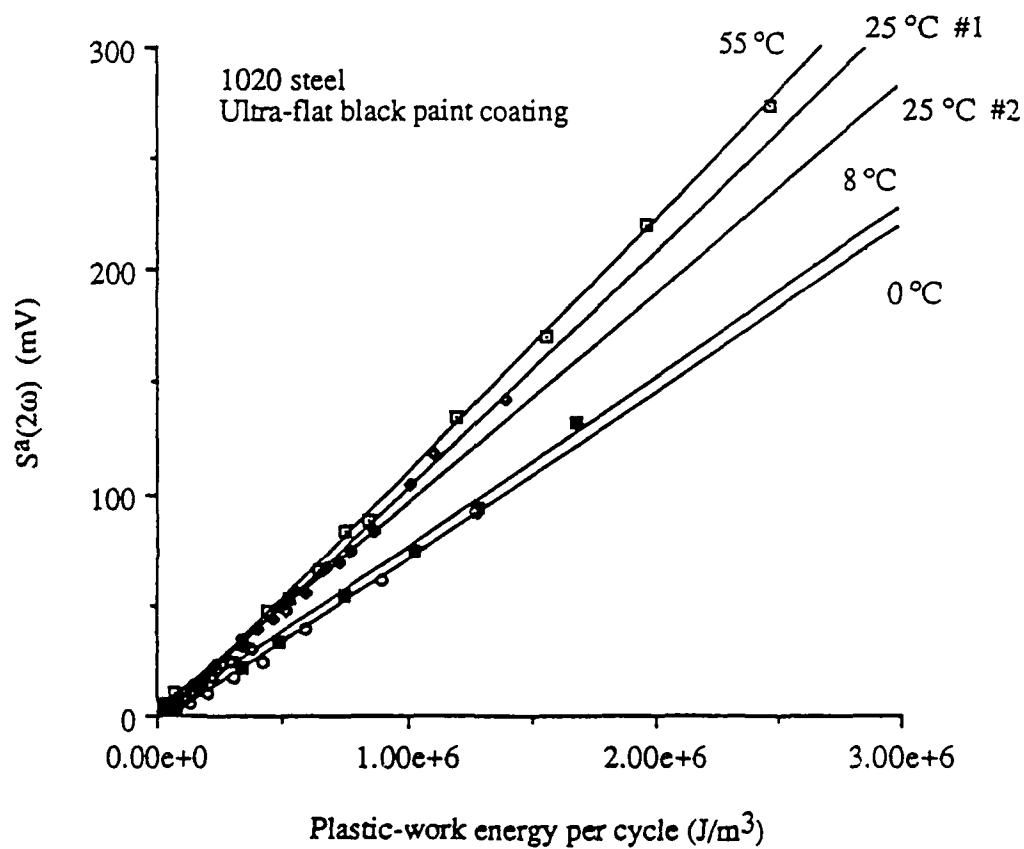


Figure 25 Cyclic stress-strain curve for 6061-T6 aluminum



Data for 0 °C, 8 °C, 55 °C and 25 °C #1 are for load-controlled cycling  
Data for 25 °C #2 are for strain-controlled cycling

Figure 26 Plastic-work energy per cycle versus  $S^2(2\omega)$  for 1020 steel

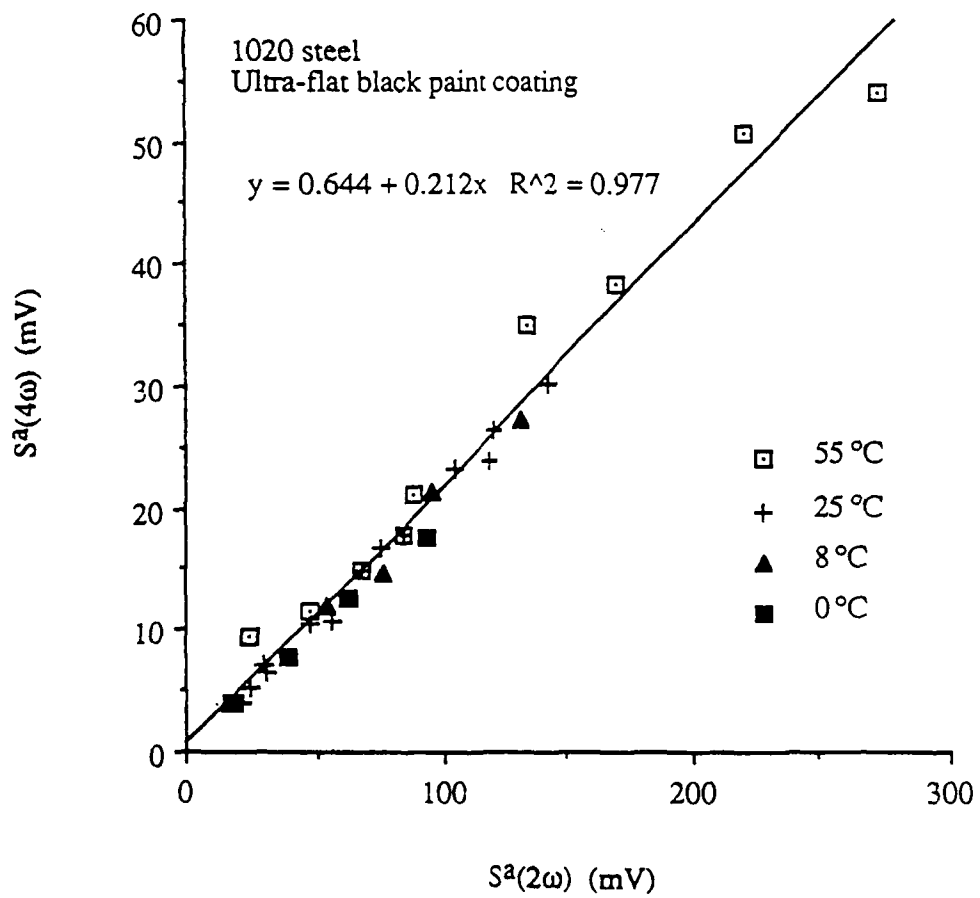
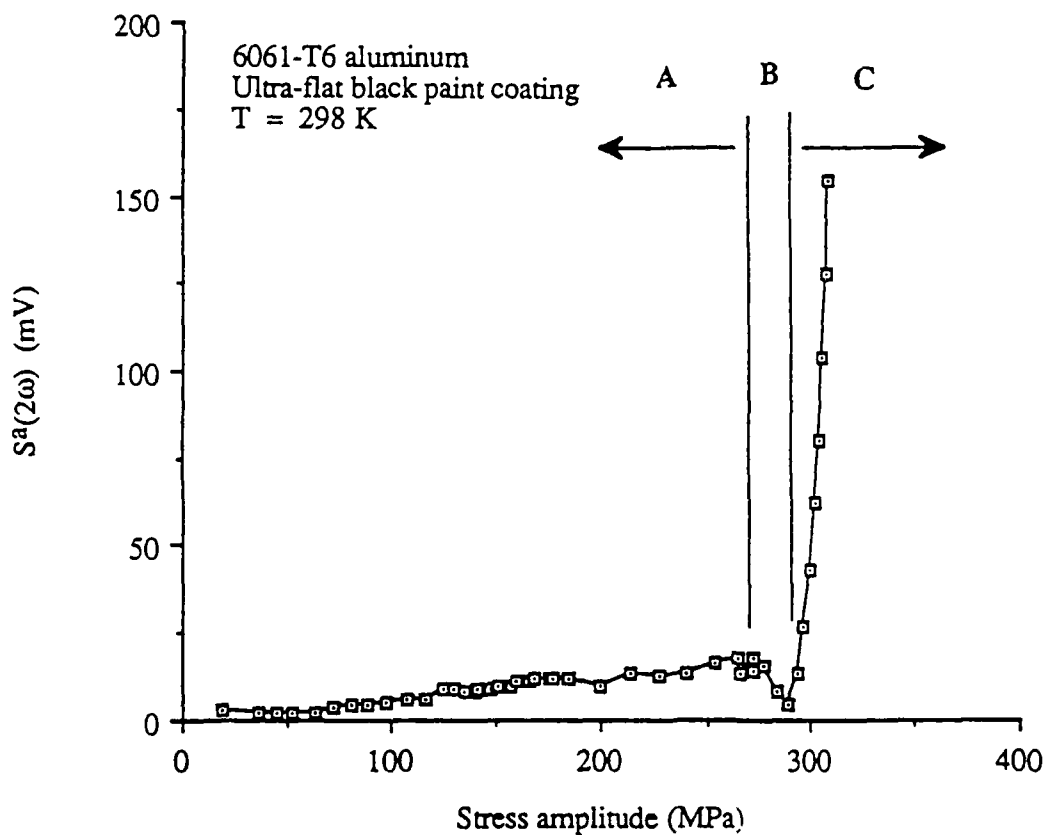


Figure 27  $S^a(2\omega)$  versus  $S^a(4\omega)$  for 1020 steel



Region A - Nonlinear thermoelastic effects dominate

Region B - Nonlinear thermoelastic and thermoplastic effects interfere destructively

Region C - Thermoplastic effects dominate

(a)  $S^a(2\omega)$  versus stress amplitude

Figure 28  $S^a(2\omega)$  versus stress amplitude and plastic-work energy per cycle for 6061-T6 aluminum

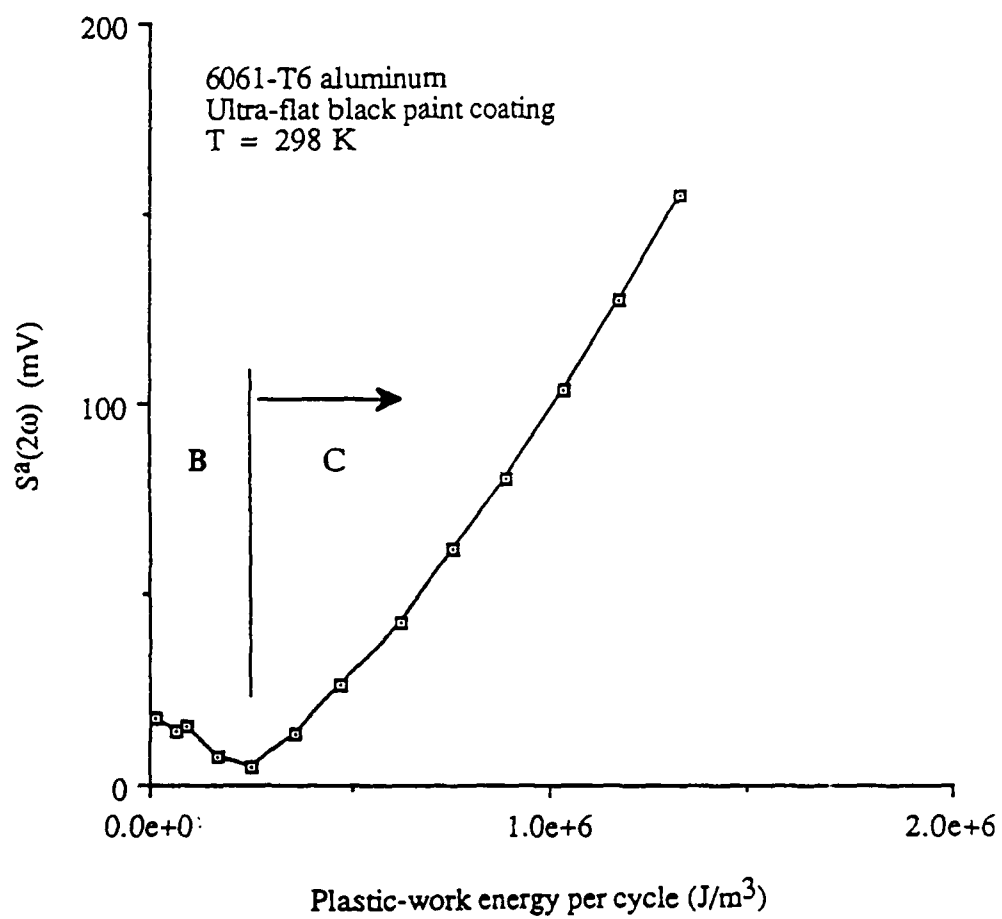
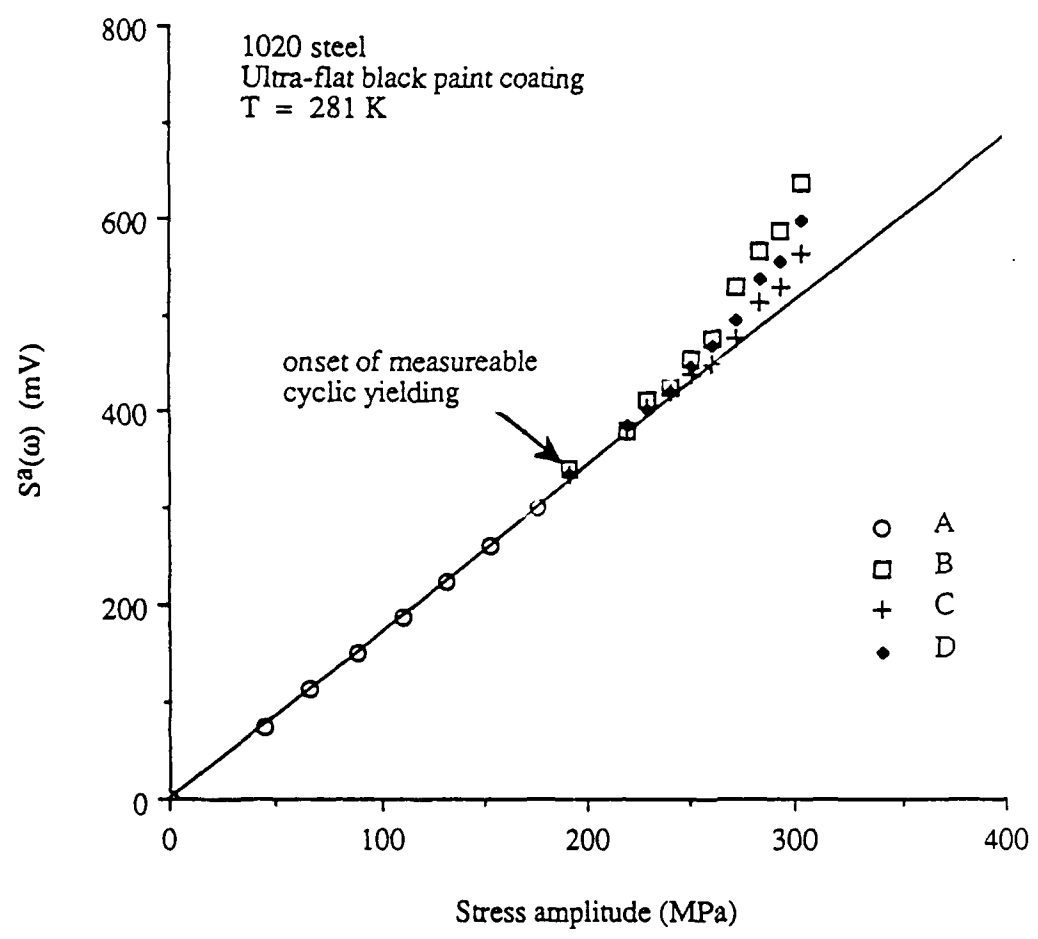
(b)  $S^a(2\omega)$  versus plastic-work energy

Figure 28 (continued)



- A = experimental data for elastic response
- B = experimental data for elastic-plastic response
- C = theoretical prediction based on measured specimen temperature
- D = theoretical prediction based on adiabatic specimen conditions

Figure 29  $S^a(\omega)$  versus stress amplitude for 1020 steel at 8 °C

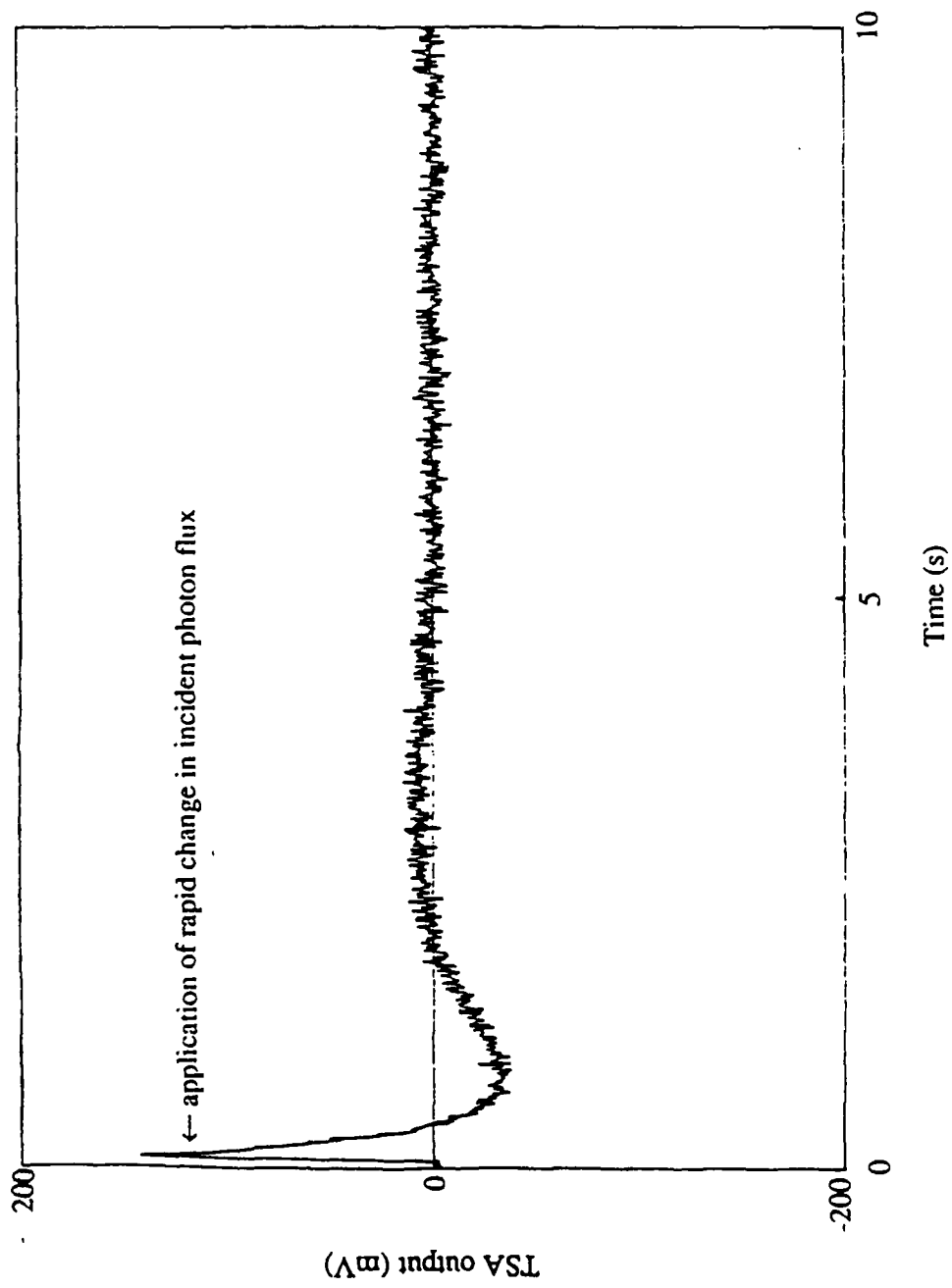
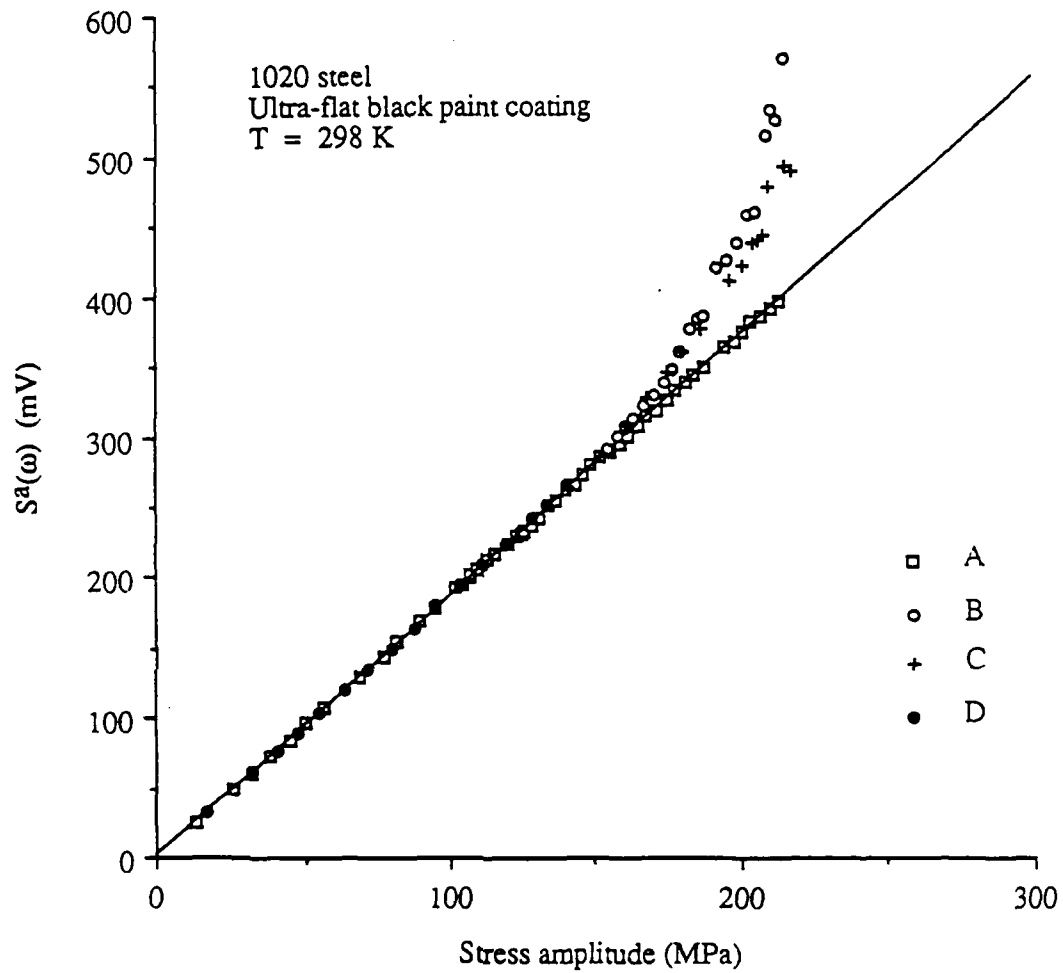


Figure 30 Effect of a rapid change in incident photon flux on the TSA output of the SPATE system



- A = elastic response before cyclic yielding  
 B = elastic-plastic response for load-controlled cycling  
 C = elastic-plastic response for strain-controlled cycling  
 D = elastic response after cyclic yielding

Figure 31  $S^a(\omega)$  versus stress amplitude for 1020 steel at 25 °C

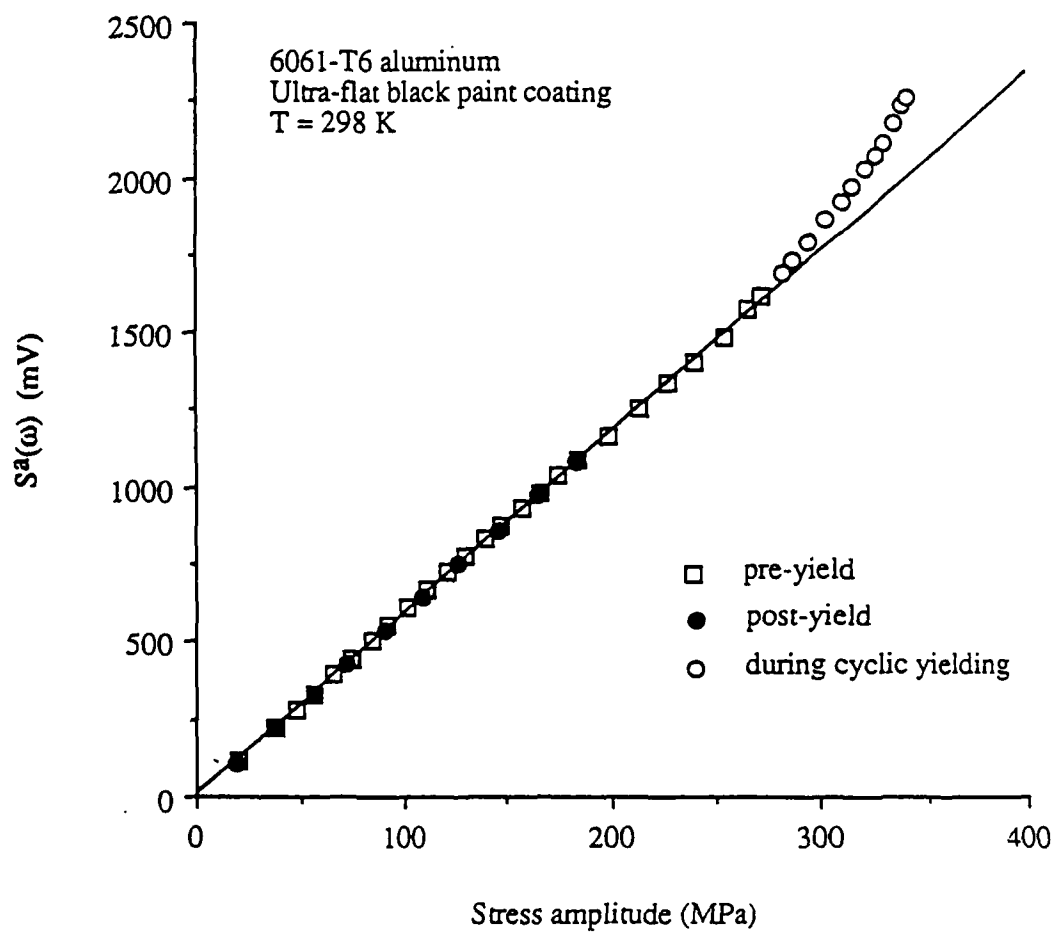


Figure 32  $S^a(\omega)$  versus stress amplitude for 6061-T6 aluminum at 25 °C

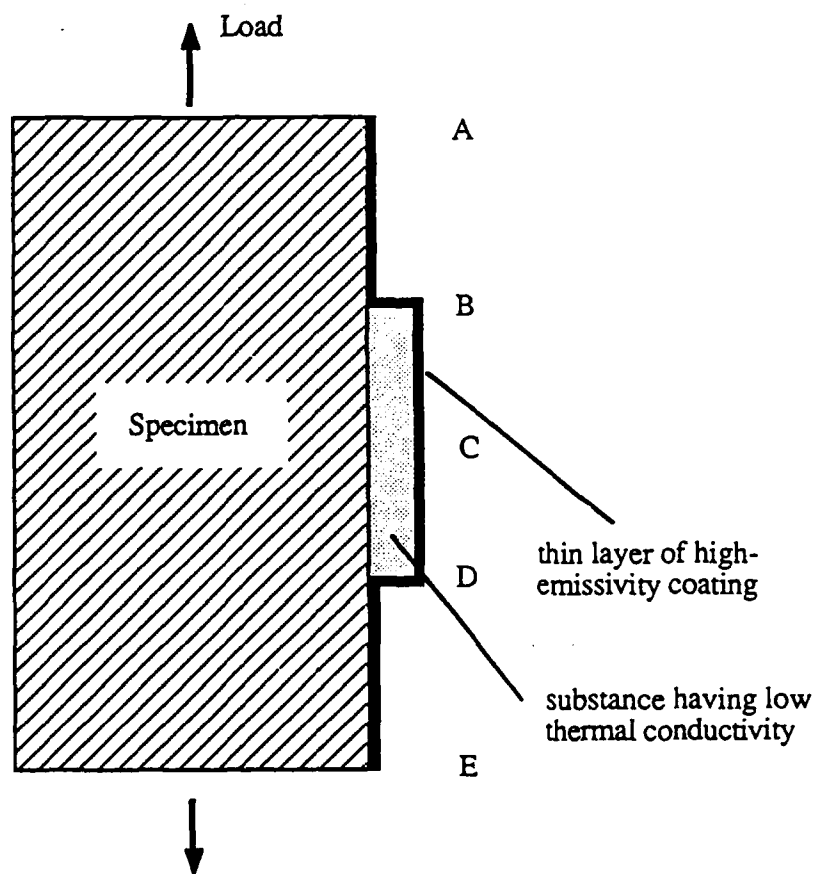
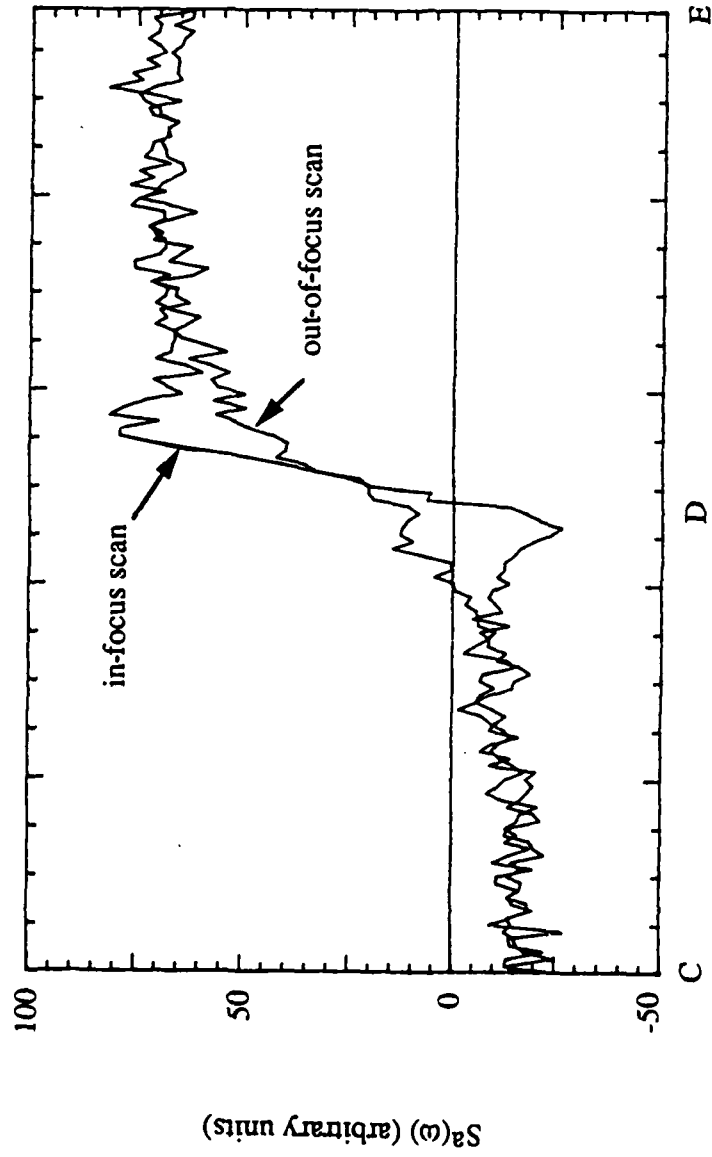


Figure 33 Specimen design used to determine proper focus settings for the SPATE infrared camera



Distance (arbitrary units - see Fig. 33)

Figure 34 Examples of in-focus and out-of-focus scans

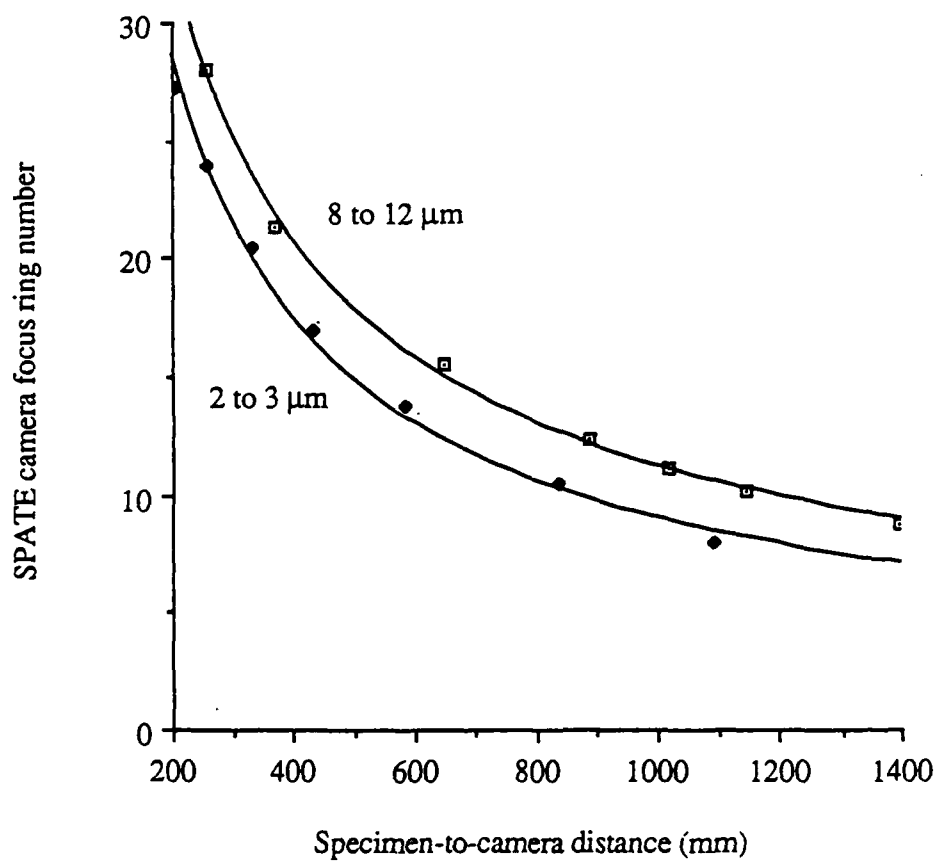
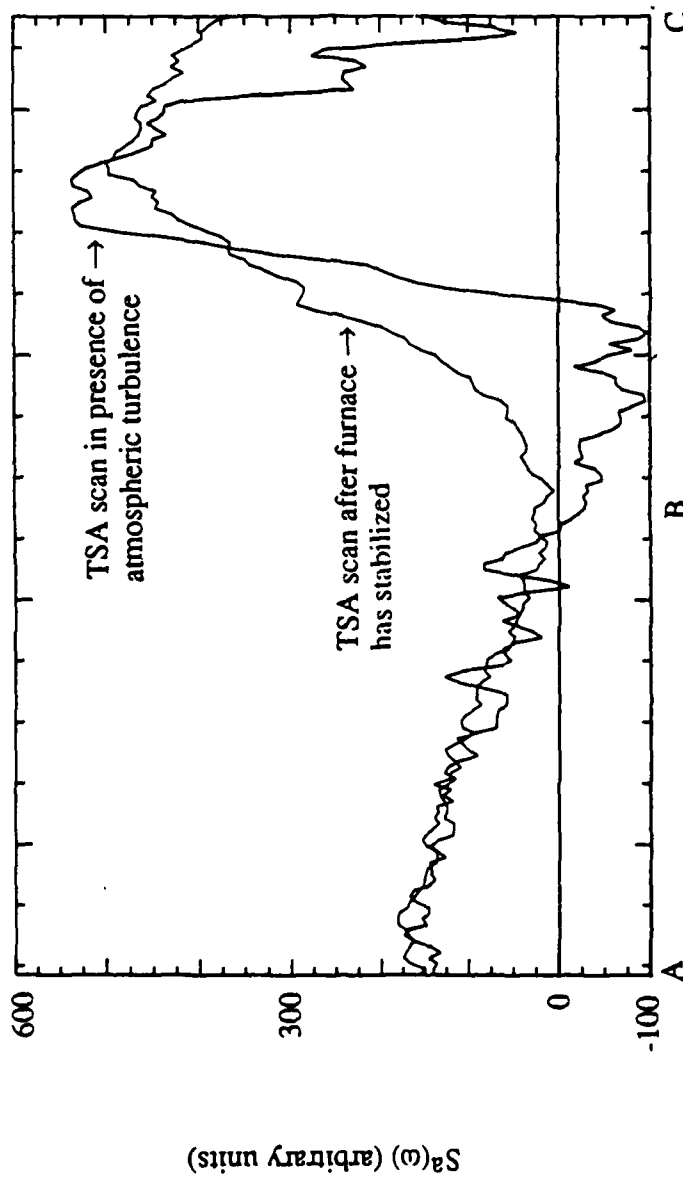
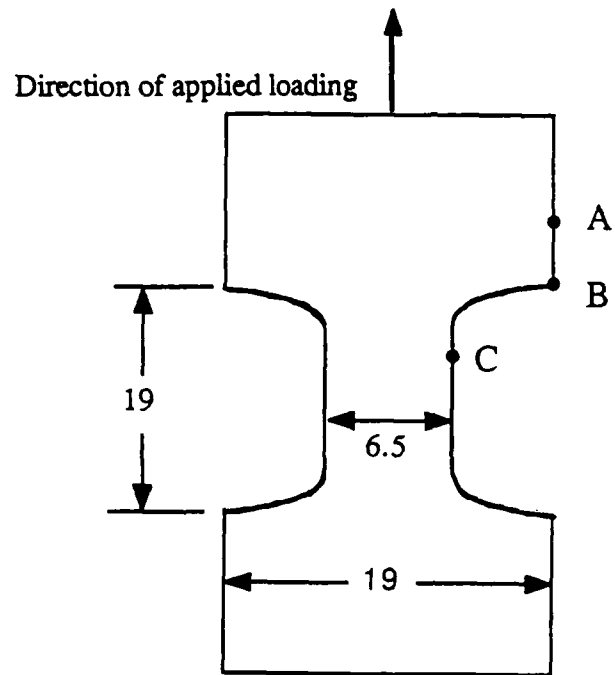


Figure 35 Focus curves of the SPATE infrared camera for 8 to 12  $\mu\text{m}$  and 2 to 3  $\mu\text{m}$

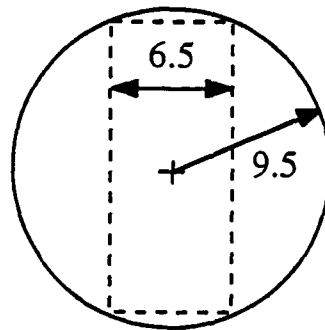


Distance (arbitrary units - see Fig. 37)

Figure 36 Example of the effects of atmospheric turbulence on the TSA output



(a) Side view



(b) Top view

Figure 37 Geometry of the Hastelloy-X specimen. All dimensions in mm.

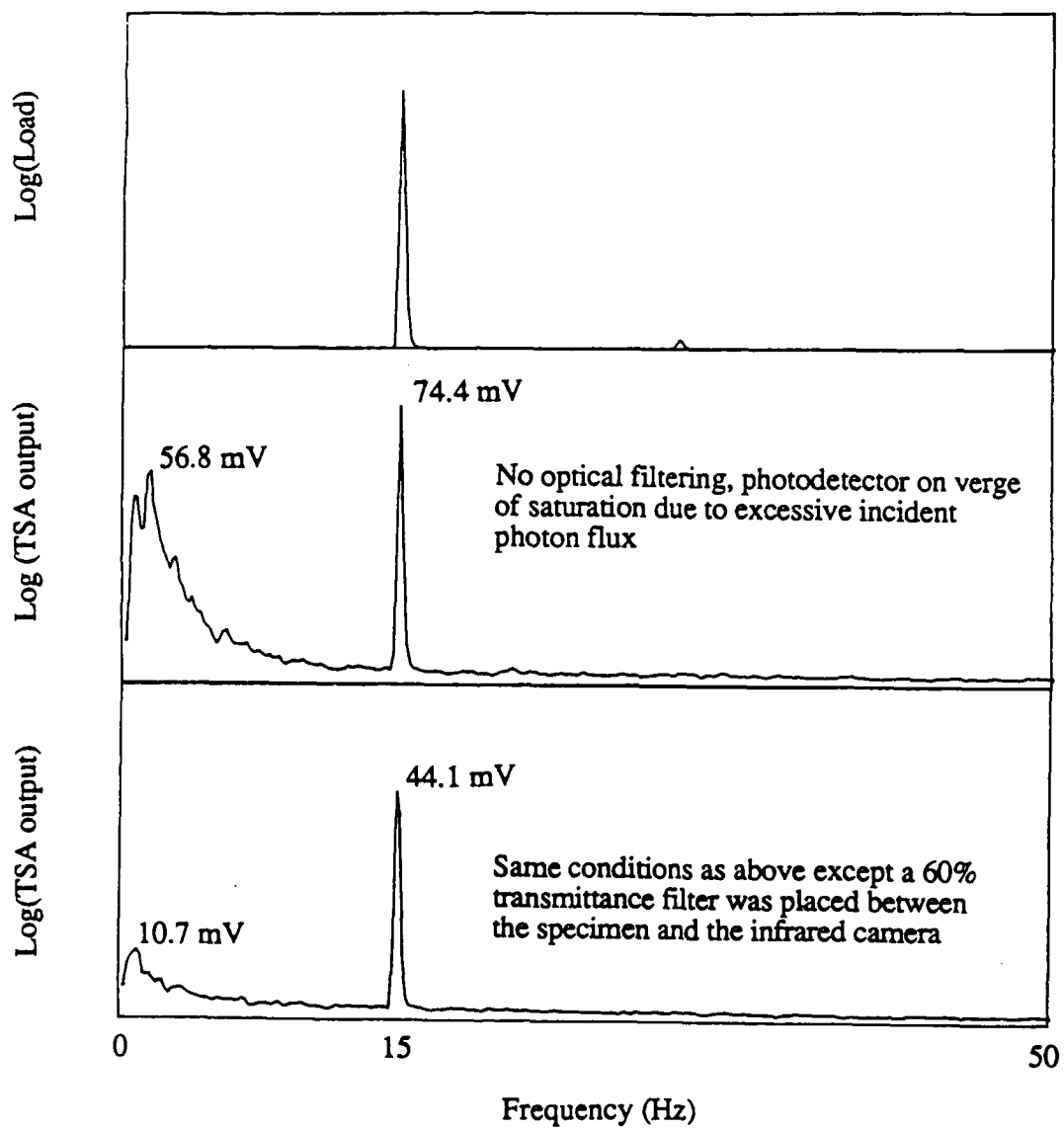


Figure 38 Effects of excessive incident photon flux on the TSA output

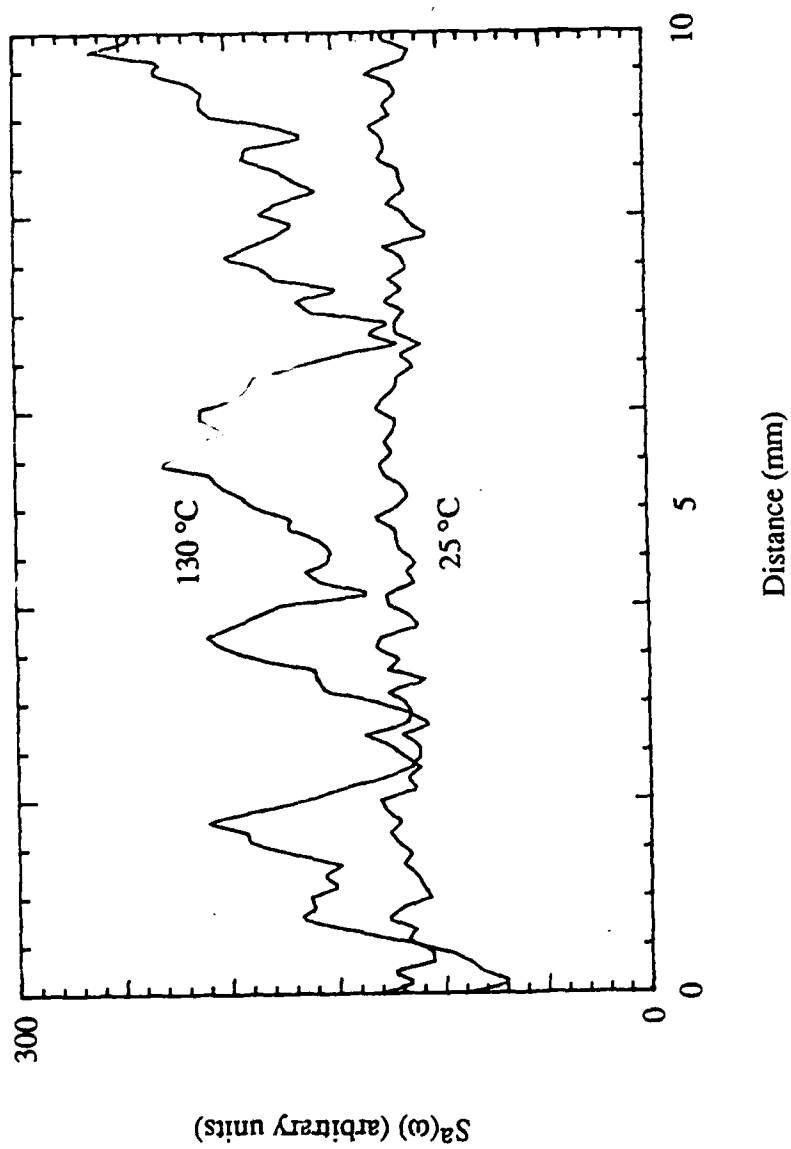


Figure 39 Effects of nonuniform spatial emissivity on the TSA output

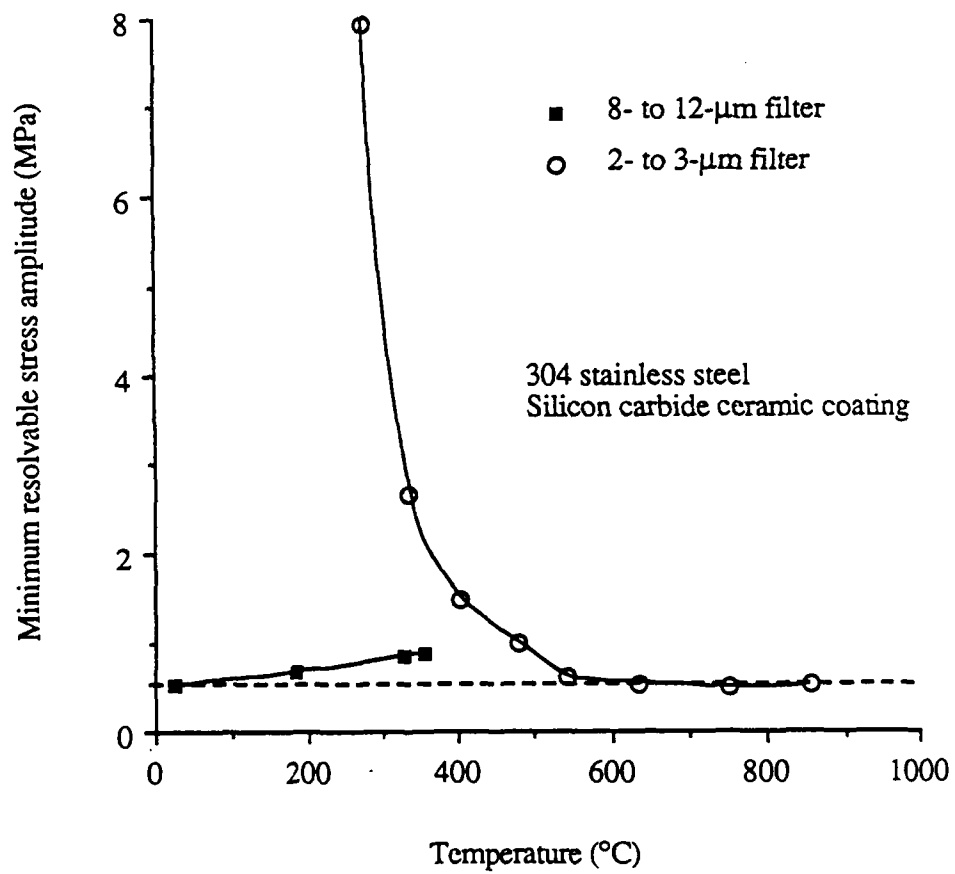


Figure 40 Minimum resolvable stress versus temperature

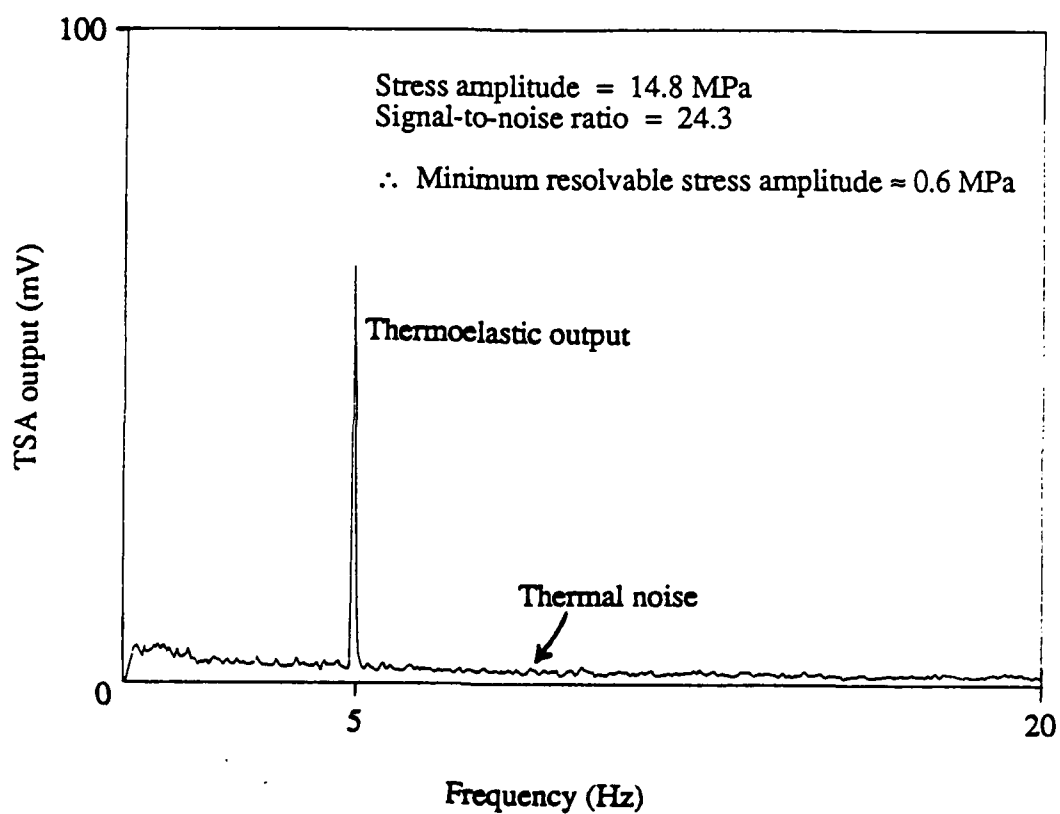
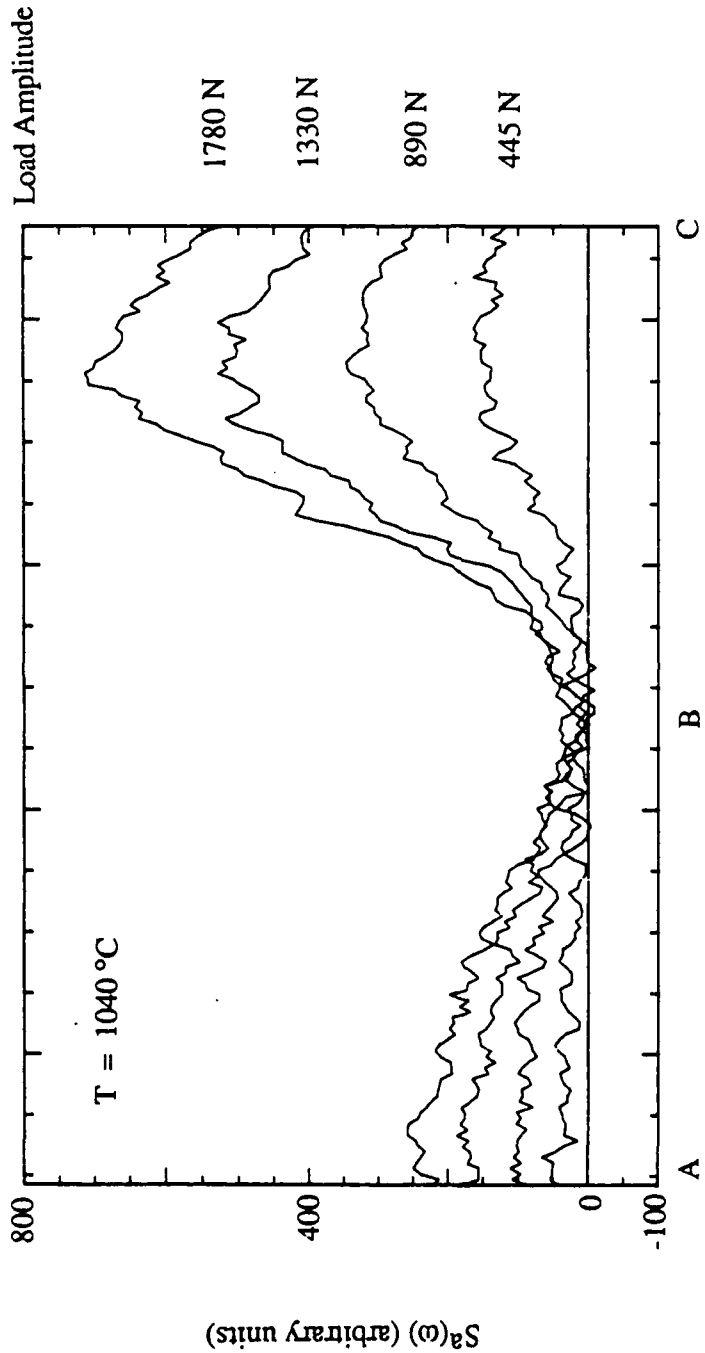


Figure 41 FFT of TSA output for Hastelloy-X specimen at 1040 °C



Distance (arbitrary units - see Fig. 37)

Figure 42 TSA line scans of Hastelloy-X specimen at four different load amplitudes

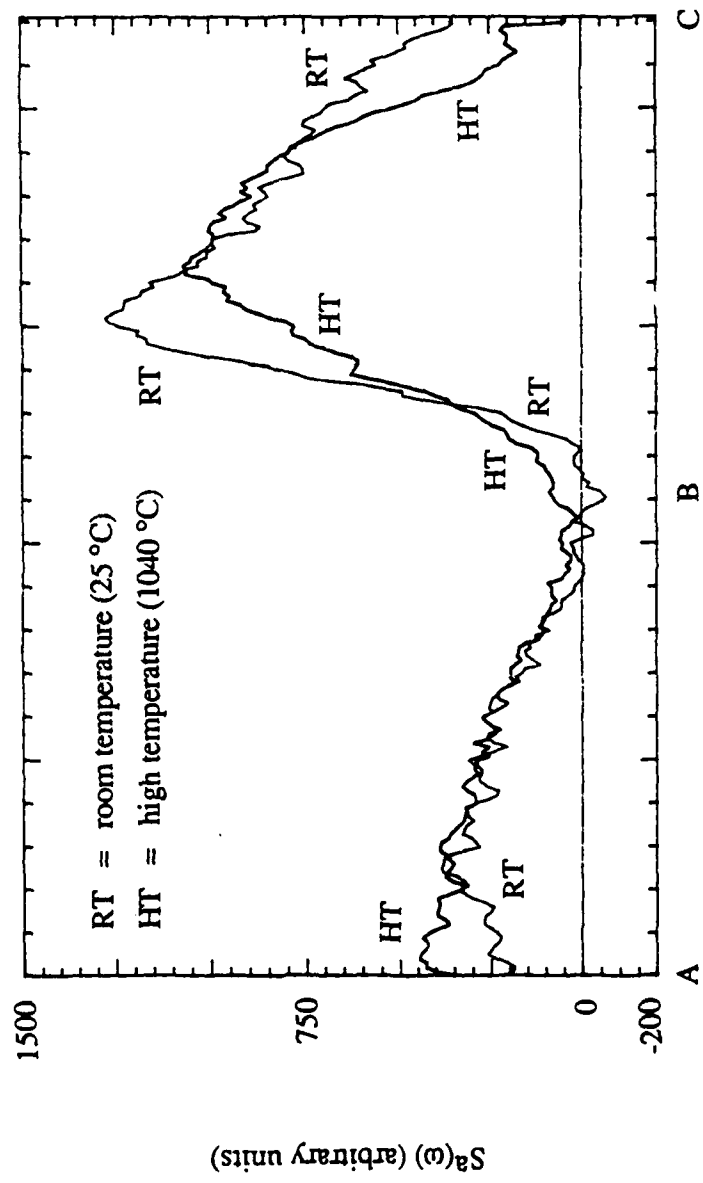
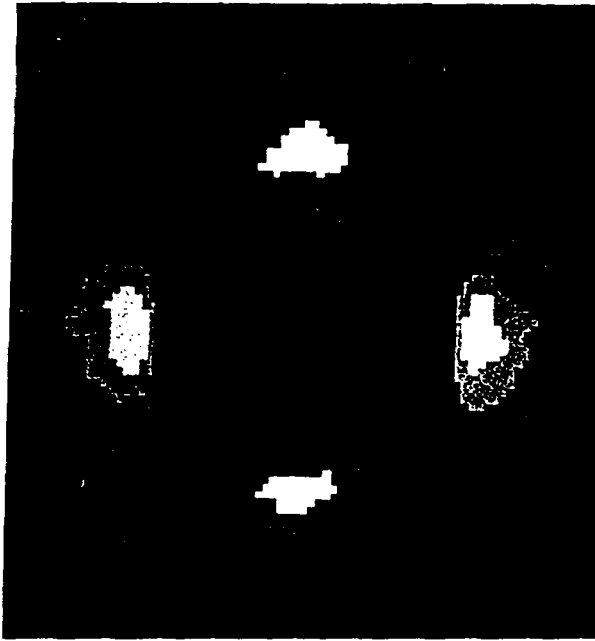
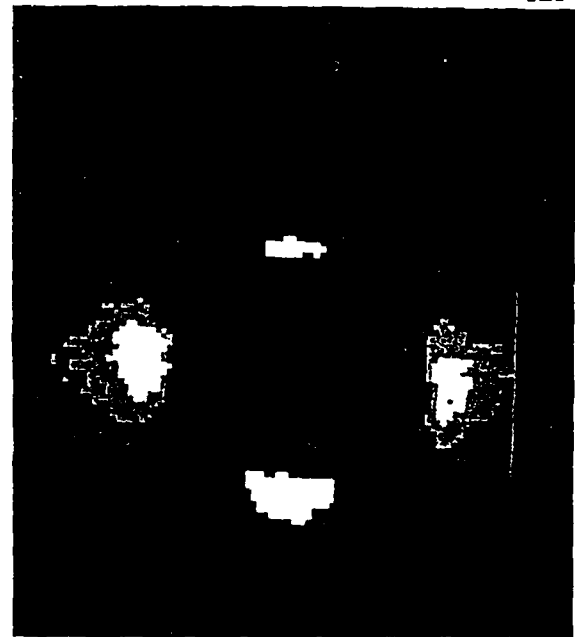


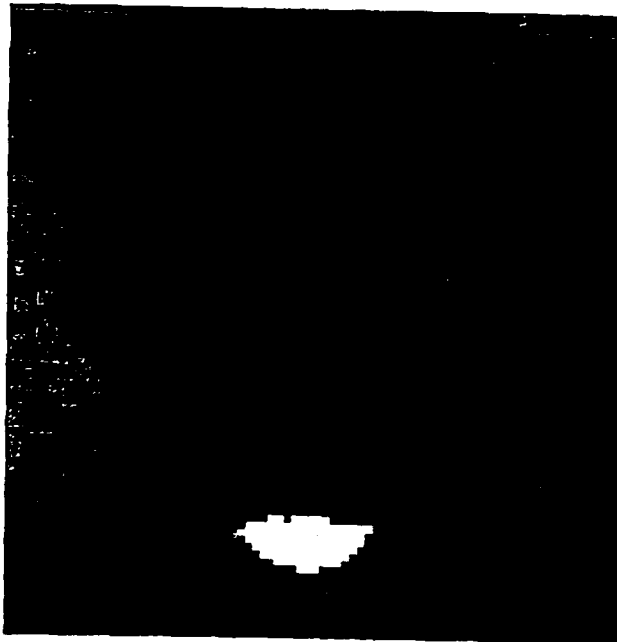
Figure 43 Comparison of TSA line scans of Hastelloy-X specimen at 25 °C and 1040 °C



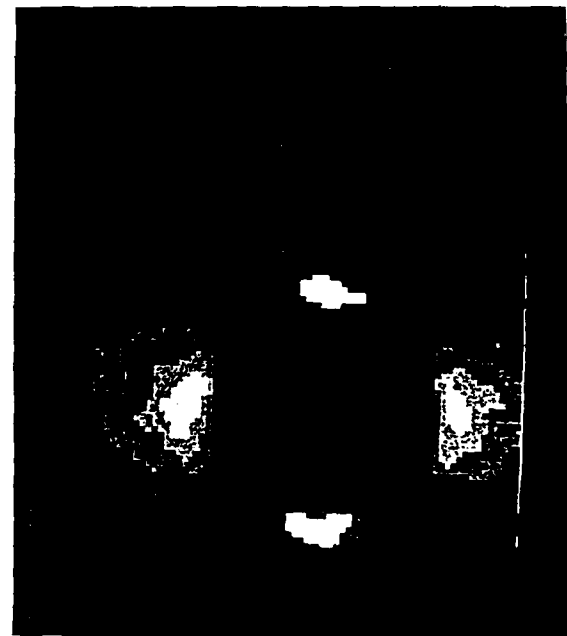
(a) 23°C



(b) 100°C



(c) 300°C



(d) 800°C

Figure 44a, b, c and d TSA frame scans of 304 stainless steel with 1/4" diameter hole in center at temperatures of (a)23°C, (b)100°C, (c)300°C and (d)800°C. Specimen is coated with silicon carbide ceramic coating.

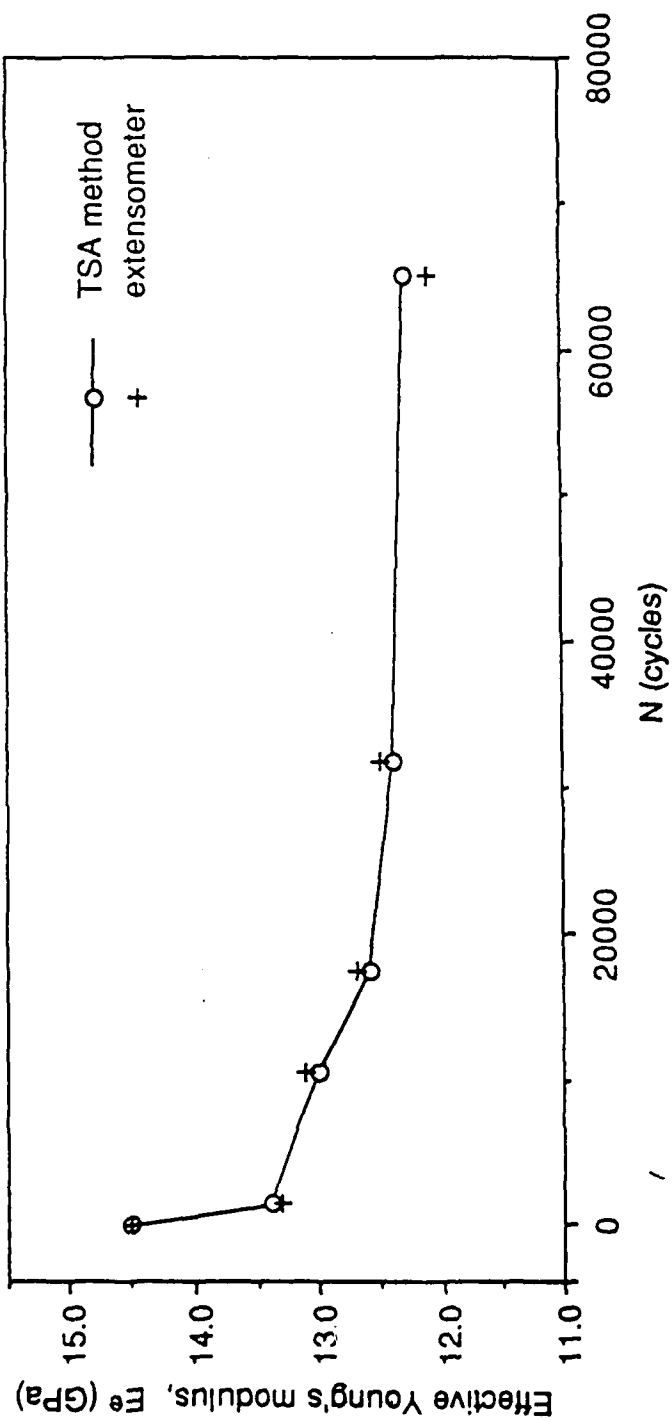


Figure 45 Comparison of effective modulus  $E_e$  of  $[0/0/90_5]_s$  laminate measured by two methods  
Daming stresses:  $\Delta\sigma = 58$  MPa,  $R = 0.1$   
Nondestructive stresses for TSA:  $\Delta\sigma = 8$  MPa,  $R = 0.1$

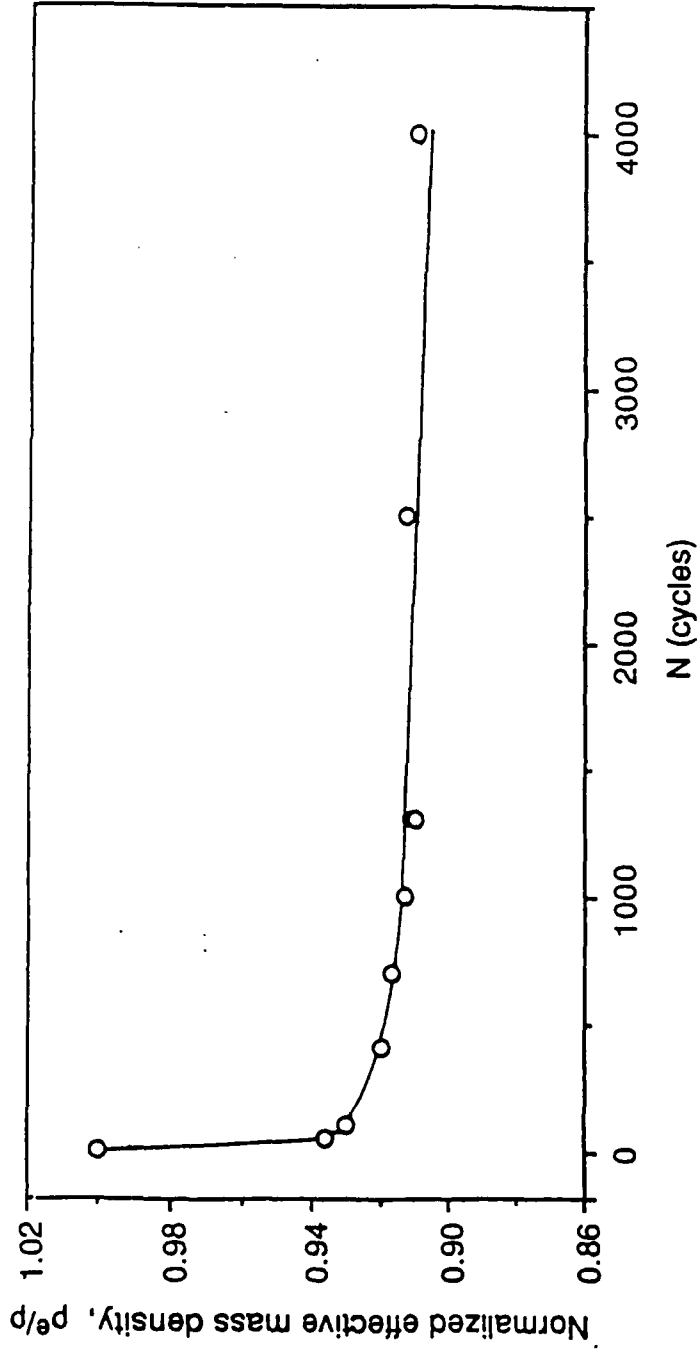


Figure 46 Normalized effective mass density  $\rho^e/\rho$  during damage evolution of [0/90/0/90/0]<sub>s</sub> laminate measured by the TSA method  
Daming stresses:  $\Delta\sigma = 317$  MPa,  $R = 0.1$   
Nondestructive stresses for TSA:  $\Delta\sigma = 31$  MPa,  $R = 0.1$

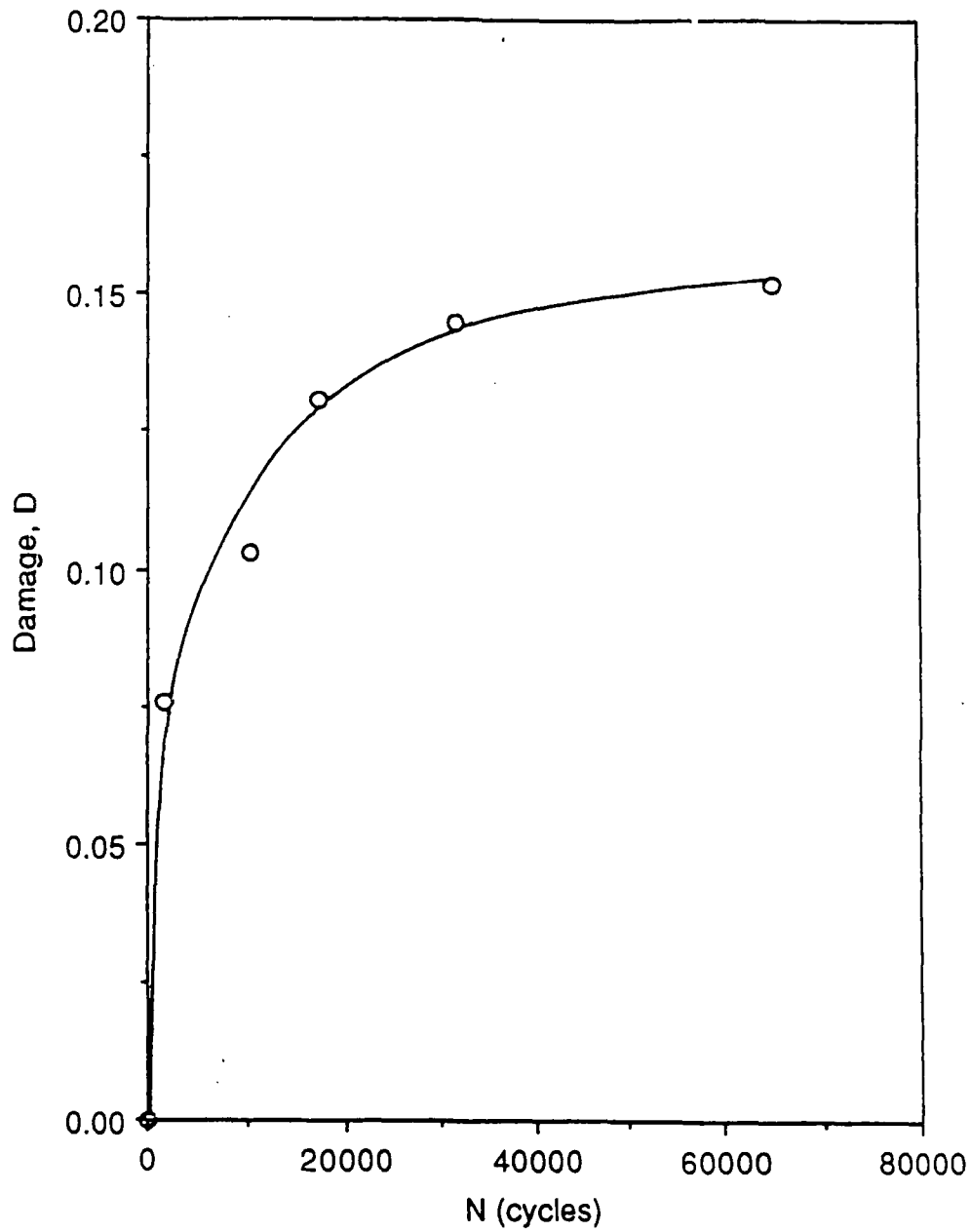


Figure 47 Damage accumulation of  $[0/0/90_5]_s$  laminate measured by the TSA method  
Daming stresses:  $\Delta\sigma = 58$  MPa,  $R = 0.1$   
Nondestructive stresses for TSA:  $\Delta\sigma = 8$  MPa,  $R = 0.1$

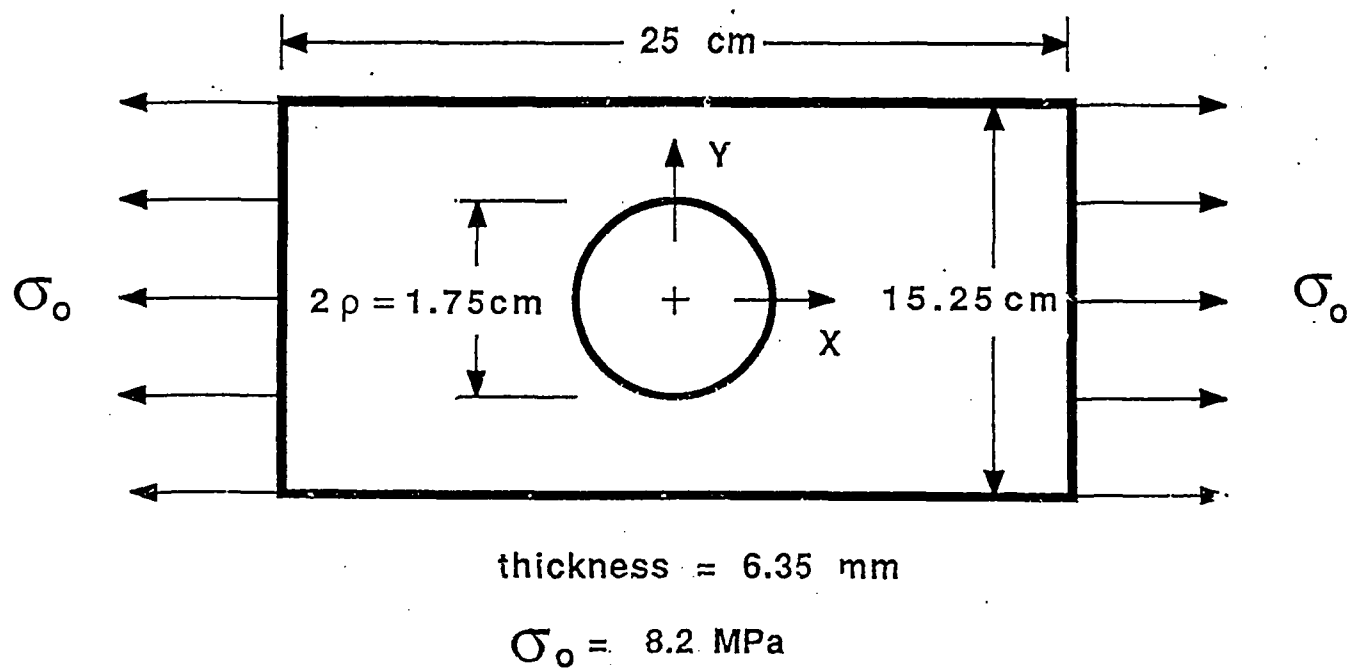
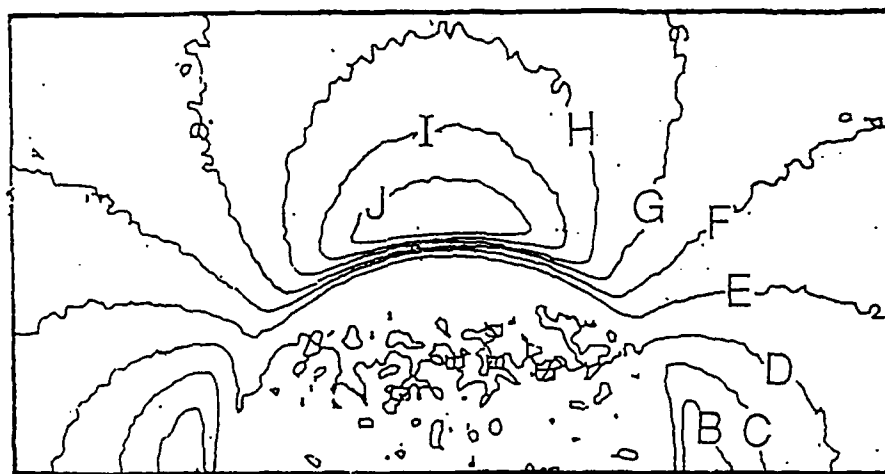
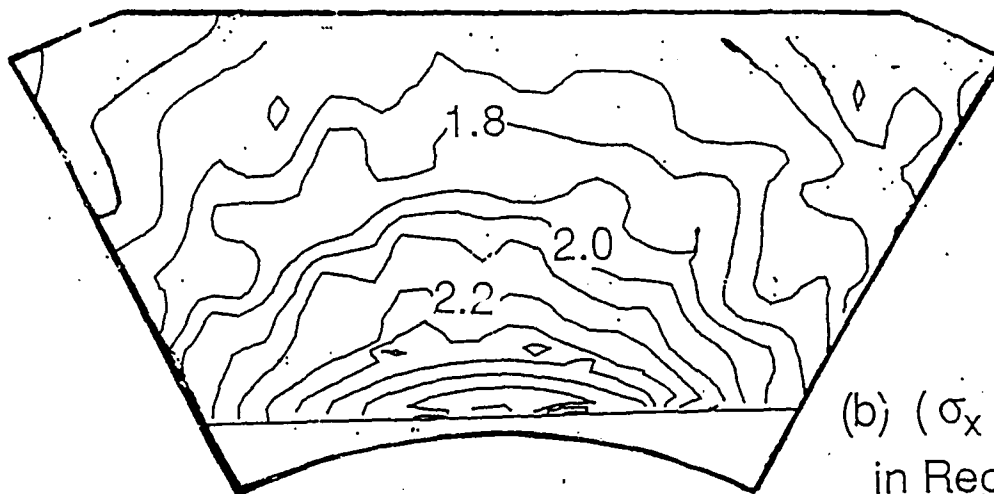


Figure 48 Tensile Aluminum Plate Whose Individual Stresses Were Determined Thermoelastically



J	-	950
I	-	800
H	-	650
G	-	500
F	-	350
E	-	200
D	-	50
C	-	-100
B	-	-250

(a) Thermoelastic Contours  
Around Hole



(b)  $(\sigma_x + \sigma_y) / \sigma_0$   
in Region R

Figure 49 Thermoelastic Information in Region R Adjacent to the Top of the Hole of Fig. 48

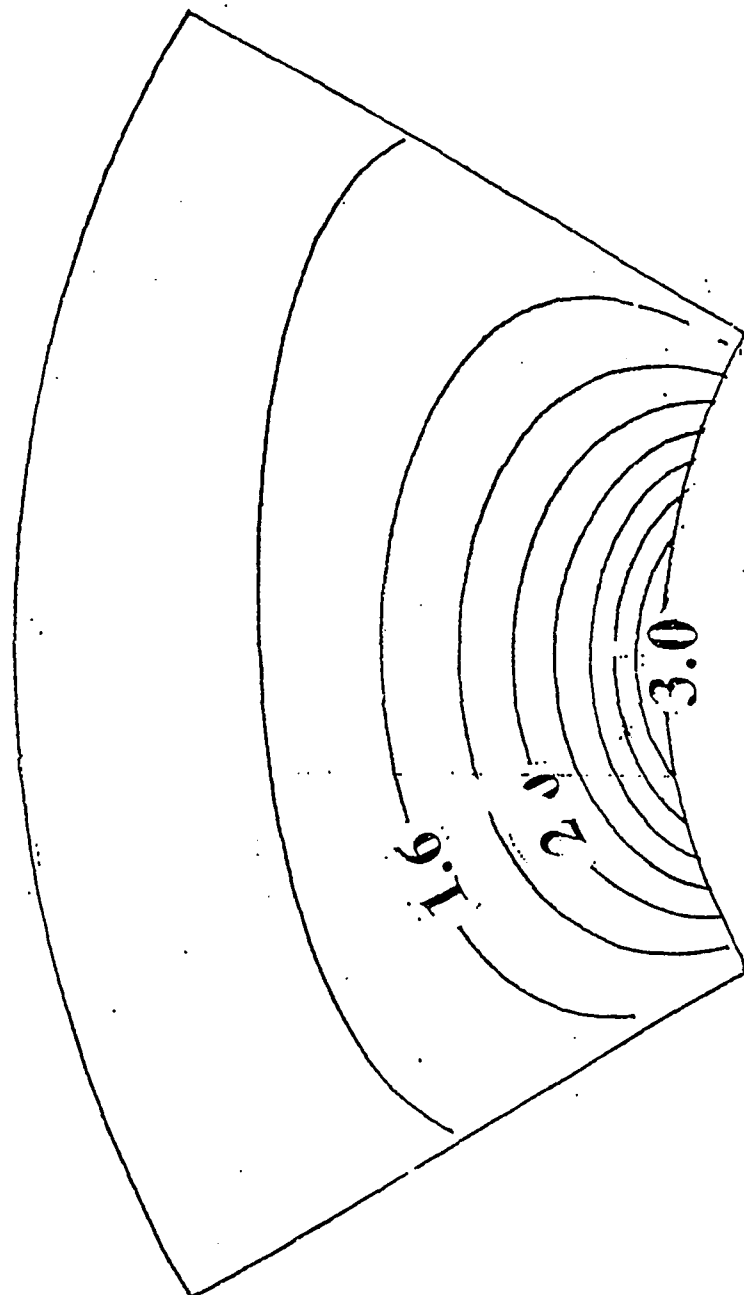


Figure 50 Thermoelastically Determined Tensile Stress  $\sigma_x / \sigma_0$  in Region R Adjacent to the Top of the Hole of Fig. 48

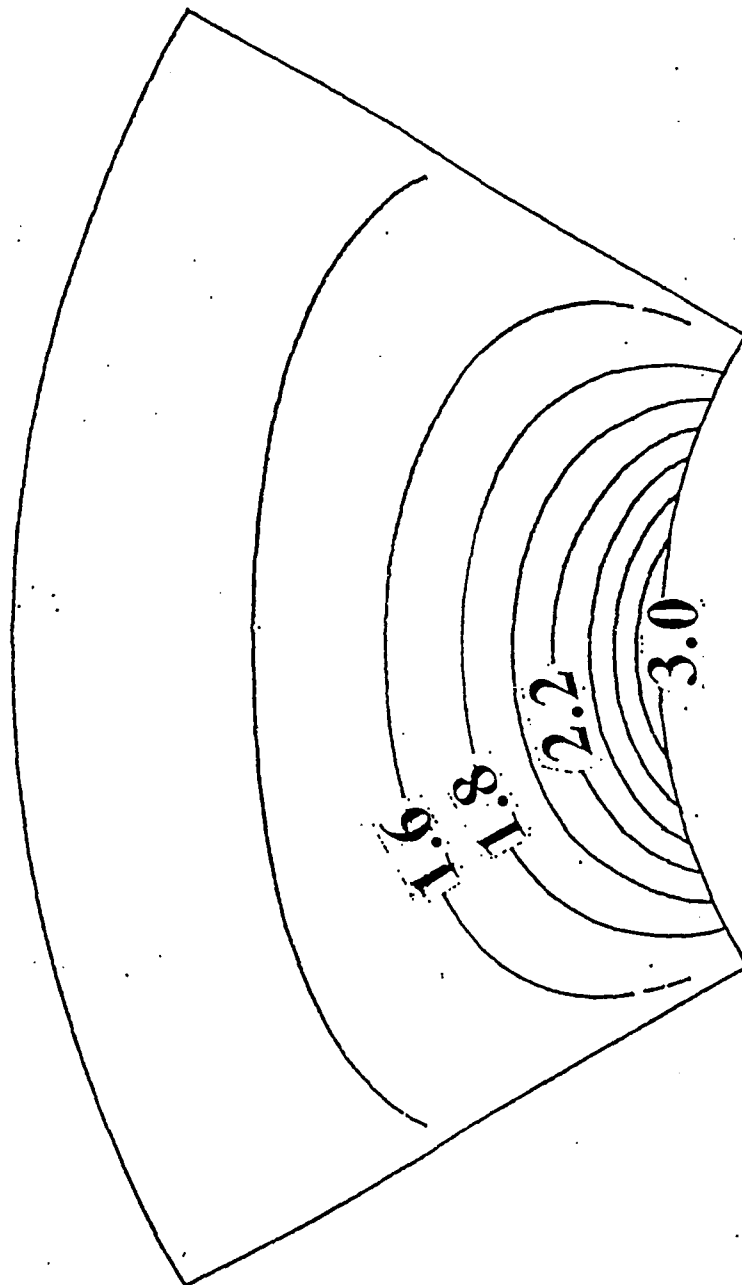


Figure 51 Theoretically Predicted  $\sigma_x / \sigma_0$  in the Region R Adjacent to the Top of Hole of Fig. 48

## REFERENCES

- [1] Weber, W., "Uber die spezifische Warme fester Korper insbesondere der Metalle," Pogg. Ann. D. Physik u. Chemie, Vol. 20, 1830, pp. 177-213.
- [2] Thomson, W. (Lord Kelvin), "On the Dynamical Theory of Heat," Transactions of the Royal Society of Edinburgh, Vol. 20, 1853, pp. 261-283.
- [3] Compton, K. T. and Webster, D. B., "Temperature Changes Accompanying the Adiabatic Compression of Steel. Verification of W. Thomson's Theory to a Very High Accuracy," Phys. Rev., Vol. 5, 1915, pp. 159-166.
- [4] Rocca, R. and Bever, M. B., "The Thermoelastic Effect in Iron and Nickel as a Function of Temperature," Trans. AIME, Vol. 188, Feb. 1950, pp. 327-333.
- [5] Dillon, O. W., "An Experimental Study of the Heat Generated During Torsional Oscillations," J. Mech. Phys. Solids, Vol. 11, 1963, pp. 35-39.
- [6] Dillon, O. W. and Taucher, T. R., "The Experimental Technique for Observing Temperatures Due to the Coupled Thermoelastic Effect," Int. J. Solid Structures, Vol. 2, 1966, pp. 385-391.
- [7] Belgen, M. H., "Infrared Radiometric Stress Instrumentation Application Range Study," NASA Report CR-1067, 1967.
- [8] Mountain, D. S. and Webber, J. M. B., "Stress Pattern Analysis by Thermal Emission (SPATE)," Proc. Soc. Photo-optical Inst. Engrs., Vol. 164, 1978, pp. 189-196.
- [9] Dillon, O. W., "A Nonlinear Thermoelasticity Theory," J. Mech. Phys. Solids, Vol. 10, 1962, pp. 123-131.
- [10] Wong, A. K., Jones, R. and Sparrow, J. G., "Thermoelastic Constant or Thermoelastic Parameter?," J. Phys. Chem. Solids, Vol. 48, No. 8, 1987, pp. 749-753.
- [11] Machin, A. S., Sparrow, J. G. and Stimson, M. G., "Mean Stress Dependence of the Thermoelastic Constant," Strain, Vol. 23, Feb. 1987, pp. 27-30.
- [12] Wong, A. K., Sparrow, J. G. and Dunn, S. A., "On the Revised Theory of the Thermoelastic Effect," J. Phys. Chem. Solids, Vol. 49, No. 4, 1988, pp. 395-400.
- [13] Machin, A. S., Sparrow, J. G. and Stimson, M. G., "The Thermoelastic Constant," in Stress Analysis by Thermoelastic Techniques, B. G. Gasper, Editor, Proc. SPIE Vol. 731, 1987, pp. 110-120.

- [14] Dunn, S. A., Lombardo, D. and Sparrow, J. G., "The Mean Stress Effect in Metallic Alloys and Composites," Proc. SPIE Vol. 1084, 1989, to be published.
- [15] Wong, A. K., Dunn, S. A. and Sparrow, J. G., "Residual Stress Measurement by Means of the Thermoelastic Effect," Nature, Vol. 332, No. 6165, April 14, 1988, pp. 613-615.
- [16] Dillon, O. W., "Coupled Thermoplasticity," J. Mech. Phys. Solids, Vol. 11, 1963, pp. 21-33.
- [17] Jordan, E. H. and Sandor, B. I., "Stress Analysis from Temperature Data," J. of Testing and Evaluation, Vol. 6, No. 6, Nov. 1978, pp. 325-331.
- [18] Jordan, E. H., "Temperature Based Stress Analysis of Notched Members," Ph.D. Thesis, Dept. of Engineering Mechanics, Univ. of Wisconsin-Madison, 1978.
- [19] Jordan, E. H., "Notch-root Plastic Response by Temperature Measurement," Experimental Mechanics, Vol. 25, No. 1, March 1985, pp. 24-31.
- [20] Stanley, P. and Chan, W. K., "'SPATE' Stress Studies of Plates and Rings Under In-Plane Loading," Experimental Mechanics, Vol. 26, No. 4, Dec. 1986, pp. 360-370.
- [21] Beghi, M. G., Bottani, C. E., Caglioti, C. and Fazzi, A., "A Spectral Analyzer for the Thermoelastic and Thermoplastic Response of Solids to Low Frequency Dynamic Loads," Second International Conf. on Stress Analysis by Thermoelastic Techniques, London, Feb. 17-18, 1987.
- [22] Beghi, M. G., Bottani, C. E. and Caglioti, G., "Irreversible Thermodynamics of Metals under Stress," Res Mechanica, Vol. 19, No. 4, 1986, pp. 365-379.
- [23] Enke, N. F. and Sandor, B. I., "Cyclic Plasticity Analysis by Differential Infrared Thermography," Proc. Sixth International Congress on Experimental Mechanics, Portland, Oregon, June 1988, pp. 830-835.
- [24] Enke, N. F., Lesniak, J. R. and Sandor, B. I., "High-Temperature Stress Analysis Using Differential Infrared Thermography," Proc. Fifth Annual Hostile Environments and High Temperature Measurements Conf., SEM, Costa Mesa, California, March 1988, pp. 4-7.
- [25] Dennis, P. N. J., *Photodetectors: An Introduction to Current Technology*, Plenum Press, New York, 1986.
- [26] Yates, H. W. and Taylor, J. H., "Infrared Transmission of the Atmosphere," U. S. Naval Research Laboratory, Washington, D. C., NRL Report 5453, 1960.

- [27] Keyes, R. J., Editor, *Optical and Infrared Detectors*, 2nd Ed., Springer-Verlag, New York, 1980.
- [28] Private communication with personnel of Ometron Inc., 1989.
- [29] EG&G Judson, Infrared detector catalog, Montgomeryville, PA, 1988.
- [30] Bever, M. B., Holt, D. and Titchener, A. L., "The Stored Energy of Cold Work," *Progress in Metal Science*, Vol. 17, Pergamon Press, Elmsford, New York, 1973.
- [31] Biot, M. A., "Thermoelasticity and Irreversible Thermodynamics," *J. Appl. Phys.*, Vol. 27, No. 3, March 1956, pp. 240-253.
- [32] Kovalenko, A. D., *Thermoelasticity: Basic Theory and Applications*, Wolters-Noordhoff Publishing Groningen, The Netherlands, 1969.
- [33] Young, W. B., Editor, *Residual Stress in Design, Process and Materials Selection*, Proc. of the ASM Conference, Cincinnati, OH, April 1987.
- [34] Rosenfield, A. R. and Averbach, B. L., "Effect of Stress on the Expansion Coefficient," *J. Appl. Phys.*, Vol. 27, 1956, pp. 154-156.
- [35] McKelvie, J., "Consideration of the Surface Temperature Response to Cyclic Thermoelastic Heat Generation," Proc. Second International Conf. on Stress Analysis by Thermoelastic Techniques, London, Feb. 1987.
- [36] Burrus, C. S. and Parks, T. W., *DFT/FFT and Convolution Algorithms: Theory and Implementation*, John Wiley, New York, 1985.
- [37] Sandor, B. I., *Fundamentals of Cyclic Stress and Strain*, University of Wisconsin Press, Madison, WI, 1972.
- [38] Jordan, E. H., "Fatigue - Multiaxial Aspects," in *Pressure Vessels and Piping Design Technology, 1982 - A Decade of Progress*, ASME, New York, 1982, pp. 507-516.
- [39] Garud, Y. S., "Multiaxial Fatigue: A Survey of the State of the Art," *J. of Testing and Evaluation*, Vol. 9, No. 3, May 1981, pp. 165-178.
- [40] Lamba, H. S. and Sidebottom, O. M., "Cyclic Plasticity for Nonproportional Paths: Part 1 - Cyclic Hardening, Erasure of Memory, and Subsequent Strain Hardening Experiments," *Trans. ASME, Series H*, Vol. 100, No. 1, 1978, pp. 96-103.
- [41] Askwyth, W. H., Hayes, R. J. and Mikk, G., "The Emittance of Materials Suitable for Use as Space-craft Radiator Coatings," *Am. Rocket Soc.*, paper 2538-62, 1962.

- [42] Brammer, J. A. and Percival, C. M., "Elevated-temperature Elastic Moduli of 2024 Aluminum Obtained by a Laser-Pulse Technique," *Experimental Mechanics*, Vol. 10, No. 6, June 1970, pp. 245-250.
- [43] Mondolfo, L. F., *Aluminum Alloys: Structure and Properties*, ButterWorths, London, 1976.
- [44] Versé, G., "The Elastic Properties of Steel at High Temperatures," *Trans. ASME*, Vol. 57, No. 1, 1935, pp. 1-4.
- [45] *Metals Handbook*, 9th edition, ASM, Metals Park, OH, 1978.
- [46] *Thermophysical Properties of Matter*, IFI/Plenum, New York, 1970.
- [47] D. Zhang, "Anisotropic Damage: a Thermoelasticity Theory and Verifications," Ph.D. Thesis, University of Wisconsin-Madison, May 1989.
- [48] Huang, Y.M., Hamdi AbdelMohsen, M.H., Lohr, D., Feng, Z., Rowlands, R.E. and Stanley, P., "Determination of Individual Stress Components from SPATE Isopachics Only," *Proc. 6th Int'l. Congress on Exper. Mech.*, Portland, OR, June, 1988, pp. 578-584
- [49] Y.M. Huang, "Determination of Individual Stresses from Thermoelastically Measured Trace of Stress Tensor," Ph.D. Thesis, University of Wisconsin - Madison, May 1989... Professor R.E. Rowlands, Advisor.
- [50] Y.M. Huang, H. AbdelMohsen and R.E. Rowlands, "Determination of Individual Stresses Thermographically," accepted for publication in *Experimental Mechanics*, 1989.
- [51] Y.M. Huang and R.E. Rowlands, "Quantitative Stress Analysis Based on the Measured Trace of the Stress Tensor," submitted for publication, 1989.
- [52] Y.M. Huang, R.E. Rowlands, and J.R. Lesniak, "Simultaneous Stress Separation, Smoothing of Measured Thermoelastic Information, and Enhanced Boundary Data," submitted for publication, 1989.
- [53] Y.M. Huang and R.E. Rowlands, "Experimental Thermoelastic Solution of Boundary - value Stress Analysis," to be submitted for publication by November, 1989.